INVESTIGATION OF NANOENERGETIC COMBUSTION STUDY OF ALUMINUM NANOPARTICLES SYSTEMS ON PLASMONIC GRATING PLATFORM

A Dissertation Presented to the Faculty of the Graduate School
University of Missouri – Columbia

In Partial Fulfillment
of Requirements for the Degree
Doctor of Philosophy

---

by
NAADAA G. ZAKIYYAN

Dr. Shubhra Gangopadhyay, Dr. Matthew Maschmann,
Dissertation Supervisors
July 2022

The undersigned, appointed by the dean of the Graduate School,
have examined the dissertation entitled

INVESTIGATION OF NANOENERGETIC COMBUSTION STUDY OF ALUMINUM NANOPARTICLES SYSTEMS ON PLASMONIC GRATING PLATFORM

presented by Naadaa Ghulaam Zakiyyan,

a candidate for the degree of Doctor of Philosophy,

and hereby certify that, in their opinion, it is worthy of acceptance.

_____

Dr. Shubhra Gangopadhyay
Department of Electrical Engineering and Computer Science

_____

Dr. Matthew Maschmann
Department of Electrical Engineering and Computer Science

_____

Dr. Syed Islam
Department of Electrical Engineering and Computer Science

_____

Dr. Scott Kovaleski
Department of Electrical Engineering and Computer Science

_____

Dr. Jacob McFarland

Department of Mechanical Engineering, Texas A&M University

ACKNOWLEDGEMENTS

It is a great pleasure to thank those who made this dissertation possible.

First and foremost, I would like to sincerely thank my primary advisors, Drs. Shubhra Gangopadhyay and Keshab Gangopadhyay, for their unwavering support throughout my time as an undergraduate and graduate student at the University of Missouri. They both have helped me become a well-rounded scientist, but perhaps more importantly they have influenced my empathy, leadership, and collaborative spirit. I will forever be grateful to them for everything.

I would like to thank my co-advisor, Dr. Matthew Maschmann, for his expertise and guidance in solving research challenges. His thorough and innovative ways of thinking have helped me over the course of my study. I also learn a lot from his knowledge of various facets of experimental and analytical expertise. I would like to thank my research advisor, Dr. Jacob McFarland, for the discussion in helping shape my research. I would like to thank my dissertation committee members, Dr. Syed Islam and Dr. Scott Kovaleski, for their time, presence, and feedback.

Thank you to all my lab mates, particularly Dr. Joseph Mathai, for his leadership and company throughout my studies. I would also like to acknowledge the members of the research group past and present, Dr. Charles Darr, Dr. Sangho Bok, Dr. Aaron Wood, Dr. Biyan Chen, Dr. Haizheng Zheng, Dr. Syed Barizuddin, Dr. Anqi Wang, Connor Wolenski, Matt Riehn, Jimmy Keating, and Camden Boyle.

A special thanks to my parents, Mr. Taufiek Bhirawa and Mrs. Erviana, for their sacrifice and support throughout. I am especially grateful for my wife, my siblings, my relatives for being there through the tough moments and celebrate the good. My family means a lot to me, my achievements are theirs, and I dedicate this dissertation to them.

Table of Contents

LIST OF FIGURES

LIST OF TABLES

ABSTRACT

With renewed interest in energetic materials like aluminum, many fundamental issues concerning the ignition and combustion characteristics at nanoscales remain to be clarified. Aluminum nanoparticles (Al NP) are widely used solid-state fuels in energetic material applications due to the abundance of aluminum and high heat of reaction. The metallic Al core of Al NP must escape an alumina shell to react with oxidizers. The diffusion oxidation mechanism (DOM) of aluminum has been suggested as governing the reaction mechanism, whereby both oxygen and aluminum diffuse through the oxide shell at low heating rates of 10^4-10^6 K/s. However, Al diffusion through the encapsulating shell restricts the reaction rate between the fuel and surrounding oxide. An alternative model is proposed and known as the melt dispersion mechanism (MDM), a rapid thermomechanical mechanism for rapid heating >10^6 K/s. This mechanism is driven by the volumetric expansion of rapidly melting Al core which ruptures the oxide shell. MDM has been widely proposed, and we present the first Al NP spallation observed at a particle scale.

Plasmonic photothermal heating was needed to facilitate the rapid heating required to initiate the MDM reaction mechanism. A plasmonic grating coupled with an external laser significantly enhances the intensity of photothermal heating experienced by an Al NP. Aluminum, itself, has strong plasmon resonances throughout the visible and ultraviolet spectrum and may be tuned based on Al NP diameter. Our experimental setup encompasses a wide range of available imaging methods to increase the imaging resolution in a table-top optical microscope. A high-resolution camera with a polarization-based scattering method readily identifies whether a particle is metallic or nonmetallic based on the obtained light intensity.

Spatiotemporal temperature dependence of Al NP is also observed using fluorescent dyes embedded in a polymer matrix. Finally, the photothermal heating of Al NP in different systems is modeled in COMSOL Multiphysics software using Electromagnetic Waves and Heat Transfer Modules. Based on the simulation, the estimated heating rate can determine the potential mechanism of the observed mechanism. The findings underline the crucial role of heating rates in observing particle spallation through plasmonic enhanced photothermal heating.

Combustion of Al NPs is also studied with fluoropolymer and metal-oxide acting as the oxidizer. The current study aims to establish a unified theory accommodating the reaction mechanisms of aluminum particles at micro and nanoscales. The presented works investigate the material constituents starting from individual particle-scale to macro bulk-scale to understand their reaction mechanism better.

CHAPTER 1 : INTRODUCTION

1.1 Energetic Materials

Energetic material (EM) represents substances with a significant amount of stored chemical energy that can be rapidly released. Researchers have shown that the proximity of EM constituents facilitates the reaction of kinetics to enhance energy release in a shorter time. Many EM applications of EMs have been thoroughly reported, including but not limited to the manufacture and use of explosives, propellants, pyrotechnics, and fuel. Based on the materials' structure, EMs have been generally divided into two categories, namely homogeneous and heterogeneous EMs. Homogeneous EMs, also known as monomolecular EMs, contain fuel and oxidizers within one molecule [1]. The reduced reaction distance between the fuel and oxidizer offers a significant benefit for this material to achieve maximized reaction kinetics.

Though most homogeneous EMs have been around since the early 20th century, several of these high explosives are still commonly used to this day. Many monomolecular EMs, primarily C-H-N-O-based EMs, have been developed and widely mass-produced. Examples of homogenous EMs include; nitroglycerine (the energetic foundation of dynamite), PETN (pentaerythritol tetranitrate), TNT (trinitrotoluene), RDX (cyclotrimethylenetrinitramine), and HMX (tetra-hexamine tetra-nitramine) [2]. The manufacture of EMs has further evolved. For example, in the late 1980s, the discovery of CL-20 with a superior detonation velocity of 10 km/s and energy density of ~3 kJ/g led to the development of a new generation of homogeneous EM. The most recent development is the Octanitrocubane (ONC) which has recently emerged with the prospect of having the highest theoretical detonation velocity [3].

Despite discovering new materials, the synthesized compounds have shown many limitations such as excessive sensitivity, high-production cost, and manufacturing challenges. Further, the limitation stems from energy density which depends on the materials' physical density and chemical stability [4]. The historical trend shows that homogeneous EMs are not increasing to match the energy needs currently. As a result, heterogenous EMs have emerged as alternative sources to improve the energy release rates to meet the high demand. Concerns about the lack of success in developing the materials also continue to motivate improvements in the material design and nanoengineering to meet specific applications.

Heterogeneous EMs are composite materials consisting of phase-separated fuel and oxidizers. The most notable and earliest known composite material is gunpowder (black powder), a physical mixture of sulfur and charcoal as a fuel and potassium nitrate as an oxidizer. One advantage of heterogenous EMs is that there is a wide range of composite fuel source alternatives. Metal fuels have been widely researched to study their high heat of combustion and have been used to increase energy densities of heterogeneous energetic materials when adequately mixed with oxidizers. For instance, metals are chosen to be the fuel because they are highly reactive and exhibit excellent mass and volumetric density relative to other materials. As shown in **Figure 1-1**, metal fuels, in this case, magnesium, aluminum, and boron have a higher heat of combustion than homogeneous energetic materials (CL-20, RDX, and TNT).

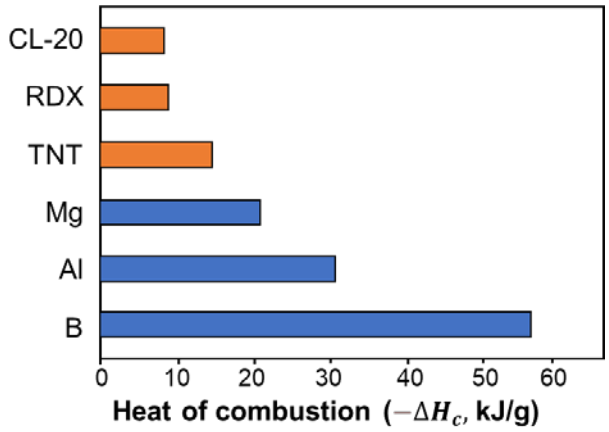

Figure 1-1. Comparison of the maximum heat of combustion on a per-mass base for commonly used organic energetic materials (orange bars) and metal fuels (blue bars). The fuels include elemental metal (Mg, Al) and metalloid (B). The graphic is redrawn from [5].

Currently, most heterogeneous EMs are in the form of thermites, comprising a reactive metal as the fuel and a metal oxide as the oxidizer. Typical thermite reaction undergoes as follows:

$$A + BO \rightarrow B + AO + \Delta H$$

where A is a reactive metal, BO is metal oxide consisting of a less reactive metal B, and ΔH is the heat of reaction. The reaction is exothermic because the produced metal oxide (AO) is more stable than the initial oxidizer (BO).

Examples of heterogenous EM include Boron and Aluminum. Boron is theoretically a more attractive fuel based on its extremely high heat of combustion on a per-mass base, as shown in **Figure 1-1**. However, on the downside, boron has a high ignition temperature that impedes its application. Upon heating, molten B_2O_3 coats the solid boron core acting as a limiting factor to the oxidation mechanism of boron, resulting in ignition and combustion delays [6]. This limits the performance of boron as a fuel material. While boron has a high melting point of 2,349 K and a low melting point of its oxide shell (723 K), aluminum has a low melting point of 933 K and

a high melting point of the oxide shell (2,345 K). Aluminum is relatively stable, benefiting from its naturally occurring thin and strong Al_2O_3 shell that prevents direct contact between aluminum and metal oxide. Aluminum generates large heat of reaction when they react with an oxidizer. By far, the most commonly employed metal fuel is aluminum due to its abundance, low cost, high energy density, and excellent ignition characteristics [7,8].

Transient metal oxides and other metal oxides have been proposed and investigated as oxidizers in thermite formulations. One prominent publication in the literature is an extensive report by Fischer et al. [9] on the thermophysical properties of thermite reactions. **Table 1-1** summarizes the thermophysical properties of aluminum-based and metal oxide thermite reactions. Some key indicators for thermite reactions are adiabatic reaction temperature (K), amount of gas production, and heat of reaction. Depending on the application needs, such as high reaction temperature or high gas production, the ability to tailor or engineer these thermites can lead to their possible use in a wide range of applications. For instance, some applications, such as thrust, demand a higher gas production; hence MnO_2, CuO, or Bi_2O_3 can be used as the oxidizer [10,11]. Meanwhile, CuO, MoO_3, and WO_3 are commonly used as oxidizers in nanothermite as they lead to high adiabatic reaction temperature and high heat of reaction. These thermites can produce self-propagating exothermic reactions with adiabatic flame temperatures over 3000 K.

Table 1-1. Thermophysical properties of some aluminum-based thermite reactions in alphabetical order [9].

Constituents	adiabatic reaction temperature (K)		gas production (mole/100g)	heat of reaction	
	w/o phase change	w/ phase change		-kJ/g	-kJ/cm^3
2Al+Bi_2O_3	3995	3253	0.4731	2.1	15.3
Al+3Co_3O_4	3938	3201	0.2196	4.3	20.0
2Al+Cr_2O_3	2789	2327	0	2.6	10.9
2Al+3CuO	5718	2843	0.5400	4.1	20.8
2Al+Fe2O_3	4382	3135	0.1404	4.0	16.5
4Al+3MnO_2	4829	2918	0.8136	4.8	19.5
2Al+MoO_3	**5574**	**3253**	**0.2425**	**4.7**	**17.9**
2Al+3NiO	3968	3187	0.0108	3.5	18.0
Al+PbO	3968	2327	0.4146	1.4	11.4
4Al+3SnO_2	5019	2876	0.2928	2.9	15.4
4Al+3TiO_2	1955	1752	0	1.5	5.5
10Al+3V_2O_5	3953	3273	0.0699	4.6	14.2
2Al+WO_3	5544	3253	0.1434	2.9	15.9

Molybdenum trioxide (MoO_3) appears to be the most attractive thermodynamically metal oxide to react with aluminum, based on **Table 1-1**. MoO_3 presents the compatibly of having a high adiabatic flame temperature as CuO, SnO_2, and WO_3, but with relatively higher heat of reaction when compared to others. The exothermal thermite reaction of aluminum and molybdenum trioxide releases a high heat reaction that follows the stoichiometric equation below [12]:

$$2\,Al + MoO_3 \rightarrow (Al_2O_3) + Mo \qquad (1.1)$$

$$\Delta H_{rxn} = 4.705\ kJ/g$$

Aside from the rapid exothermic reaction, MoO_3 is of interest to the study due to its layered structure, producibility, and scalability via liquid exfoliation [13] and van der Waals epitaxy growth [14], which will be discussed later.

Other types of heterogeneous EMs are aluminum and fluoropolymer composites which can also generate large amounts of heat release [15–17]. Due to the high fluorine content of fluoropolymers, it is highly advantageous to mix them with aluminum and form reactive materials. The formation of AlF_3 is one of the strongest bonds, with an energy of 665 kJ/mol [18]. Additionally, Fluorine-containing compounds, such as THV (terpolymer of tetrafluoroethylene, hexafluoropropylene, and vinylidene fluoride) and Teflon (polytetrafluoroethylene, or PTFE), act as oxidizers and a binder to provide structure to the EMs [19–21]. In PTFE and metal oxide composites, fluorination of the metal oxide also reduces the pre-ignition onset temperature [33,34].

Recently, additive manufacturing of reactive materials has also received much interest in developing inkjet, reactive ink, and direct writing techniques involving fluoropolymer EMs [22,23]. In addition, due to its excellent optical transmission and low absorption, THV can also be used as a medium of efficient externally induced photothermal heating of nanoparticles [24].

Over the past decades, ways to improve the reaction rates of EMS have been explored. One of them is by employing nanoscale reactants and reducing their characteristic mass diffusion length [8,25]. Reducing the sizes of metal particles and mixing them with finely divided oxidizers can improve the performance of heterogenous EMs. The increased contact surface area between fuel and oxidizer can significantly increase mass transfer and reaction rates. As a result, the combination of

nano MoO_3 and Al nanoparticles (Al NPs) shows that nanoscale fuel-oxidizer has better energetic performance. As shown in **Figure 1-3**, the energetic performance of micron constituents of MoO_3 and Al are compared to their nanoscale counterparts. Experimental setups, which will be explained later, measure the pressurization rate and the linear burn rate of different constituents' size combinations.

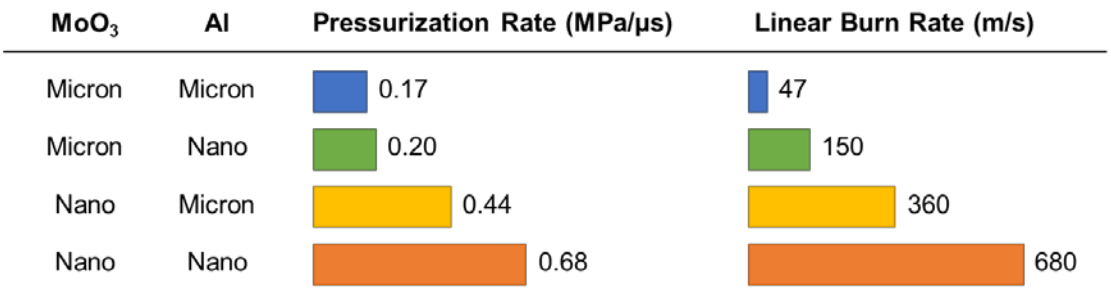

Figure 1-2. Pressurization rates and linear burn rates of Al-MoO_3 composites were tested at various combinations of constituents' sizes. All composites were prepared at an equivalence ratio of 1.4. The figure is created from [26] for illustration to add clarity.

Further improvement can also be made by using surface chemistry to induce the self-assembly of the fuel and oxidizer constituents [27–29]. The reaction rate can also be made faster by applying the concept of particle morphologies, for instance, using layered metal oxide materials. Layered two-dimensional (2D) materials such as graphite, molybdenum disulfide, and molybdenum trioxide have attracted significant attention for numerous applications ranging from multifunctional composite materials to electronic devices [13,30–33]. These materials consist of planar sheets with strong in-plane chemical bonds but weak out-of-plane van der Waals bonds. Such materials are readily exfoliated to produce single or few-layered atomic sheets for high surface area interaction [34,35]. These 2D materials have been used as templates to grow nanoparticles of metal or oxides [35,36] and used for enhanced in-plane electron mobility and heat conduction [37,38]. Moreover, nanoscale fuel-and-oxidizer materials'

surface properties can also be controlled through the assembly of nanomaterials to improve combustion performance [27].

As previously mentioned, Al NPs are coated with a passivation layer of aluminum oxide (alumina or Al_2O_3). In energetics, the presence of the oxide shell must be accounted for because smaller particles carry a substantial proportion of the shell, which is essentially dead weight. In spherical Al NPs, the thickness of the oxide shell is typically in the order of 2-5 nm, as characterized by Transmission Electron Microscope (TEM) in **Figure 1-3**.

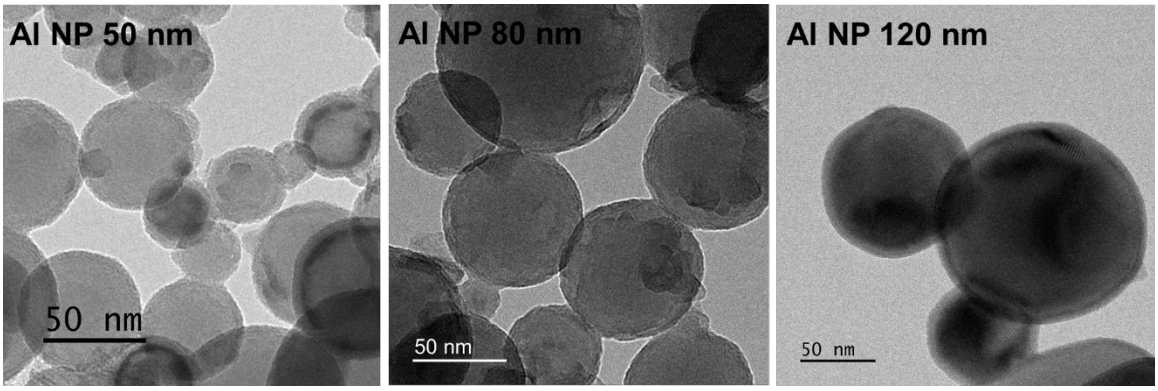

Figure 1-3. TEM characterizes the size distribution of aluminum nanoparticles with different diameter sizes: 50 nm, 80 nm, and 120 nm. For each nanoparticle diameter, the shell thicknesses are 2.62 nm, 3.26 nm, and 3.76 nm, respectively.

From a mechanical standpoint, the core-shell structure in Al NPs combustion and its implication are important topics. The mechanism by which the Al NPs react with an oxidizer to initiate combustion is still debatable. Researchers have proposed different reaction mechanisms of Al particles with various oxidizers [39–43]. The first proposed mechanism is the diffusion oxidation mechanism (DOM), whereby both oxygen and aluminum diffuse through the oxide shell at a relatively slow heating rate (10^4-10^6 K/s) [39]. In DOM, the Al core of NPs is nearly isothermal due to the small physical dimensions and high thermal conductivity. Al diffusion through the encapsulating shell

restricts the reaction rate between the fuel and surrounding oxide. TEM studies and theoretical modeling have shown that the outward diffusion of Al is more rapid than the inward diffusion of oxygen, causing the coarsening of the amorphous oxide layer [44]. This observation is consistent with the DOM theory [44].

The second mechanism is called the melt-dispersion mechanism (MDM), a mechanochemical mechanism for fast oxidation at a higher heating rate (10^6-10^9 K/s) [45,46]. MDM proposes the spallation of Al particles due to mechanical force generated during rapid heating and volumetric expansion of the melting Al core. The theoretical calculation has shown that the alumina shell of Al NPs does not break due to the thermal expansion coefficient of Al and alumina until the Al core melts [45,46]. The rapid melting of Al accompanied by a 6% volume expansion creates a high dynamic pressure of up to 3 GPa. The high hoop stress on the alumina shell is sufficient to induce mechanical failure and spallation of the Al core [47]. Activation of this effect requires specific conditions, which include very high heating rates (10^6-10^9 K/s), a core temperature that exceeds the melting temperature of Al (933 K), and a sufficiently homogeneous alumina shell that can withstand the building pressure provided by the Al core [20]. Furthermore, the different Al oxidation mechanisms share a similar role in delivering the fuel to react with oxidizers. Regardless of the specific combustion mechanism, the intimate proximity of fuel and oxidizer composites can increase the heat of reaction and flame propagation rate, which is desirable for many nanoenergetic applications [28,48].

1.2 Literature Review

In published literatures, the **melt dispersion mechanism** (MDM) has never been directly observed in an isolated condition. Instead, MDM is primarily proposed when

experimental configuration can achieve a heating rate of >10^7-10^9 K/s, mainly observed during a bulk reaction in many reports [15,43,49]. The MDM requires a fast-heating rate to heat the core, create tensile pressure, and spall the particle. A recent experiment and simulation results have pointed out that the photothermal fluence must be beyond ~1-2.5 J/cm^2 to raise the Al core temperature to its melting point [50]. One important consideration is the core-to-shell ratio to determine the required temperature for MDM to occur. The figure below is the simulated graph of the fracture temperature of core-shell Al NPs as a function of m, defined as the ratio of oxide thickness to the radius of the Al core. The graph is obtained from reported literature, while the data points indicate the Al NPs sizes used in our experiment: 50, 80, and 120 nm.

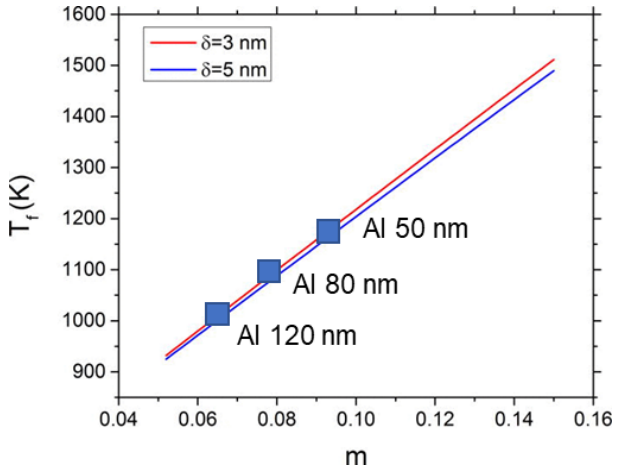

Figure 1-4. Simulated fracture temperature of core-shell Al NPs is presented as a function of m, defined as the ratio of oxide thickness to the radius of the Al core. Temperature T_f of an Al nanoparticle, required for fracture of the oxide shell after complete melting of Al, vs. $m = \delta/R$ for shell thickness δ = 3 nm and δ = 5 nm [51]. Additional data points indicate the Al NPs sizes used in our experiment: 50, 80, and 120 nm.

The borderline for a photothermal heat source can be estimated to satisfy the MDM requirement. As MDM requires a heating rate of beyond 10^7 K/s, a minimum temperature rise dT of 640 K for Al melting must occur within the duration dt of 6.4x10$^-$

^{5} s. Assuming a spherical aluminum nanoparticle with a constant density, the minimum fluence required for MDM can be estimated as follows:

$$F = \frac{1}{QLe}.q".\ dt = \frac{4}{3}\rho c_p r\ dT \tag{1.2}$$

where F is the minimum fluence [J/m^2], $q"$ is the minimum energy flux [W/m^2], ρ is the density [kg/m^3], c_p is the specific heat capacity [J/kg], r is the particle radius [m], Q is the absorption efficiency (absorption/ geometric cross section), L_e is the energy loss constant (~0.1). This assumption accounts for any phase change of the Al NP or any energy loss to the surrounding.

The photothermal heating experiments can be plotted based on power density as a function of exposure time to assist in classifying different reaction mechanisms. The photothermal heating fluence is drawn as the diagonal blue dotted line. Each diagonal line, representing the fluence, is calculated from the range of energy deposited and its irradiation time to initiate the reaction. Based on our calculation above, the expected regions for MDM are drawn in the orange shaded area in **Figure 1-5**.

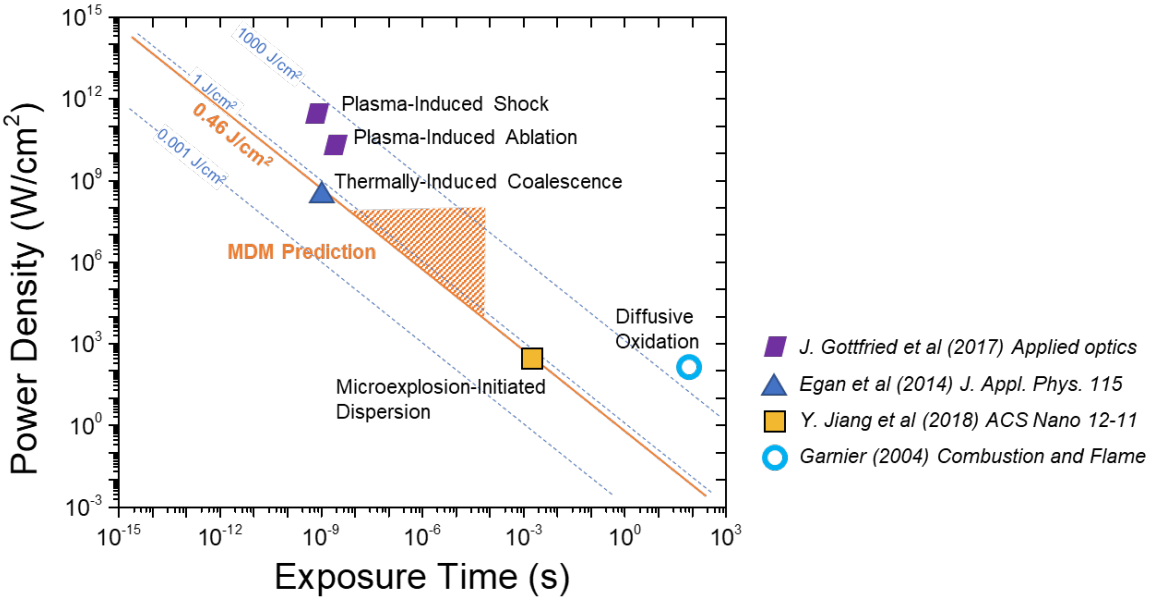

Figure 1-5. Recent reported works on photothermal-initiated Al particles reaction mechanisms are plotted to the experimental parameters, namely the laser heating source's peak power density and exposure time. Each diagonal line, representing the laser fluence, is calculated from the range of energy deposited and its irradiation time.

Figure 1-5 summarizes our observation and recent works on Al particle's reaction mechanisms using laser ignition experiments [10,52,53]. Works from Granier et al. [12] marked one of the earliest works on laser ignition experiments that observed **diffusive oxidation** reactions on composites of Al and MoO_3 (marked as ○ in **Figure 1-5**). The laser initiates the bulk pellets sample of MoO_3 and various Al particle sizes ranging from nano- to micron-particles. A 50-W CO_2 laser with a power density of 100 W/cm^2 was operated in a continuous wave CW mode. The laser was held constant at maximum power while a shutter regulated the laser irradiation. In **Figure 1-5**, the laser exposure time is estimated using the ignition time in the paper. The ignition time is the time delay between the events when the laser is triggered and when the first luminescent flame. The ignition time varies between 20-260 ms depending on the material composition as the main factor. While the paper's author extensively

discusses the study of ignition time and burn rate of Al/MoO_3 reactions, post-combustion products are discussed shortly. Further, the report categorizes the reaction towards diffusive transport mechanism as one possible explanation and complete or nearly complete oxidation mechanism. This work emphasizes that a continuous long laser pulse results in diffusion oxidation mechanism which is associated to slow heating rate (10^2–10^5 K/s).

Furthermore, other reaction mechanisms can be observed when the deposited energy is beyond the MDM requirement instead of spallation of Al NPs. **Plasma-induced ablation** (marked as ▰ in **Figure 1-5**) of aluminum particles was observed in a pulsed Nd: YAG laser (Quantel Brilliant, 6 ns, 1064 nm, 850 mJ) to ablate and ionize Al NPs, forming a high temperature (>10,000 K) micro-plasma that persisted for several microseconds [10]. The laser-induced plasma was observed to accelerate the resulting laser-induced shock wave captured with a typical Z-type schlieren imaging setting. The focused laser pulse can effectively provide a heating rate of ~10^{13} K/s. In a similar experiment, the laser with a fluence of ~3.4 J/cm^2 is exposed to Al/GO to enhance the combustion properties. This experiment is later known as the laser-induced air shock from energetic materials (LASEM) technique.

Another exciting finding can be classified as **Microexplosion-initiated dispersion** (marked as ▢ in **Figure 1-5**), which was observed by flash pulse heating on nano-Al particles with an average diameter of 60-96 nm [54]. The author claims the TEM analysis shows evidence of an Al_2O_3 shell partially ruptured and molten Al dispersed out of the shell. The 1-ms flash, a broad-spectrum light source, has an energy density of 0.62 J/cm^2 and was exposed to bulk Al powder on top of a glass slide. The visual observation indicates the presence of 3-20 nm product particles,

while in some cases, the ignited Al particles eventually led to the outflow of the molten Al. The observation led the report to suggest that the camera flash provided enough energy to melt the Al and generated a large dynamic pressure inside the NP to rupture its shell. However, this work's instrument is insufficient to satisfy the MDM requirement based on our estimation, as shown in **Figure 1-5**.

The authors argue that the findings are the first direct nanoparticle dispersal claim via flash-pulse heating [54]. Although the result of the photothermal dispersal is consistent with MDM and contradicts the DOM, this work may best be categorized as flash pulse-induced dispersal. The paper explains that ignition can only be observed in a reactive atmosphere. In the absence of reactive gas, no ignition was observed when the experiment was performed in the argon environment. The figure shows that the heating power density and exposure time are far below and insufficient for MDM requirements. Consequently, the alumina shell broke in the presence of reactive gas, and the aluminum core melted out without dispersion. When the reactive gas entered, the Al reaction provided additional rapid heating for neighboring particles, hence initiating the occurrence of MDM [49]. Further, the experimental findings also show that sparsely distributed nano-Al and micron-Al were not ignited by flash ignition.

In contrast to the MDM theory, coalescence of nanoparticles can occur during photothermal heating. **Thermally-induced coalescence** (marked as ▲ in **Figure 1-5**), was also observed on nano-Al particle aggregates subjected to rapid laser heating (10^6-10^{11} K/s) in an electron microscope instrument. The TEM equipped with a pulsed laser (1064 nm wavelength) was used to induce photothermal heating of the sample. The 12 ns laser pulse has a fluence of 0.123 J/cm^2. Their experiment used nano-Al 80nm particles, with a 2–5nm amorphous oxide shell, deposited onto a TEM grid.

Dynamic TEM observes the morphological changes between the laser pulses. The results indicate that the nanoparticle agglomerates significantly coalesce into larger structures. The author claimed that the subsequent loss of surface area accounted for up to 65 %, while further heating resulted in the mass loss by evaporation. In a separate experiment, higher laser fluences led to higher coalescence. Hence, the report challenges that the particle may experience thermally induced coalescence well before the combustion event. Without a nearby oxidizer, the claim detriments the functionality of the nanostructure by not retaining the high surface-to-volume ratios required for increased combustion rates [53]. With the presence of intermixed nano-oxidizers, the readily available oxidizing agent can rapidly be exposed to a high surface area of the molten Al fuel.

1.3 Aim and Objectives

The challenge of determining the Al NPs' oxidation mechanism during combustion comes from the lack of nanoscale observation. Experimentally, one can expose the Al NPs under high temperature and high heating rates to emulate the conditions of actual combustion. Some recent reports postulating the reaction mechanisms of Al NPs are performed in bulk combustion, hence unable to track the origin of the product particle [55,56]. Whereas performing a low heating rate condition, e.g., DSC TGA heating at 10-25 K/minute, fails to mimic the fast nature of an ideal combustion event. There also have been attempts to provide nanoscale observation by performing a rapid Al NPs heating experiment in a high-resolution electron microscope using a laser or a heating stage [18,53]. However, the presence of a high-energy electron beam and the vacuum environment associated with the electron microscope can alter the Al NPs'

response. Hence, the experiment is somewhat unsuitable for replicating a combustion event.

We aim to tackle the challenge of determining the underlying mechanism by observing localized Al NPs' reactions. One efficient method to initiate energetic material reactions at a high heating rate is photothermal heating, photoexcitation of material by electromagnetic radiation resulting in thermal energy (heat) production. Isolating the reaction to only several Al NPs can help determine the earliest combustion regime and study how the combustion is initiated. We introduce the plasmonic grating microchip to enhance the localized electric field and deliver rapid photothermal heating of Al NPs. The plasmonic grating couples with an external laser to significantly enhance the intensity of photothermal heating, therefore, increasing the heating rate. The photothermal ignition allows a non-invasive and rapid heat generation necessary to emulate combustion events. The downside of using an optical microscope is the limited resolution compared to experiments using the electron microscope. To tackle the lack of resolution, nanoscale observation can be performed before and after the laser photothermal experiment.

1.4 Methods: Plasmonic Grating

1.4.1 Surface plasmon resonance

Nanoscale materials exhibit unique and enhanced properties that continue to intrigue scientists to discover novel methods to learn its potential for various nanotechnology breakthroughs and applications [57–59]. The emergence of plasmonic is the most recent breakthrough in the field of optics and electronics. Plasmonic confines light within dimensions much smaller than the optical wavelength by utilizing surface plasmon resonances (SPR). SPR is a mechanism in which

electromagnetic waves resonate with the free electron in a metal film/substrate. SPR occurs where photons of incident light from a specific incident angle excite the electrons at the metal surface. While studying the metal/dielectric interface, it is essential to note that SPP consists of both free electron motion at the metal surface (surface plasmons) and electromagnetic waves in the dielectric (polaritons). These free electrons and surface plasmons result in the propagation of charge oscillation parallel to the metal surface, called surface plasmon polaritons (SPP). SPP can travel between two media interfaces with dielectric constants of opposing signs. The assumptions are that the dielectric and metal are homogeneous, isotropic materials and are linearly polarized and magnetized in response to external fields.

Electromagnetic representation of surface plasmon can be derived from Maxwell's equations. The relationship between the wavevector, k , and the permittivity, ε, of each material, is expressed as:

$$\frac{k_{\perp m}}{k_{\perp d}} = -\frac{\varepsilon_m}{\varepsilon_d} \tag{1.3}$$

where $k_{\perp m}$ is the wavevector component of electric and magnetic fields at the interface perpendicular to the metal interface, m, while $k_{\perp d}$ is the wavevector component perpendicular to the dielectric, d. This relation can only be satisfied if ε_m and ε_d have the opposite signs, which is indeed valid for metal with negative permittivity (ε_m< 0) and a dielectric with positive permittivity (ε_d> 0). In addition, the wavevector k_0, for each medium satisfies the relation:

$$k_{\parallel i}^2 + k_{\perp i}^2 = \varepsilon_i k_0^2 \tag{1.4}$$

where i represents both metal and dielectric media, while $k_{\parallel i}$ is the wavevector component parallel to each medium and is equal in both media. Therefore, the surface

plasmon propagating at the metal/dielectric interface can be represented by a dispersion relation as shown below:

$$k_{SP} = \frac{\omega}{c}\sqrt{\frac{\varepsilon_d \varepsilon_m}{\varepsilon_d + \varepsilon_m}} \tag{1.5}$$

SPP can be generated by forming SPR using incident light and can be seen in **Figure 1-6(a)**. Here, a photon strikes a planar metal surface having a specific frequency, ω, and propagating through a dielectric medium with a refractive index (RI.) $n = \sqrt{\varepsilon}$, at an angle θ to the normal. The in-plane parallel wavevector can be described as:

$$k_{\parallel} = \frac{\omega}{c}\sqrt{\varepsilon_d}\, sin\theta = \frac{\omega}{c} n\, sin\theta \tag{1.6}$$

At any given frequency ω, the generated SPP with a corresponding wavevector k_{SP} in equation (1.5) will always be greater than the parallel wavevector $k_{\parallel}$ (1.6). As a result, simply using a flat metal surface will not couple the photon of the incident light to the SPP, as illustrated in **Figure 1-6(b)**.

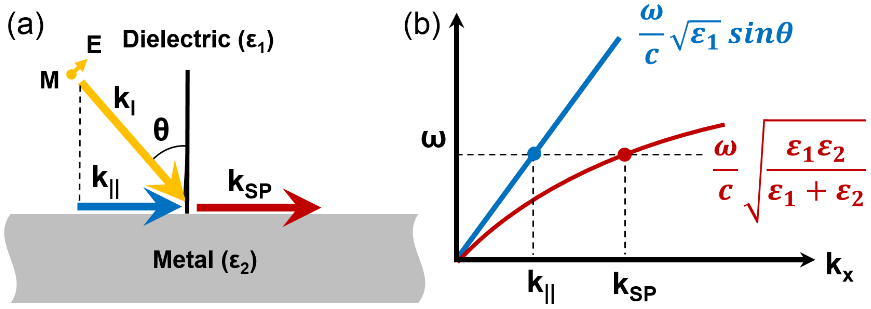

Figure 1-6. (a) Illustration of a photon incident on a metal/dielectric interface and (b) photon dispersion compared to the plasmonic dispersion showing that $k_{SP} > k_{\parallel}$ at any frequency ω [60].

To match the SPR wavevector and couple to the SPP, the photon wavevector of the incident light needs additional energy and momentum. The first method that can

provide the additional momentum to match the SPR wavevector involves combining a high refractive index prism n_{prism} with a thin noble metal film. Popularly introduced by Otto and Kretschmann [61,62], several prism-based configurations were used to excite the surface plasmon on a metal surface using photons of the incident light. Their methods resulted in the wavevector matching in equation (1.7) below.

$$k_{SP} = \frac{\omega}{c}\sqrt{\frac{\varepsilon_d \varepsilon_m}{\varepsilon_d + \varepsilon_m}} = n_{prism}\frac{\omega}{c}\, sin\theta_{SPR} = k_{prism} \tag{1.7}$$

where ε_m is the permittivity of the metal film, ε_d is the permittivity of the dielectric, e.g., air or water, and θ_{SPR} is the surface plasmon resonance angle for a specific wavelength λ to achieve SPR.

The concept of prisms traces back to the phenomenon of anomalous diffraction that was first described in the early twentieth century by RW Wood [63]. In the late 1960s, Kretschmann and Otto demonstrated several prism-based SPR excitation configurations by the methods of attenuated total reflection [61,62]. However, several limitations come with the prism-based method: 1) the system is susceptible to the thickness of the metal and dielectric layers; 2) the relatively bulky prism limits its application to be integrated into other devices or setups; 3) the coupling is limited to a certain angle and wavelength, and 4) these configurations are expensive to build and operate. The limitations in the theories and applications in surface plasmons and their significant properties elicited many studies which have led to further discoveries [64–66]. Hence, the discovery of nanostructures grating-based systems to generate SPR has become an alternative to prism-based configurations [67].

The nanostructures grating-based method to generate SPR utilizes a metallic grating - a periodic pitch structure comprised of parallel grooves and ridges, shown in

Figure 1-7(a). The grating pitch Λ is the peak-to-peak distance, and the grating height h is the distance from the bottom of the groove to the top of the ridge. When a photon with a specific wavelength λ similar to the pitch size Λ, strikes the metal grating at an incidence angle θ_I, it will be diffracted at a specific angle θ_D, shown in **Figure 1-7(a)** and can be represented by the diffraction equation below.

$$sin\theta_D = \frac{m\lambda}{\Lambda} - sin\theta_I \tag{1.8}$$

where m = 0, ±1, ±2, … is the diffraction orders that constructively interfere and enhance the total field due to individual scattered waves.

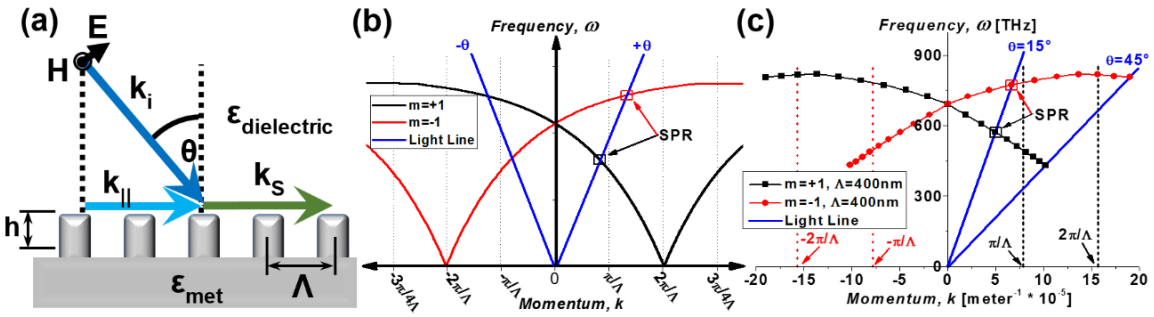

Figure 1-7. (a) Illustration of a photon incident on a grating interface. (b) Theoretical and (c) experimental frequency vs. momentum plot depicting photon and SPR wavevector matching conditions [60].

The grating vector $\boldsymbol{k}_\Lambda$ for periodic metal grating with a given grating pitch is defined as:

$$\boldsymbol{k}_\Lambda = \frac{2\pi}{\Lambda} \tag{1.9}$$

Note that the grating vector in the x-direction is perpendicular to the grating grooves. Several orders of grating vector m can be accumulated to provide additional photon momentum to couple to the SPP. Therefore, the incident photon that excites the surface plasmons upon the metallic grating surface can be represented as:

$$k_{SP} = \frac{\omega}{c}\sqrt{\frac{\varepsilon_d \varepsilon_m}{\varepsilon_d + \varepsilon_m}} = k_{\parallel} + m\boldsymbol{k}_{\Lambda} = \frac{\omega}{c}\sqrt{\varepsilon_d}\, sin\theta_{SPR} + m\frac{2\pi}{\Lambda} \quad (1.10)$$

The proper coupling conditions at a specific range of values can be visualized theoretically in frequency vs. momentum plots in **Figure 1-7 (b)** and experimentally in **Figure 1-7 (c)**. It can be observed that there are resonance conditions at a particular θ_{SPR} angle at a specific wavelength. (refer to the arrows in the graph)

1.4.2 Plasmonic Grating Fabrication

The plasmonic grating microchip can be fabricated using a microcontact lithography stamping process as described in previous literature [68]. HD DVD gratings (height: 60 nm, L: 400 nm) are negatively copied using polydimethylsiloxane (PDMS) stamping and then replicated in polymethylsilsesquioxane (PMSSQ) “ink” with an added cross-linker, 3-aminopropyltriethoxy-silane (APTES), depicted in **Figure 1-8**. Furthermore, 40nm or 100 nm thin film of silver (Ag) and a 10 nm thick protective layer of alumina (Al_2O_3) are deposited on the grating by atomic layer deposition method to obtain the plasmonic silver grating microchip used in the later chapters.

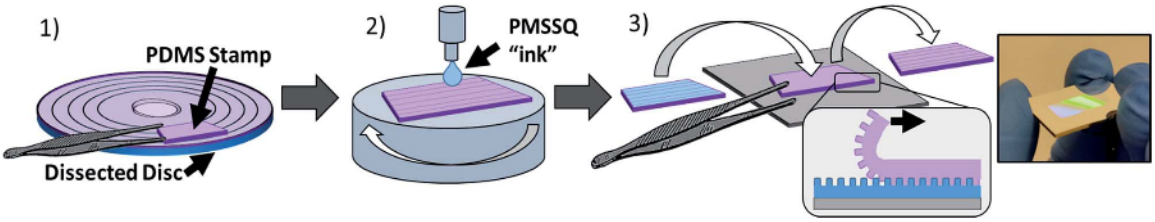

Figure 1-8. Soft lithography process diagram. (1) Cut and remove the PDMS stamp pieces from the disc mold; (2) spin coat PMSSQ “ink” solution onto the PDMS stamp; (3) stamp and peel off the PDMS onto a glass slide or silicon wafer. [68]

1.4.3 Dispersion Relation

SPR dispersion curve, represented by wavelength (λ) vs. incidence angle (θ) at specific mediums, can indicate the optimum angles for coupling the light emission [60].

The effect of the medium representing the varying refractive index that governs SPR has been studied to understand dispersion relation better. The dispersion curve is characterized using ellipsometer measurements in various mediums shown in **Figure 1-4**. Transmission and reflection data of the medium (air, oil, and polymer) on the grating are used to determine the plasmonic coupling.

Ellipsometer transmission measurements of a transparent grating microchip in different media, e.g., air and oil, are presented in **Figure 1-9 (a)** and **(b),** respectively. **Figure 1-9 (c)** represents the corresponding dispersion curve with distinct transmission measurement peaks indicating several SPR modes. The SPR modes of PMSSQ/Ag resonance peak appear at around 625 nm for both mediums, as denoted by the circles in **Figure 1-9**. The refractive index difference between the medium and grating interface also appeared in the dispersion curve below. SPR mode of air/grating (blue curve) and oil/grating (red curve) interfaces are well represented by resonance peaks at around 460 nm and 625 nm, respectively.

Polymers with an excellent coupling to the grating will be used as they can constructively interfere and couple the light substantially. The intense light coupling can be used to generate localized heating for aluminum nanoparticle ignition. These fluoropolymers will also be used as mediums in combustion studies with aluminum nanoparticles to create nanoenergetic films. Furthermore, the latter studies will incorporate various polymers with different refractive indexes. In addition to utilizing 40 nm silver plasmonic grating, a thicker 100nm silver plasmonic grating substrate will be used in some experiments in this dissertation. The characterization and application will be discussed in the later chapters.

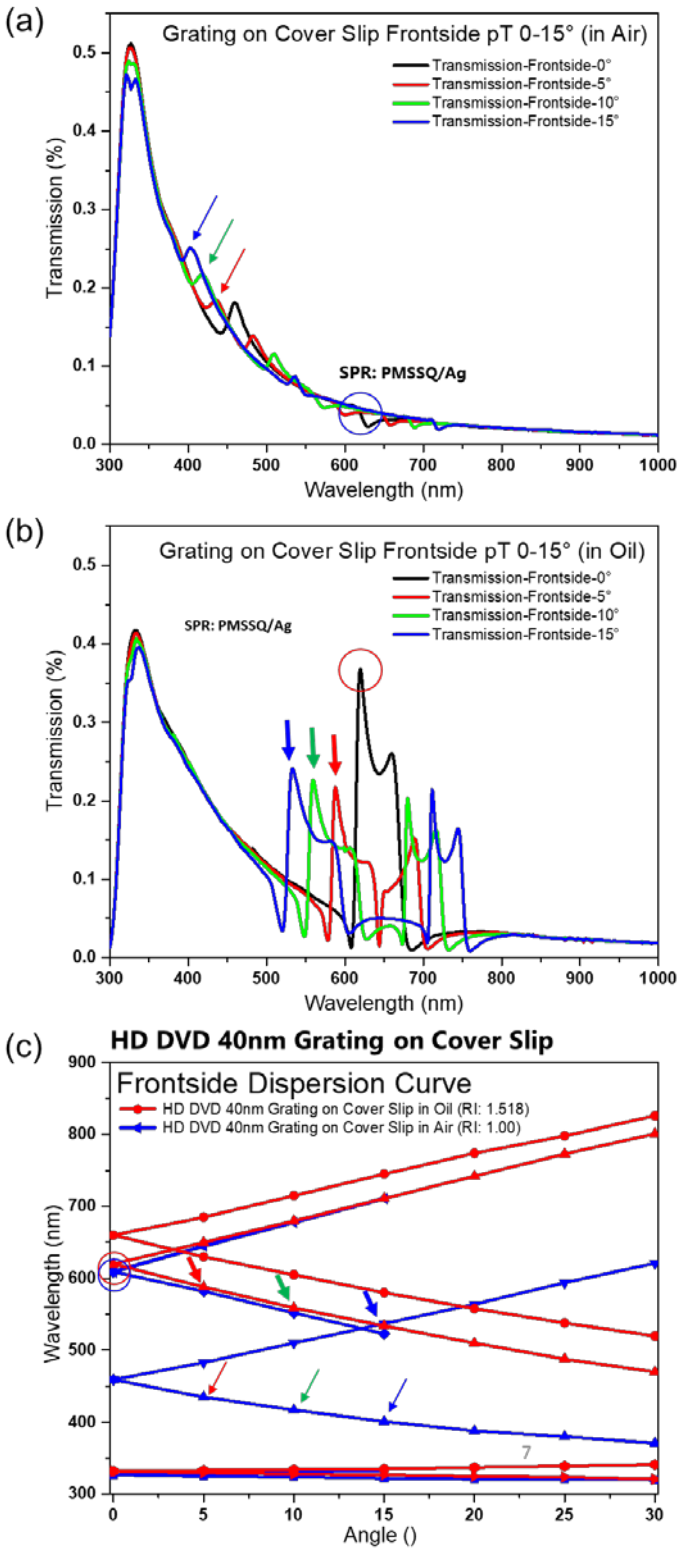

Figure 1-9. Transmission measurement in ellipsometer from the top side of 40nm Ag grating in the air (a) and oil (b) medium is translated into the SPR dispersion curve (c).

1.4.4 Finite Element Method Simulation

Photothermal heating of aluminum nanoparticles by electromagnetic wave irradiation was modeled in Commercial COMSOL Multiphysics software. The Finite Element Method (FEM) was utilized to simulate actual physical phenomena by solving partial differential equations given the analyzed system's geometry, materials, and boundary conditions. For the current study, the method that will be used is called the Sequential Study type, a two-step process that can be used for coupling the physics. In our case, the electromagnetic element is solved in the frequency domain, and cycle-averaged losses are computed. The losses are plugged in as a heat source in a subsequent stationary or transient heat transfer study. The rationale for using the method is that it takes less time and computational resources.

The model will simulate the electromagnetic field distribution and the thermal response of the photothermal heating of Al NP on a plasmonic grating substrate using both COMSOL Multiphysics Radio Frequency and Heat Transfer modules. The first step is using an Electromagnetic Wave, Frequency domain to model the electromagnetic response of an incident source, e.g., laser irradiation on Al NP and grating nanostructures. The second simulation step incorporates the Heat Transfer in Solids to model the transient thermal response and temperature variations.

The first step involves the absorption and scattering cross-sections of free-standing single Al NP in a medium that can be simulated to understand the intrinsic properties of Al NP. The excitation wavelength, the refractive index of the medium, and the size of Al NP are all evaluated to understand their effects on the absorption cross-section. The cross-section can be defined as the net rate of energy absorption (W_{abs}) [W] divided by the incident irradiation (P_b) that is, laser power density or specific

rate of energy transfer [W/m^2]. The absorption cross-section (σ_{abs}) may be larger or smaller than the physical cross-section of the particle itself, as represented by the equation below.

$$\boldsymbol{W_{abs} = P_b \cdot \sigma_{abs}} \quad (1.11)$$

The model is flanked by a Floquet boundary that describes the structure's periodicity. The boundary condition states that the solution on one side of the unit equals the solution on the other before being multiplied by a complex-valued phase factor. Because the periodicity boundaries are parallel with the y-axis, only the x-component of the electric field is required. The following chapters will discuss further details and implications of the absorption cross-section.

The second step is to simulate the laser irradiation on Al NPs and the grating substrate. The plasmonic grating structure is incorporated into the simulation to investigate its effect on the electric field enhancement. Since the electromagnetic coupling of the Al NPs and grating is localized, the plasmonic grating microchip can be represented by three periodic unit cells of the grating structure to shorten the simulation time. The simulation model consists of five domains: (1) the medium, (2) nanoparticle Al core, (3) nanoparticle alumina shell, (4) alumina grating layer, and (5) silver grating substrate. The scheme of the model is shown in **Figure 1-10**.

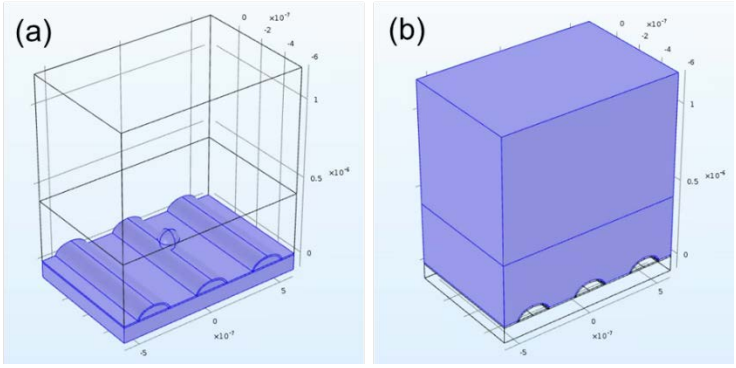

Figure 1-10. Cropped simulation area of three grating pitches illustrates an Al nanoparticle on a grating ridge. The model comprises several domains, including (a) Al nanoparticle on the grating substrate and (b) the air medium. Note that the Al nanoparticle has two domains: the Al core and alumina (Al_2O_3) shell.

The laser photothermal heating of the particle or cluster will act as a heat source obtained from the electromagnetic losses Q_e [W/m^3]. The COMSOL Simulation Electromagnetic Wave Module considers heating due to resistive and magnetic losses, given by:

$$Q_e = Q_{rh} + Q_{ml} \tag{1.12}$$

where the resistive losses are

$$Q_{rh} = \frac{1}{2} Re(\mathbf{J} \cdot \mathbf{E}^*) \tag{1.13}$$

and the magnetic losses are

$$Q_{ml} = \frac{1}{2} Re(i\omega \mathbf{B} \cdot \mathbf{H}^*) \tag{1.14}$$

In the frequency domain, the material properties representing loss are conductivity (σ), complex magnetic permeability (μ''), and complex relative permittivity (ε''). In addition, the model maps the electromagnetic surface losses as an additional heat source on the boundary [W/m^2].

The heat transfer equations in continua are derived from the first law of thermodynamics under the principle of energy conservation. The heat generation rate is used as the input in the thermal conduction equation for calculating the thermal distribution. For solid interface, the equation used in the COMSOL Simulation Heat Transfer Module is expressed by:

$$\rho C_p \frac{\partial T}{\partial t} + \rho C_p \mathbf{u} \cdot \nabla T + \nabla \cdot \mathbf{q} = Q_{ted} + Q_e \tag{1.15}$$

and

$$q = -k \nabla T \tag{1.16}$$

where ρ is the density [kg/m^3], C_p is the specific heat capacity at constant stress [J/(kg.K)], T is the absolute temperature [K], $\mathbf{u}$ is the velocity vector [m/s], $\mathbf{q}$ is heat flux [W/m^2], k is the thermal conductivity [W/(m.K)], Q_{ted} is the thermoelastic damping in solids [W/m^3], and Q_e is the photothermal heat source [W/m^3]. The model ignores the effect of radiative and convective heat transfer since the process is dominated by heat conduction from aluminum nanoparticles and the silver grating substrate.

Table 1-2. Material properties used in COMSOL Multiphysics simulation.

Property	**Thermal conductivity**	**Density**	**Heat capacity**
Unit	*W/(m.K)*	*kg/m^3*	*J/(kg.K)*
Aluminum	237	2600	921
Alumina	27	3900	900
Silver	406	10490	238
THV	2.4	1980	1200
Oil	0.151	900	1900
Air	0.026	1.225	1000

A periodic port placed 1.2 μm above the grating at a 0° incident angle, normal to the substrate, acted as the electric field source. As the laser beam is much larger than the cluster of interest, the electric field source is represented as uniform intensity with a peak power density of 4.2×10^5 W/cm^2. In the heat transfer simulation, a larger model dimension of $10 \times 10 \times 1.2$ μm^3 was applied, with the Al NPs acting as the heat source. All the outside faces of the medium and grating substrate are defined to have scattering boundary conditions so that no inward waves are entering the domain. **Figure 1-11** illustrates the simulation output of the electromagnetic field and the corresponding transient temperature response. Electric field enhancement can be observed in the intensity-color plot representing the electric field coupling at the Al NP and grating interfaces. The temperature plot shows that the aluminum core heats up due to laser photothermal heating and dissipates the heat to its surroundings. The

simulation is essential for estimating the temperature rise given the particle dimension and laser power density. The model will simulate the actual physical arrangement of the Al NPs on the grating substrate from the experiment, which will be discussed in the later chapters.

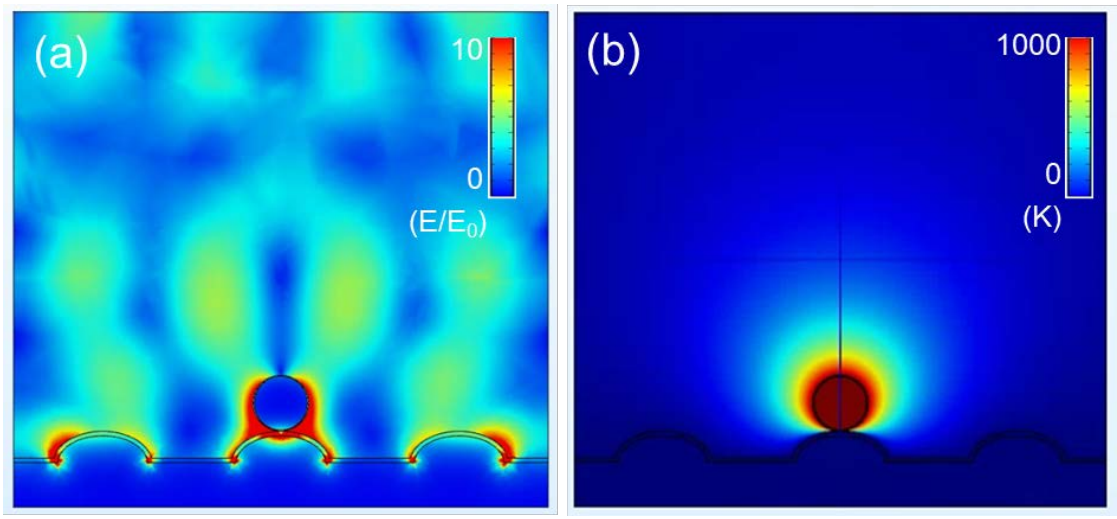

Figure 1-11. Laser photothermal heating of Al NPs on the plasmonic grating substrate is modeled in COMSOL. Cross-sectional views of the simulation result can be plotted as (a) the electric field and (b) the corresponding temperature profiles.

1.4.5 Nanoscale Thermometry

Thermometry at sub-micron length scales has found application in microelectronics [69–71], microfluidics [72–74], and nanomedicine [75–77]. Enhancing the spatiotemporal resolution of temperature sensing techniques can advance their application of a fundamental heat transfer mechanism for small and rapidly heated particles. Current nanothermometry techniques include contact thermometry, scanning thermal microscopy [58,78,79], and micro-thermocouple devices [80]. Non-contact thermometry techniques that elucidate temperature changes noninvasively are particularly attractive, namely infrared thermography [81,82], quantum dot-based fluorescence thermography [83–86], and

organic dye-based luminescence or fluorescence thermography [87–90]. Fluorescence thermography, in particular, offers high detection sensitivity and spatial resolution limited only by the diffraction limit on the order of a few hundred nanometers. Further, the fluorescence thermography technique is compatible with a diverse range of experimental applications, provides *in-situ* spatial temperature maps, and results may be independent of the illumination source [91].

Numerous fluorescence-based experiments have demonstrated the utility of fluorescence thermography. Lanthanide-based dyes undergo upconversion following excitation in the near-infrared and resist photobleaching and photoblinking [92,93]. In particular, Europium-doped materials are well-suited to monitor temperatures up to 1300 K [94,95]. However, lanthanide-doped nanoparticles are frequently micron-scale, limiting their use in high-resolution applications, and offer low luminescence efficiency or quantum yield compared to organic dyes. Several organic dyes, including rhodamine, fluorescein, and triarylboron, have been used for temperature sensing [96–98]. These dyes may be used for temperature detection in aqueous environments such as microfluidic devices or solid polymers [99,100]. In particular, Rhodamine 6G (R6G) has a long history as a dye reporter with a reversible temperature-dependent response owing to thermostability to 250 °C [73,89,101] and high temporal and spatial resolutions [102–104]. Unfortunately, long-duration exposure to exciting radiation may lead to irreversible photobleaching of R6G. The relatively low signal-to-noise ratio of R6G has been insufficient to measure fast-dynamic events and low-temperature differences, limiting the use of rhodamines in nanothermometry. Recently, excitation of fluorophores involving surface plasmon resonance (SPR) coupling of the incident excitation energy at a metal-dielectric

interface (e.g., Ag-Al_2O_3) was shown to enhance the intensity of the dyes by a factor of 100 compared to glass [105–109]. The free-space SPR effect provided by a dielectric-coated metal grating may also enhance the photothermal heating rate experienced by a nanoparticle near the grating surface [50,110].

1.5 Scope of This Dissertation

This dissertation discusses the works that have been accomplished, from investigating the role of each nanoenergetic material constituent on the bulk scale to studying the isolated nanoparticle to understand their mechanism better. **Chapter 1** introduces the background of energetic material and the plasmonic grating platform that will be used in the following chapters. **Chapter 2** reports the spallation of isolated aluminum 120-nm nanoparticles on a graphene layer on the plasmonic grating substrate. Rapid photothermal heating, assisted by the plasmonic-enhanced electromagnetic field, will be used to provide a fast-heating rate sufficient to observe nanofragment dispersal. **Chapter 3** is the comprehensive study of Chapter 2. Photothermal heating of isolated aluminum nano- and micron-particles will be conducted on a bare grating substrate and MoO_3 flakes. An extensive study of different nanoparticle sizes and mediums will be investigated in this work.

Chapter 4 discusses the synthesis and observation of macro-scale energetic reactions comprising Al NPs and layered materials, 2D MoO_3. The materials show the effect of constituents' proximity between the fuel and oxidizer to enhance their combustion performance. Thermal and reactivity characterization techniques will be introduced in this chapter, along with sets of electron microscopy imaging and elemental analysis.

Chapter 5 discusses the study of Al NPs laser-heating assisted by polymer nanoenergetic. In-situ laser-induced ignition of nanoenergetic systems consisting of Al NPs embedded in polymer oxidizers on plasmonic gratings will be examined using optical microscopy. Teflon, THV, and nitrocellulose (NC) are the polymers of interest. They are selected due to diverse physical and reactivity characteristics and processing feasibility. The combustion dynamics of reactive materials will be investigated by imaging laser-ignition with high-resolution and high-speed color cameras. The high spatial resolution images were sufficient to facilitate Al NP counting. In contrast, the high temporal resolution was beneficial in quantifying the reaction mechanism and estimating reaction temperature using two-color pyrometry.

Chapter 6 discusses in-situ photothermal heating to investigate the spatiotemporal temperature dependence of Al NPs. In-house tunable laser synchronization control is developed to achieve a focused, high-power-density heating source. The nanoparticles are suspended in a THV film, while Rhodamine6G (R6G) dyes are embedded in the film and used as temperature sensing tools. An external laser photothermally heats individual Al NPs, and the time-resolved fluorescence is recorded. The fluorescence intensity is converted to temperature maps via controlled calibration. The maps are then projected into radial temperature profiles whose curve fittings are used to calculate the heat transfer rate of the Al NP into the THV matrix. These in situ techniques provide direct visualization and measurement of local temperature to better understand the combustion mechanism.

.

CHAPTER 2 : SPALLATION OF ISOLATED ALUMINUM NANOPARTICLES BY RAPID PHOTOTHERMAL HEATING

The spallation of isolated aluminum nanoparticle (Al NP) clusters is triggered using rapid photothermal heating. The Al NPs exhibited a nominal diameter of 120 nm, with an average oxide shell thickness of 3.8 nm. The NPs resided on an optical plasmonic grating and were irradiated by a focused 446 nm wavelength laser. The resulting plasmonic coupling enhanced the local electric field by a factor of up to 10 compared to a plane glass substrate and generated an Al NP heating rate on the order of 10^8 K/s. Numerical simulation demonstrates that Al NPs experiencing full laser intensity reach temperatures between 1000 – 1600 K. In large Al NP clusters, the particles undergoing direct laser irradiation exhibit spallation, while NPs adjacent to the laser sinter together. We propose that the observations and experimental conditions are consistent with those anticipated for the thermomechanical melt dispersion mechanism (MDM). We believe our observations of spallation are the first of their kind for Al NPs.

2.1 Introduction

Aluminum nanoparticles (Al NPs) have attracted interest as a reactive metal fuel additive in energetic materials due to their high energy density, low cost, and commercial availability [48,111,112]. Applications of Al NPs include solid propellants, explosives, and enhanced combustion of metastable intermixed composites [113–115]. To react with surrounding oxide, the metallic Al core of Al NPs must escape an encapsulating alumina shell. Understanding the fundamental escape mechanisms of Al fuel through the shell is crucial to optimizing their use in diverse applications. Various mechanisms have been proposed based upon the NP heating rate, including

the diffusion oxidation mechanism (DOM) and the melt-dispersion mechanism (MDM) [54,116,117]. DOM is observed in a slower heating rate regime (10^4-10^6 K/s), in which reaction is initiated by diffusion of the Al and O atoms through the core-shell interface or the outer surface of the Al NP [10] [118]. In the DOM mechanism, the Al core of NPs is nearly isothermal due to the NP's small physical dimensions and high thermal conductivity, and Al diffusion through the encapsulating shell restricts the reaction rate between the fuel and surrounding oxide. The outward diffusion of Al is more rapid than the inward diffusion of oxygen, causing the coarsening of the amorphous oxide layer, as shown by MD simulation and experimental observations [119,120]. At a temperature of 770 K, a polymorphic phase transformation of the oxide shell may initiate the nucleation of high-density crystallites [121]. These crystallites are accompanied by the formation of small voids at their boundaries that may accelerate the escape of Al [122,123]. The MDM model proposes that rapid heating, melting, and expansion of the Al core produces sufficiently high hoop stress on the alumina shell to induce mechanical failure and spallation of the Al core. Activation of this effect requires specific conditions, including very high heating rates (10^7-10^9 K/s), a core temperature that exceeds the melting temperature of Al (933 K), and a sufficiently homogeneous alumina shell that can withstand the building pressure provided by the Al core [49]. Shells with pre-existing defects, including nanovoids, impurities, and heterogeneous shell thickness, may hinder the occurrence of MDM [51,124].

Promoting the rapid spallation and ejection of molten Al fuel, as proposed by the MDM model, could drastically increase the reaction rates of nanothermite systems. However, experimental validation of MDM, or other dispersive reaction mechanisms,

has not been provided in the literature to the authors' best knowledge. In one targeted attempt to experimentally isolate the MDM mechanism, clusters comprised of approximately 100 Al NPs were heated using a 12 ns pulsed 1064 nm wavelength laser or a thin-film MEMS heater within a transmission electron microscope (TEM) [53]. The Al NPs for this experiment were nominally 80 nm in core diameter, with an estimated 3 nm oxide shell thickness. Based on finite element electromagnetic simulations, the laser absorption (and thus heat generation) was largely isolated to hot spots located at the contact point between Al NPs. These experiments failed to demonstrate Al spallation. Rather, adjacent NPs coalesced to form a large particle without evidence of the MDM mechanism. The projected heating rates of the Al NPs ranged between 10^6 -10^{11} K/s, estimated based on laser pulse time and the minimum observed temperature to promote Al NP coalescence (1300 K) obtained from controlled resistive heating experiments. However, underestimation of alumina shell thickness and insufficient temperature to induce the MDM mechanism has been suggested as explanations for the observed sintering rather than MDM [51].

2.2 Materials and Methods

In this work, we use optical microscopy to identify and photothermally heat isolated clusters of Al NPs. The Al NPs have a nominal diameter of 120 nm (Novacentrix M2692 Al-120-P). Our TEM analysis showed an average NP size of 110.91 ± 26.27 nm with an oxide thickness of 3.76 ± 0.99 nm. A 446 nm diode laser, focused using a 40x (air) objective, supplied heating as shown in **Figure 2-1**. This laser wavelength was selected due to localized electromagnetic enhancement from both the grating substrate and the plasmonic peak of Al NPs [50]. The following section will discuss further details regarding photothermal absorption using numerical analysis.

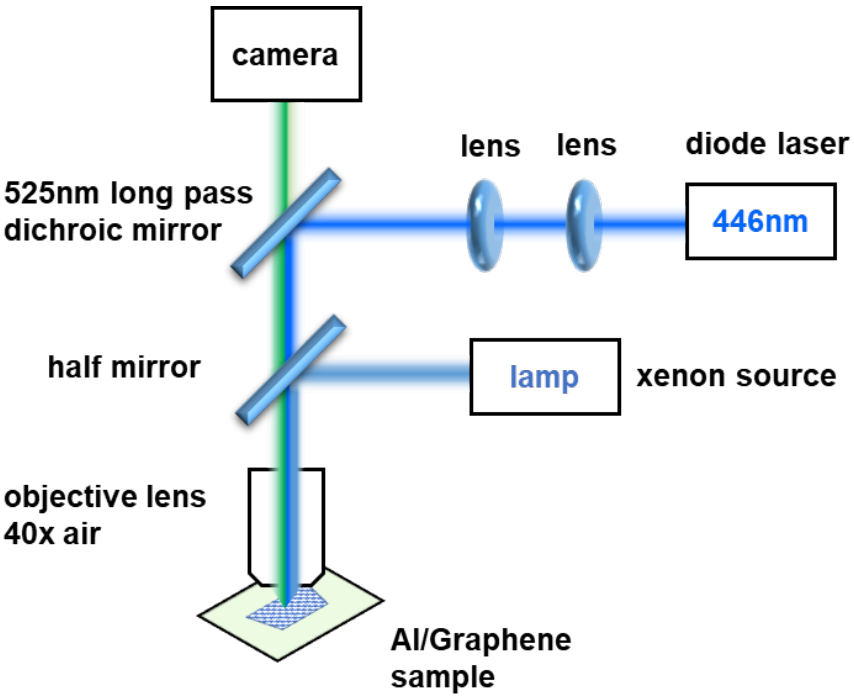

Figure 2-1. Experimental schematics incorporating 446 nm blue diode laser focused onto the sample using 40x air objective lens

The width and breadth of the laser profile may be observed by the dashed outline in **Figure 2-2**, representing the full-width half-maximum (FWHM) of the laser spatial profile. The laser has a 7 µs rise time to reach a peak power of 7.6 mW and power density of 4.2×10^5 W/cm^2 (see figure below).

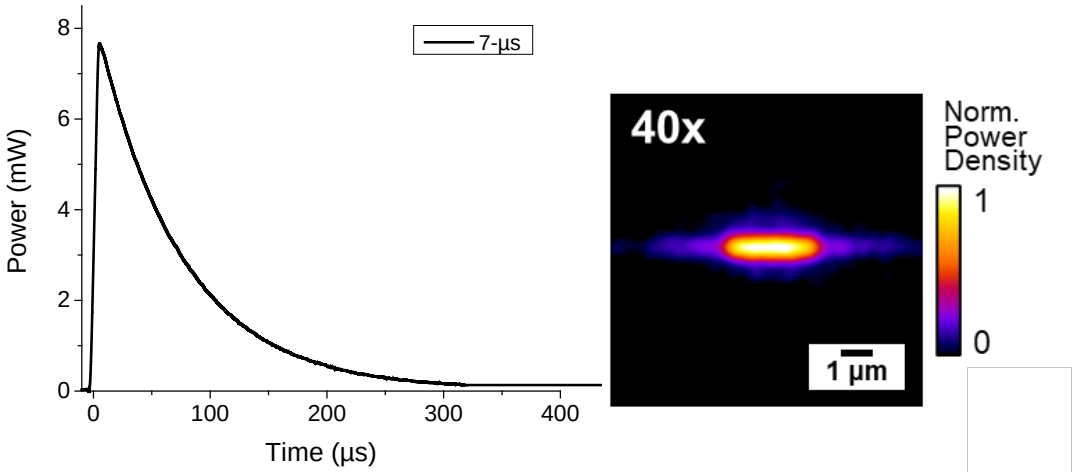

Figure 2-2. (Left) The graph represents the laser temporal profiles at their actual power during the corresponding experiment is the 7 us pulse with 7.6 mW peak power. After 7 us, the profile slowly ramping down as the laser discharges. (Right) Spatial profile of the laser focused on the substrate is represented in a normalized false-color image.

An optical grating substrate was used in all experiments to increase optical image resolution and enhance laser coupling to Al NPs [68,108,125]. The grating features a 400 nm pitch and 60 nm peak-to-valley ridge height [126,127]. As shown in the supplemental information, the optical grating enhanced the absorption cross-section of a 120 nm diameter Al NP by a factor of approximately 8-10 relative to isolated Al NPs in air. To assist the visual observation in differentiating between the grating silver grains and the post-reaction products, a single-layer graphene sheet (Trivial Transfer Graphene, ACS Material) was placed on the grating substrate [128]. The presence of graphene layer was verified by Raman spectroscopy and SEM. The Al NPs were dispersed in isopropyl alcohol (0.01 mg mL-1) and sonicated for 2 hours before their dispersal on the grating substrate. Then, 5 µL of the Al NPs solution was drop-casted onto the sample and air-dried before performing the experiments.

2.3 Experimental Result

Atomic force microscope (AFM, Innova Bruker) images, shown in **Figure 2-3**, display representative clusters of Al NPs that were heated in our studies. The well-defined grating surface indicates that the graphene sheet conformed well to the grating surface.

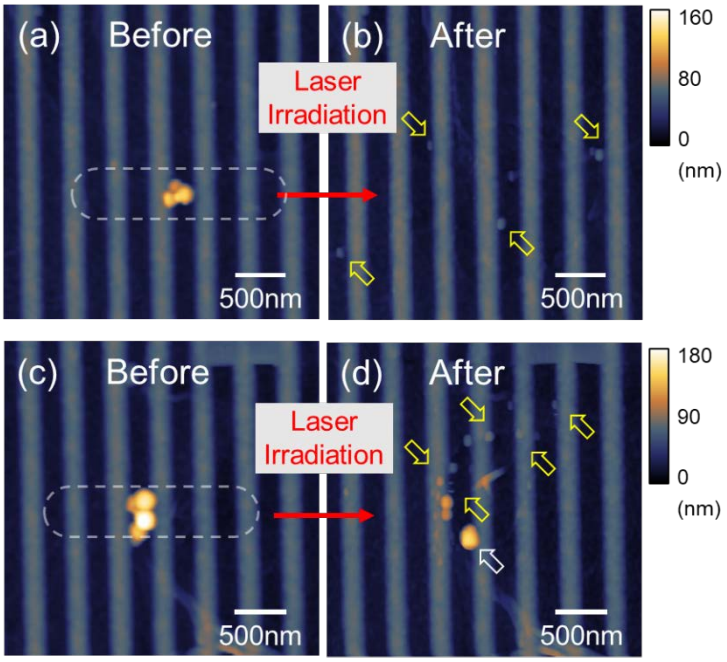

Figure 2-3. (Color online). The evolution of sample morphology due to laser irradiation was measured in AFM microscopy. (a, c) High-resolution AFM images show Al NPs residing on a single graphene sheet on the plasmonic grating microchip. The dashed line represents the full-width half-maximum of the laser spatial profile. After a laser pulse irradiated the NPs, (b, d) AFM images revealed post-ignition products with fragment dispersal locations indicated by yellow arrows, while the unreacted particle is indicated by the white arrow. The periodic ridges in the background represent the morphology of the underlying plasmonic grating substrate.

Evidence for spallation in response to photothermal heating can be observed within a cluster of 4 Al NPs using AFM topology images, displayed in **Figure 2-3(a, b)**. The figures represent before and after laser pulse irradiation, respectively. No evidence of the original Al NPs was observed after the heating; instead, a dispersal pattern of smaller fragments was present that extended radially more than 500 nm

beyond the initial perimeter of the cluster. Considering the laser-induced heating occurred within the irradiation time and assuming Al melting temperature (933 K) was the minimum temperature required to facilitate the spallation, a heating rate of greater than 10^8 K/s may be estimated. The dispersed nanoparticle fragments suggest a rapid material release generated from high pressure, with no large fragments (>50 nm) discernable after the reaction. All Al NPs in the cluster were heated nearly uniformly in this example because all particles were well within the full-width half max of the laser intensity profile, overlayed on **Figure 2-3(a)**. By contrast, **Figure 2-3(c, d)** shows a cluster of Al NPs in which one NP was located slightly outside the peak laser intensity. The lower-most particle resided outside the central heating zone and experienced a laser flux approximately 60% lower than surrounding particles. While the 3 Al NPs that received the full laser irradiation intensity appear to have experienced spallation (yellow arrows), we believe that the particle that received lower laser fluence did not rupture, as observed by the lower-most particle in **Figure 2-3(d)** (white arrow). Notice that the graphene wrinkles at the bottom center of **Figure 2-3(c-d)** present a stationary reference point. Accordingly, the large particle translated approximately 25 nm to the right during the reaction, from the left side of a grating through to the right side. Fragment particles smaller than 50 nm observed on the graphene sheet may represent oxidized Al from the core on the graphene surface. Energy Dispersive X-ray spectroscopy via scanning electron microscopy could not distinguish the composition of the fragmented material due to the small feature size and the significant alumina layer contained within the underlying grating structure.

To better refine the photothermal heating response of Al NPs in the current experiment, the electric field distribution and the transient thermal response were

simulated numerically using the finite element software (COMSOL Multiphysics 5.2a). The numerical simulations have been used in numerous recent reports [24,129,130] and were preferable to the analytical solution in solving partial differential equations (PDE) for hetero-structured models. The spectral absorption of an Al NP was first evaluated and was represented by the absorption cross-section based on Mie theory. The individual nanoparticle of 90, 120, or 150 nm diameters was simulated with a 3 nm alumina shell surrounded by air. The same Al NP was then simulated while resting on the ridge of a plasmonic grating substrate to determine the electric field enhancement. The transient thermal response of Al NPs on the grating surface was then modeled by using the Al NP energy absorption as an input to the 3D heat equation.

The spectral absorption plot (see **Figure 2-4**) for isolated Al NPs shows that the dielectric loss peak is located at 810 nm for all Al NP diameters, while the plasmonic peaks red-shift and broaden as the Al NP diameter increases, similar to other reports [101].

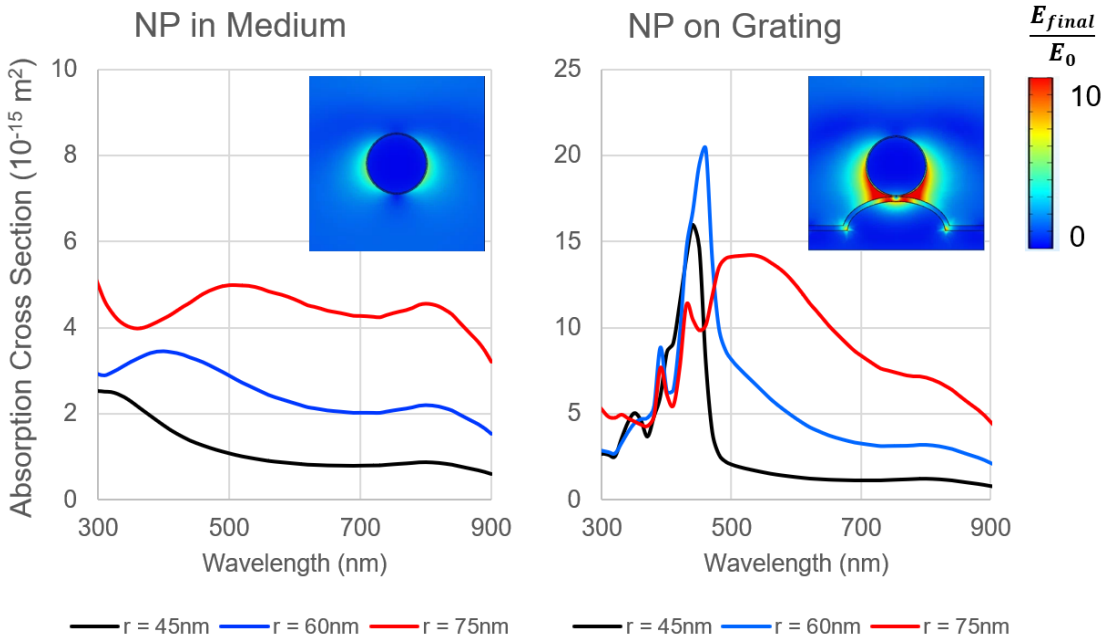

Figure 2-4. Absorption cross section as a function of the wavelength for a single aluminum nanoparticle with an oxide shell of 2 nm and core radius of 45, 60, and 75 nm (a) suspended in air medium and (b) residing on grating substrate. The corresponding insets represent the electric field distribution at 446 nm source excitation with normalized intensity (0-10) to the initial port input.

The effect of the plasmonic grating substrate on the absorption cross-section of Al NPs was simulated by considering an isolated Al NP residing on the ridge of the silver plasmonic grating substrate. The exact configuration of Al NP clusters experimentally observed in **Figure 2-5(a, e)** was then simulated using COMSOL. The model incorporated the AFM-measured size and morphological arrangement of the Al NPs relative to the grating substrate to match the actual experimental condition as closely as possible **Figure 2-5(b, f)**. The coupled electromagnetic field interaction enhanced the energy absorption by 8-10 times relative to an Al NP heated in the open air as shown in **Figure 2-5(c, g)**.

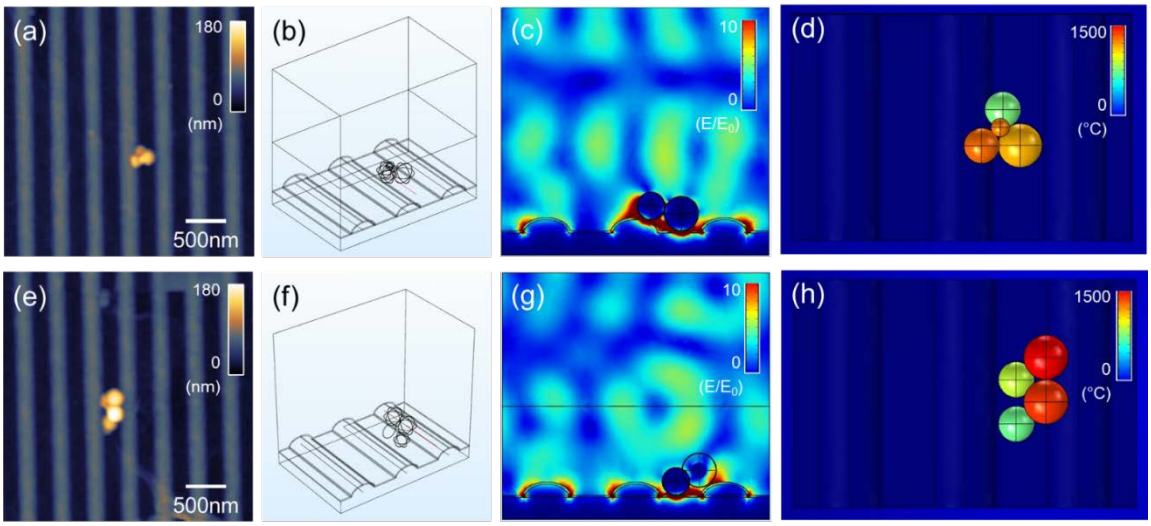

Figure 2-5. (a, e) High resolution AFM image showed Al NPs residing on a single graphene sheet on the plasmonic grating microchip. (b, f) 3D simulation model represents three grating pitches to simulate the experimental NP arrangement prior to laser irradiation. COMSOL simulation shows (c, g) cross-section of electric field distribution and (d, h) thermal response at t = 7 μs.

In the COMSOL simulation, the horizontal span of three grating pitches was modeled to reduce the computational workload, while the scattering boundary condition was applied so that no inward waves were entering the domain. The electric field source was a periodic port placed 1.2 μm above the grating at 0° incident angle, normal to the substrate. As the laser beam is much larger than the cluster of interest, the electric field source is represented as uniform intensity with a peak power density of 4.2×10^5 W/cm^2. In the heat transfer simulation, a larger model dimension of $10 \times 10 \times 1.2$ μm^3 was applied, with the Al NPs acting as the heat source. Most particles contacted the underlying grating, which itself served as a heat sink. The electromagnetic simulation determined the volumetric heating for each particle. For the simplified thermal model, phase change heat transfer was neglected, and the Al was treated as a solid material regardless of temperature.

Table 1. Peak temperatures for all nanoparticles simulated in COMSOL.

	Figure 2-6 (a)		Figure 2-6 (b)	
Particle	Radius (nm)	Peak Temperature (K)	Radius (nm)	Peak Temperature (K)
1	60	1435	75	1610
2	30	1400	75	1520
3	60	1328	60	1135
4	75	1035	60	1012

The transient temperature for each particle within the two cluster configurations is shown in **Figure 2-6**. The temperature profiles for all NPs followed the laser intensity temporal profile trend. The characteristic thermal rise time of the Al NPs computed as $\tau_p \approx r^2/4\alpha_p$, where α_p is the thermal diffusivity of the particle [129]. For an Al NP with $\alpha_p = 0.83\times10^{-4}$ m^2s^{-1} and radius $r \cong 60$ nm, the characteristic time $\tau_p \approx 10^{-12}$ s, orders of magnitude faster than the laser rise time. The simulation shows that the aluminum core temperature within a given particle varied less than 6-10 K. **Table 1** summarizes the simulated peak temperature for all nanoparticles in **Figure 2-6** corresponding to the experimental configuration in **Figure 2-3**. For the particle assembly in **Figure 2-6(a)**, all particles reach between 1,000 – 1,500 K within the duration of the laser rise time of 7 μs, generating a heating rate of ~1-2 $\times 10^8$ K/s. The melting temperature of aluminum is 933 K. Note that in this simulation, all Al NPs reside within the region of maximum laser intensity. The fast-heating rate can be attributed to both electric field enhancement of the plasmonic grating and heat accumulation of multiple nanoparticles acting as heat sources. For the particle assembly shown in **Figure**

2-6(b) (corresponding to the experimental configuration in **Figure 2-3(b)**), particle 4 does not receive the full heating intensity because it lies outside the FWHM laser intensity. While the particles reach similar or greater temperatures than those simulated in **Figure 2-6(a)**, the maximum temperature of 1,000 K reached by particle 4 (r = 60 nm) in **Figure 2-6(b)** may not be sufficient to induce spallation because of the relatively small diameter compared to that of particle 4 (r = 75 nm) in **Figure 2-6(a)**. According to the MDM mechanism, spallation is triggered at increasingly more significant temperatures as the ratio of shell thickness to Al radius increases [51]. In other words, larger diameter particles are expected to be activated by the MDM mechanism at lower temperatures than smaller diameter particles. Assuming a 3 nm shell thickness, an 80 nm diameter Al NP would fracture at 1107 K, while a 35 nm diameter Al NP would fracture at 1805 K [51]. While the authors do not conclusively claim that the MDM mechanism generated the reactions observed by rapidly heated Al NPs, we believe that the particle diameter, shell thickness, heating rate, and core Al temperatures generated in our analysis are consistent with MDM criteria.

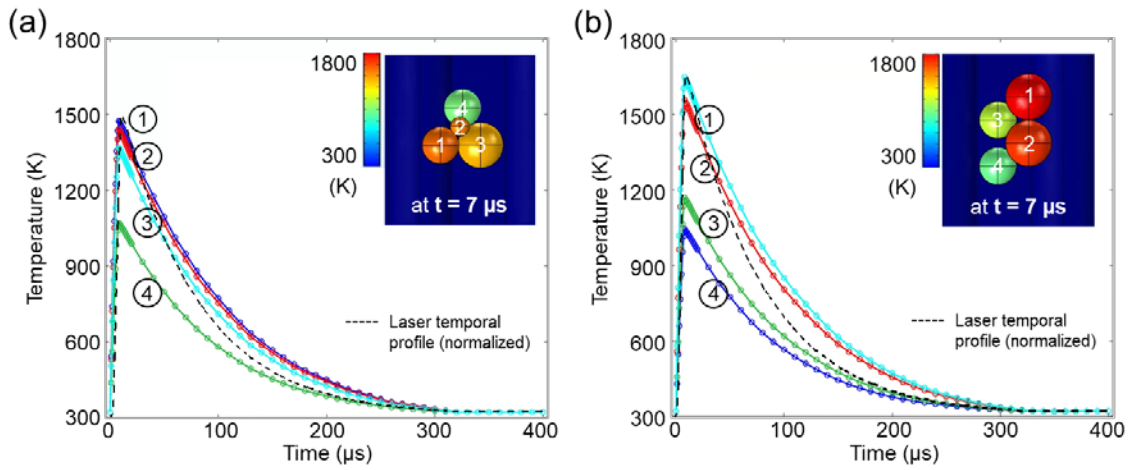

Figure 2-6. (Color online). The particle core temperature of the corresponding 4 Al NPs (insets) represents thermal response as a function of time. The laser temporal profile has been plotted in a black dotted line and normalized to the peak temperature.

When the Al NP cluster size greatly exceeds the laser-heated area, the NPs within a cluster may undergo drastically different heating rates. The AFM topology image in **Figure 2-7(a)** shows a large, 3D cluster of ~65 Al NPs heated at the power density (4.2×10^5 W/cm^2) and rise time (7 μs) used to trigger Al spallation previously. In this scenario, many Al NPs lie completely outside of the laser-irradiated zone or are shielded from direct line-of-sight irradiation by vertical Al NPs stacking. Evidence of two different reaction mechanisms (spallation and sintering) is evident in **Figure 2-7 (a-c)**. The Al NPs in and above the heated region are absent after heating and are replaced by a field of smaller fragments. Small, irregular fragments are observed within 2 μm from the center of the laser-heated zone. Note that there are no fragments beyond the field of view shown in the SEM and AFM images shown in **Figure 2-7**. Based on the three-dimensional AFM topology, each fragment was converted into an equivalent hemisphere to estimate particle diameter. The large, sintered particle was estimated to be a sphere. A histogram of the equivalent diameter of the fragments is shown in **Figure 2-7(d)**. The average fragment diameter of approximately 21.9 nm is drastically smaller than the initial Al NP diameters. The loss of volume was estimated at approximately 23% from **Figure 2-7(a)** and **Figure 2-7(b)**. This volume reduction can be attributed to the loss of mass by vaporization [53] or caused by error sources from the estimation method. The spallation reaction was sufficiently energetic also to induce tearing of the graphene layer. The tears in the graphene sheet align approximately to the same region heated by the laser but extend further than the direct irradiation zone. Additionally, small particles decorating the perimeter of the torn graphene may indicate that the graphene was consumed in a reduction reaction with the Al fuel as it escaped the alumina shell. Although the energy carried by the ejected

Al material in the direct laser heating zone was insufficient to trigger a sustained chain reaction of spallation events that propagated through the entire Al NPs cluster, the heating was sufficient to induce sintering of many particles that were subject to no direct laser heating. We believe that the Al NP spallation occurred only for the NPs located within the direct laser profile.

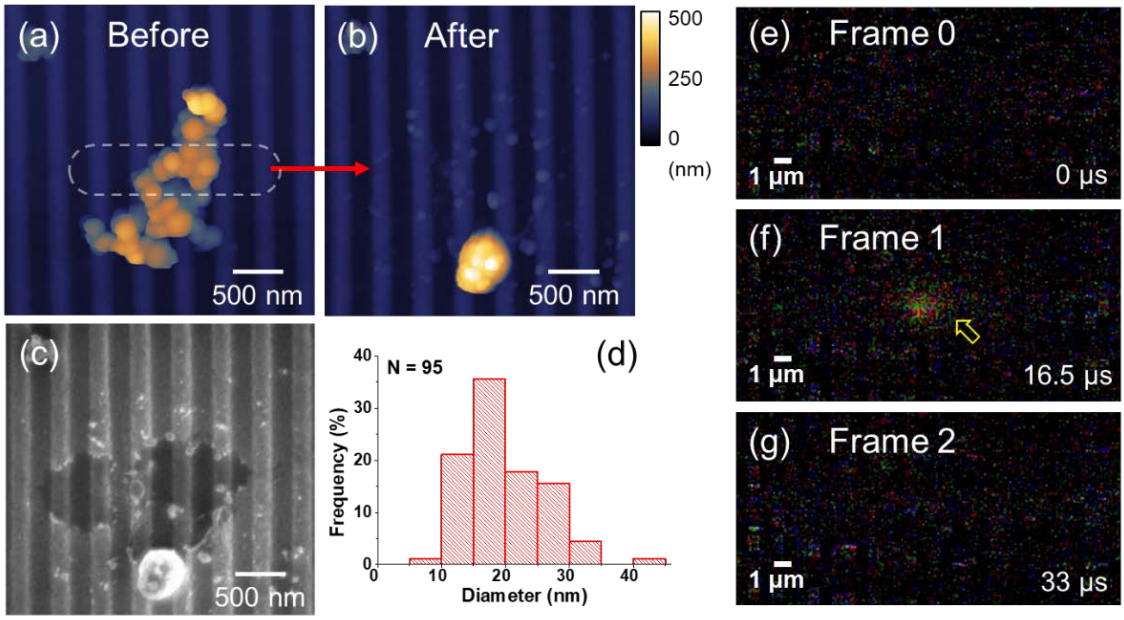

Figure 2-7. (Color online). (a) AFM images of Al NPs residing on a graphene sheet on the plasmonic grating microchip. After a laser pulse irradiated the NPs, high resolution (b) AFM and (c) SEM images revealed post ignition products. (d) A histogram of the size distribution of the dispersed nanofragments less than 50 nm was plotted, while the frequency of larger fragments is negligible. (e-f) High speed imaging was able to capture the photothermal heating reaction.

The reaction of large clusters, similar to that shown in **Figure 2-7(a-b)**, was also investigated using high-speed imaging. A high-speed Phantom camera was used to record the photothermal heating using a frame rate of 60,606 frames per second (16.5 μs per frame). The synchronized system allowed the laser to be triggered simultaneously with the first frame of the camera. Therefore, the laser rise time of 7 μs was designed to be well within the first frame. The images (**Figure 2-7(e-g)**) clearly

show that a light-generation reaction occurred within the first exposure, indicating a high-temperature reaction of Al fragments to oxygen in air. Note that only high photon intensity is sufficient to register at the exposure time used in the experiment. The diameter of the bright spot generated by the reaction is on the order of 500 nm, similar to the initial diameter of the Al NP cluster. Because of the ejected material's small scale and the relatively low photon intensity that they would generate, we would not anticipate visualizing ejected particles with this experiment. The instruments used here do not have the spatiotemporal resolution to probe the physical mechanisms generating the Al NP reactions observed.

2.4 Conclusion

Our observations clearly show that rapid, high-intensity heating of isolated NP can cause the spallation of nanoscale aluminum nanoparticles. The MDM is one potential mechanism to promote Al spallation, and the physical parameters of the NPs (diameter, shell thickness), heating rate (10^8 K/s), and maximum temperature (1000 – 1600 K) employed in this experiment are consistent with those required to promote MDM. Other ultra-fast excitation mechanisms, including Coulomb explosion from the ejection of hot electrons [131,132] require heating rates that are orders of magnitude greater than those observed here. While we do not anticipate electron emission, strong plasmonic coupling may play a role in our observations, and additional investigation is being pursued in this area. The spallation reactions were not readily sustained between adjacent NPs in contact, as large-scale sintering of NPs adjacent to the irradiated zone was observed. We hypothesize that similar Al NPs heating rates may be achieved within the reaction of mesoscale and macroscale assemblies of Al and oxidizer NPs when particle packing and equivalence ratios are achieved in

nanothermite systems. Enabling this Al NP reaction mechanism at a larger scale may further enhance the reaction rate and reaction temperature for nanothermite systems. Future parametric studies will elucidate structure-property relationships of the spallation reactions and will help identify and control the underlying mechanism.

CHAPTER 3 : PHOTOTHERMAL HEATING OF ALUMINUM PARTICLES ON MOLYBDENUM TRIOXIDE FLAKES

This work is the extension of the experiments conducted in Chapter 2. The reaction mechanisms of isolated energetic particles was experimentally studied before comparing them to traditional bulk material combustion behavior. Here, various sizes of nano- and micron aluminum (Al) particles with a core-shell structure are individually heated while residing on the top surface of 2D molybdenum trioxide (MoO_3) flakes via photothermal heating. The plasmonic grating structure enhanced the electromagnetic field and provided enhanced heating rates. Post-reaction images show that spallation can be achieved for both cases of nano-Al particles on a bare grating substrate and residing on MoO_3 flakes on a grating substrate. Results indicate that 1) a plasmonic grating substrate enhances the heating rate to cause spallation only for nano-Al particles, and 2) hot ejected molten fuel can react locally to the surrounding oxidizer. Additionally, the same laser setup was not able to react micron-Al particles. In contrast, spallation was observed for micron-Al particles residing on MoO_3 flakes using similar laser setup. The investigation is crucial to better understand the determining factors of spallation and the governing reaction mechanism.

3.1 Introduction

Investigating aluminum particles' localized reactions and oxidation mechanisms with metal-oxide oxidizer can attract significant attention especially due to its high energy density [39,40,42]. The improved combustion performance of nano-scale aluminum particles compared to micro-scale aluminum particles has been widely studied [26,49,133]. Nanoscale energetic materials, which are comprised of nanoscale fuel and oxidizer constituents, greatly benefit from the enhanced surface

area of interaction [29,115,134]. Reduced particle dimensions improve the homogeneity of the mixture, decreasing the distance required for reactions [49,135,136]. Like the nanoscale fuel constituent, layered 2D oxidizer materials have continued to draw increased attention for many applications due to their superior combustion performance and enhanced properties [13,30,137].

The previous dissertation chapter used plasmonic grating substrates to spall nano-Al (120 nm) particles using photothermal heating. Our observation indicates that the source's heating rates and products' morphology are in-line with the prediction of melt dispersion mechanism (MDM) theory. According to MDM, a spallation event can produce Al ejecta when the particles are heated at a rate of 10^6-10^9 K/s [45]. The fast heating causes the Al core temperature to rise beyond the Al melting point, accompanied by rapid Al core expansion. As a result, high tensile pressure at the alumina shell is followed by dynamic spallation [45]. The dispersing hot ejecta at high velocity may readily react to an oxidizing agent if any oxidizer materials are presently at proximity. Therefore, in the later section of this paper, MoO_3 flakes will be introduced in proximity to the Al particles.

To the best of the author's knowledge, no reported works have observed the MDM reactions at the particle scale to test the existence of MDM. In contrast, available reported results have been conducted on larger and bulk scale experiments [47,49,124]. At a low heating rate of 10^4-10^6 K/s, the diffusion oxidation mechanism (DOM) describes the diffusion of Al and oxygen atoms through an oxide shell [116,121]. Similarly, another report observes Al content escaped the alumina shell, then reacts to nearby oxidizer at a lower heating rate of ~10^2 K/s [110]. The proposed reaction mechanism is that Al adatoms diffusion along the energetically

preferential direction. The extended α-Al_2O_3 streaks in the ⟨001⟩ direction are believed due to surface diffusion and subsequent sub-surface adsorption of Al into the α-MoO_3 lattice.

In this experiment, we hope that the reaction products can help determine whether the reaction mechanism follows melt-dispersion or diffusion oxidation mechanism. Simultaneous chemical and thermomechanical mechanisms in Al NPs were investigated using photothermally activated experiments. This chapter will summarize several sets of extensive experiments and simulations.

- First – a COMSOL numerical model will simulate the laser heating experiment
- Second – rapid laser-heating experiments on isolated Al NPs will be conducted. The expected results include ejected Al molten materials (hot ejecta), sintered Al aggregate or local Al melting.
- Then, MoO_3 will be introduced at proximity acting as an oxidizing agent. In Al/MoO_3 experiment, the presence of a readily available MoO_3 will provide an oxidizing agent for the Al ejecta to react.
- Finally, a comparison to the reported literature will be discussed to evaluate many proposed reaction mechanisms. The analysis will shed light on the parameters governing the nanofragment spallation via photothermal heating.

3.2 Materials and Methods

Setup Details. Experiments to capture the post reaction product and potentially reaction temperatures via two-color pyrometry are proposed using the established

100x air optical microscope Olympus BX51system. A high-resolution 32MP (6464-pixel x 4864-pixel) Infinity-X32 camera observes the before-and-after laser irradiation. The Infinity camera has an 81.67 pixel/micron or 12.24 nm/pixel measured resolution. As a comparison, the previously used 2.8 MP (1920-pixel x 1440-pixel) Hamamatsu camera (in Dissertation Chapter II) has a 27.5 pixel/micron or 36.36 nm/pixel resolution in a similar setup.

Further, two imaging modes are used in this experiment, namely bright field and scattering modes. Bright-field imaging is used to locate a sample and focus the laser onto the target nanoparticles. Polarization-based scattering is used before and after nanoparticle heating to determine the presence of Al and Al_2O_3. Reacted Al NPs in the form of alumina will appear dark as the reacted oxide material does not scatter light compared to strongly scattering metallic Al. Al NPs scatter light under this imaging condition, while alumina primarily absorbs light [50].

Combining the high-definition objective lens, high-resolution camera, and coupling of the grating in the air medium facilitates subwavelength resolution to visualize morphological changes in the particles of interest. The experiment will incorporate the aluminum nanoparticles (nano-Al) with diameters of 50, 80, and 120 nm and aluminum micron-particles (micron-Al) with a diameter of 3-4.5 μm. At least 50 particles were measured by TEM to obtain the statistics of each particle's diameter and shell thickness. Results are presented in the table below.

Table 3-1. Aluminum particle physical dimensions are characterized in TEM.

Particles Size	Measured Particle Diameter (nm)	Alumina Shell Thickness (nm)	Relative Particle Size Radius/Shell Ratio
50 nm	55 ± 20.3	2.6 ± 0.74	10.12
80 nm	81 ± 21.1	3.3 ± 1.08	12.41
120 nm	111 ± 26.3	3.8 ± 0.99	14.73
3-4.5 μm* [49]	2990 – 4496	4	374-562

Plasmonic Grating Dispersion Curve. The dispersion curve of the grating substrate with a 100-nm Ag layer was compiled from the reflectivity and transmission ellipsometer data shown in **Figure 3-1**. Several things are crucial in determining the laser and sample medium to design the most optimum coupling configuration. For instance, a 638 nm red laser is well coupled to the grating substrate in the oil medium at a 0-degree angle. This may promote more coupling of the e-field on the grating, especially when coupled with Al NPs. On the other hand, 808 nm IR-laser experiences much less grating coupling in oil or air medium. Since the experiment will be conducted in air at a 0-degree laser excitation angle, selecting a 446 nm blue laser can provide the most optimum configuration as a photothermal heating source.

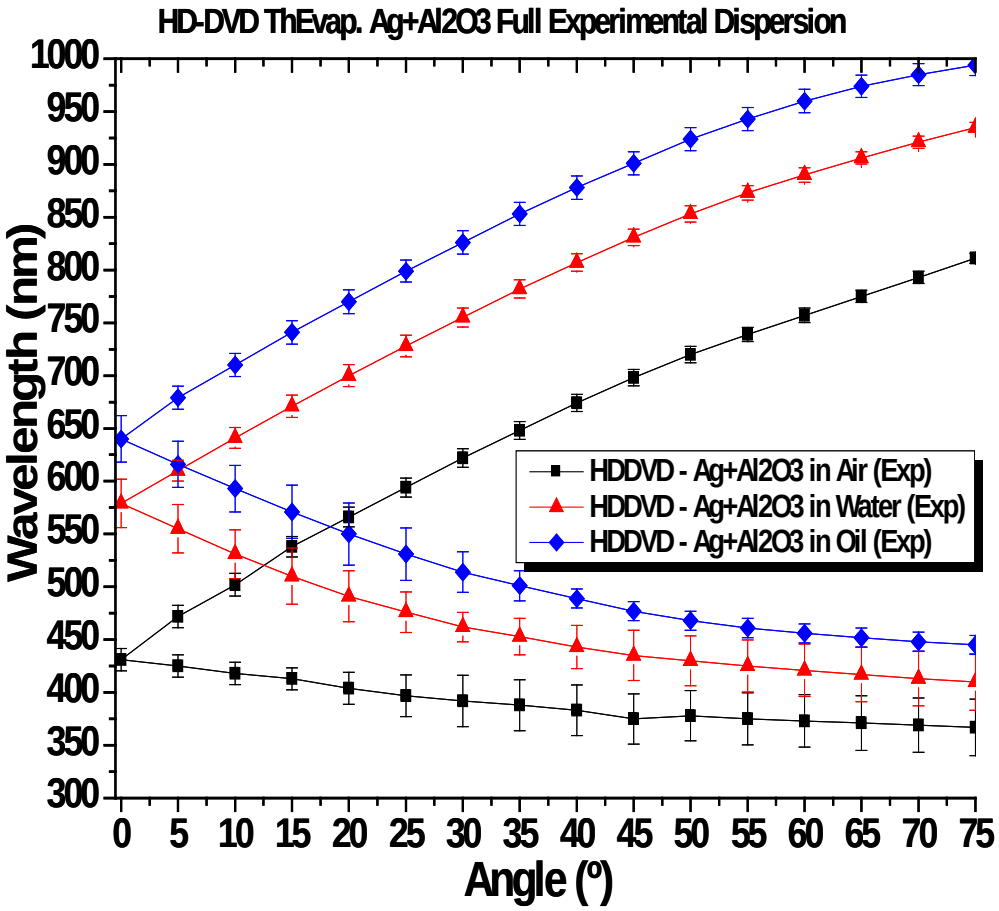

Figure 3-1. Dispersion curve of 100 nm Ag grating measured by ellipsometer in several media: air, water, and oil. The grating of interest has a pitch length of 400 nm peak-to-peak and 50 nm pitch height from groove to ridge. Each data point represents the wavelength location of the upper or lower coupling dip in the reflection measurement at different incidence angles.

Laser Characterization. A 446 nm blue diode laser is used as the photothermal heating source. The laser was routed through an optical microscope optical path using a 40x objective lens system. The power densities delivered to the substrate are of the same order for the 40x and 100x objective systems, as seen in the table below. Specifically, the power density of the laser when using the 40x objective lens was ~ 4.71 x 10^5 W/cm^2, while the FWHM laser profile is 1.46 μm x 0.545 μm.

Table 3-2. 446 nm blue laser characterization.

446nm Blue Laser Characterization		Microscope Objective Lens	
Measured		40x	100x
Source Power	mW	1600	1600
Max Power Delivered (*Pmax)*	mW	102	50
Running voltage	V	5.6	5.6
Pulse Time	µs	7	7
Power at 7 µs *~7.5% x Pmax*	mW	7.642	3.75
Laser Area FWHM (PEAK)	μm^2	1.82 (0.81)	0.796 (0.275)
Power Density FWHM (PEAK)	W/cm^2	4.20×10^5 (9.55×10^5)	4.71×10^5 (13.6×10^5)

Sample preparation. Thin α-MoO3 flakes were synthesized using the ambient pressure physical vapor deposition method [110]. A 500 nm thick Mo film deposited on a Si wafer by DC sputtering was heated to 540 °C for 10 min in air. A freshly cleaved Mica sheet was then placed in contact with the top of the Mo surface. During heating, Mo oxidized, and thin layers of α-MoO_3 were deposited on the mica surface. The flakes were adhered to the mica by van der Waals forces. A polydimethylsiloxane (PDMS) stamp was pressed to the mica sheet and placed in DI water to separate PDMS from the mica sheet to transfer the α-MoO_3 flakes to the desired substrate.

Next, Al particles with a nominal average diameter of 50 nm, 80 nm, 120 nm, and 3-4.5 µm are separately prepared with 0.1 mg/mL concentration in ethanol. The sample was ultrasonicated in a sonic bath for 2 hours, and each freshly drop-casted sample was immediately tested in the laser experiment.

Experiment Strategy. 2 µL of each Al particle solution was drop cast onto the sample in pre-determined areas, and then the following steps were performed:

1. Take high resolution 100x air imaging in brightfield and scattering mode with the Infinity Camera.
2. Using 100x objective lens, perform photothermal heating experiment at 5.6 V max power (1-μs Arduino input yields a 7-μs actual rise time laser output, as discussed in the previous Chapter II) using 446 nm blue laser.
3. Other laser wavelengths (638 nm red and 808 nm IR lasers) are later used as a photothermal heating source. However, these lasers can only be operated at a less power than the blue laser. A 7-μs laser pulse using 638 nm red and 808 nm IR lasers did not observe any reaction. Therefore, these lasers are used with a longer pulse duration, e.g., for 100-μs pulse during the following experiment.
4. Take 100x air imaging in brightfield and scattering mode with the Infinity Camera after heating.

After all experimental datasets are obtained and analyzed, visual observations based on optical images will inform the areas/clusters for further investigations in SEM. It is worth noting that before the laser experiment, the unreacted particles were not imaged in SEM to prevent carbon deposition from the SEM vacuum chamber. Any sample contamination can change the particle behavior under photothermal heating and potentially alter the mechanism.

Target Particle of Interest. Figure 3-2 summarizes the SEM images evaluating the fresh unreacted nano-Al and micron-Al particle morphology on a bare grating substrate or a MoO_3 flake. Several things are worth mentioning here for the unreacted areas. **Figure 3-2(a)** shows SEM imagery at a magnification of 80,000x, resolving individual silver grains in the size of tens of nanometers which is in line with an atomic

force microscopy measurement in the previous report [68]. The image shows the pristine sample areas throughout the grating substrate with no pre-existing debris, defects, or junks.

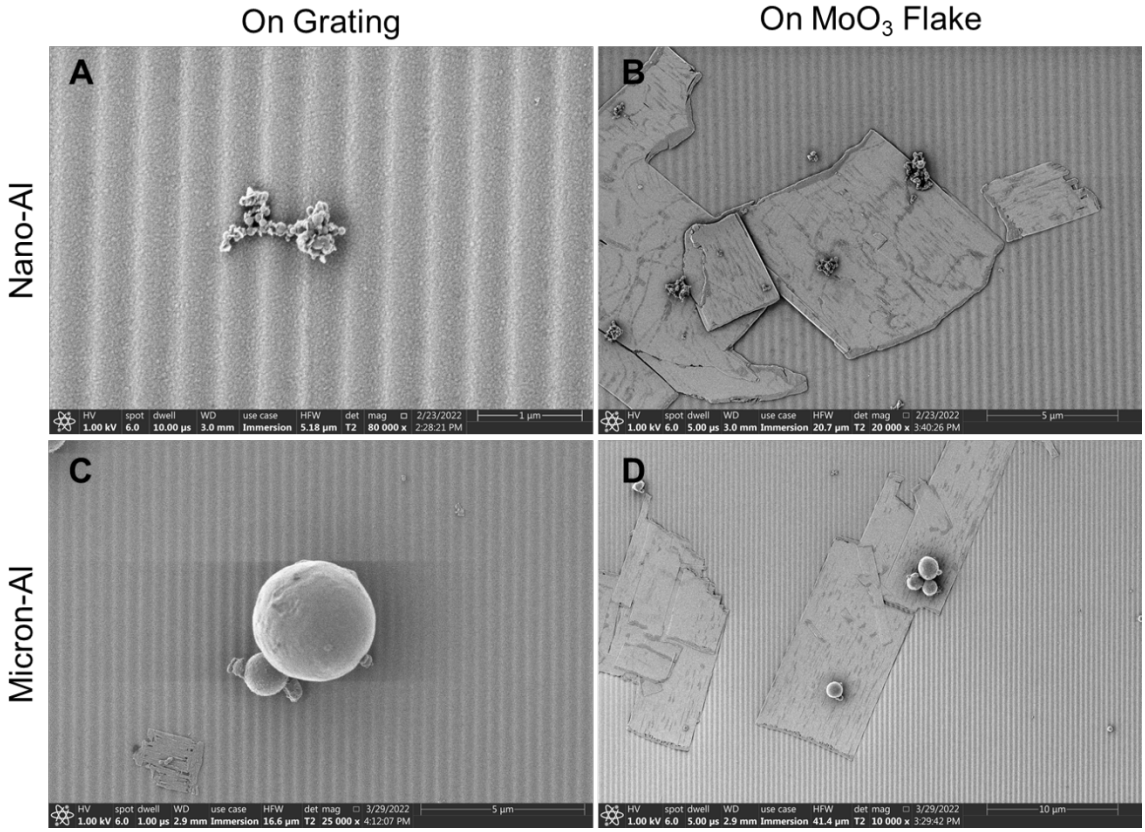

Figure 3-2. SEM images reveal the morphology of the (a-b) nano-Al and (c-d) micron-Al particles on the grating substrate and MoO3 flake, respectively.

3.3 COMSOL Simulation

COMSOL Multiphysics with the RF module is used to simulate the electromagnetic absorption by a particle, based on Mie theory. The particle is embedded in a non-absorbing medium of the relative dielectric function ε_2 and excited at a wavelength λ by an incident field $\mathbf{E}(\mathbf{r})$ consisting of a plane wave of amplitude E_0 traveling along the z-axis and polarized along the x-axis. The incident electric field can be described as:

$$E_x = E_0 e^{-j2\pi/\lambda_0 z}[V/m] \tag{3.1}$$

where λ_0 is the wavelength in free space that corresponds to the laser wavelength, and E_0 is the input electric field related to laser intensity used for photothermal heating. To investigate the excitation wavelength for optimum photothermal heating, the ability of a matter to absorb a photon of a particular wavelength can be quantified by the absorption cross-section, $\boldsymbol{\sigma_{abs}}$ defined as

$$\sigma_{abs} = \frac{W_{abs}}{S_0} \tag{3.2}$$

where $W_{abs}$is the absorption energy [W] and S_0 is the incident radiation [W/m^2].

In COMSOL, the absorption cross section is calculated from the volume integral of the total power dissipation density inside the nanoparticle, as follows:

$$\sigma_{abs} = \frac{1}{S_0} \iiint_{NP} Q_h \, dV \tag{3.3}$$

where $Q_h = \frac{1}{S_0}\omega\varepsilon_0 \mathrm{Im}((\varepsilon_2(\omega))|\mathbf{E}(\mathbf{r})|^2$ is the total power dissipation density, $\varepsilon_2(\omega)$ denotes the relative dielectric function of the particle (possibly in a complex form and wavelength-dependent), and $S_0 = \frac{{E_0}^2}{2Z_1}$ is the power density of the incident field. Whereas $Z_1 = Z_0/\sqrt{\varepsilon_1}$ and $Z_0 = \mu_0 c = \approx 376.73\Omega$ is the characteristic impedance of vacuum. Since we are also interested in mapping the electric field enhancement, the incident electric field, E_0, is adjusted based on the obtained power density from the experiment parameter. Therefore, we define the following parameters

```
Z1 = Z0_const / sqrt(epsilon1)
S0 = E0^2 / (2*Z1)
```

Once the model is simulated for the defined parameters, e.g., geometry, materials, and wavelength of excitation, the absorption cross section can be called using the function below:

```
sigma_abs = intop_vol (emw.Qh)/S0
```

where emw.Qh is the Q_h, the total power dissipation density as explained previously, intop_vol is the volumetric integral of the particle, and S0 is the power density of the incident field. Further, the absorption efficiency Q [dimensionless] can be obtained by dividing the absorption cross section by the geometrical size of the nanoparticle (physical cross section area, $A = \pi r^2$). The absorption efficiency is the proportionality constant between σ and A, which follows the relationship of $\sigma_{abs} = QA$.

Figure 3-3 represents various particle sizes' spectral absorption cross section and spectral absorption efficiency. The individual nanoparticle of 50, 80, 120, or 150 nm diameters was simulated with a 3 nm alumina shell. The baseline spectral absorption of an Al NP surrounded by air was first evaluated and was represented in **Figure 3-3(a, c).** The absorption peak at 810 nm is the intrinsic peak of aluminum dielectric loss, while the absorption peaks at the lower wavelength region represent the plasmonic peaks. In **Figure 3-3(a)**, several plasmonic peaks are visible; for instance, the dipole peak is at around 520 nm for Al NP 150 nm (red line). The dipole peak blue-shifts and narrows as the nanoparticle size decreases. Since all nanoparticles have the same alumina shell thickness, smaller particle size results in higher absorption efficiency at LSPR peaks due to a better electric field confinement effect per geometrical area.

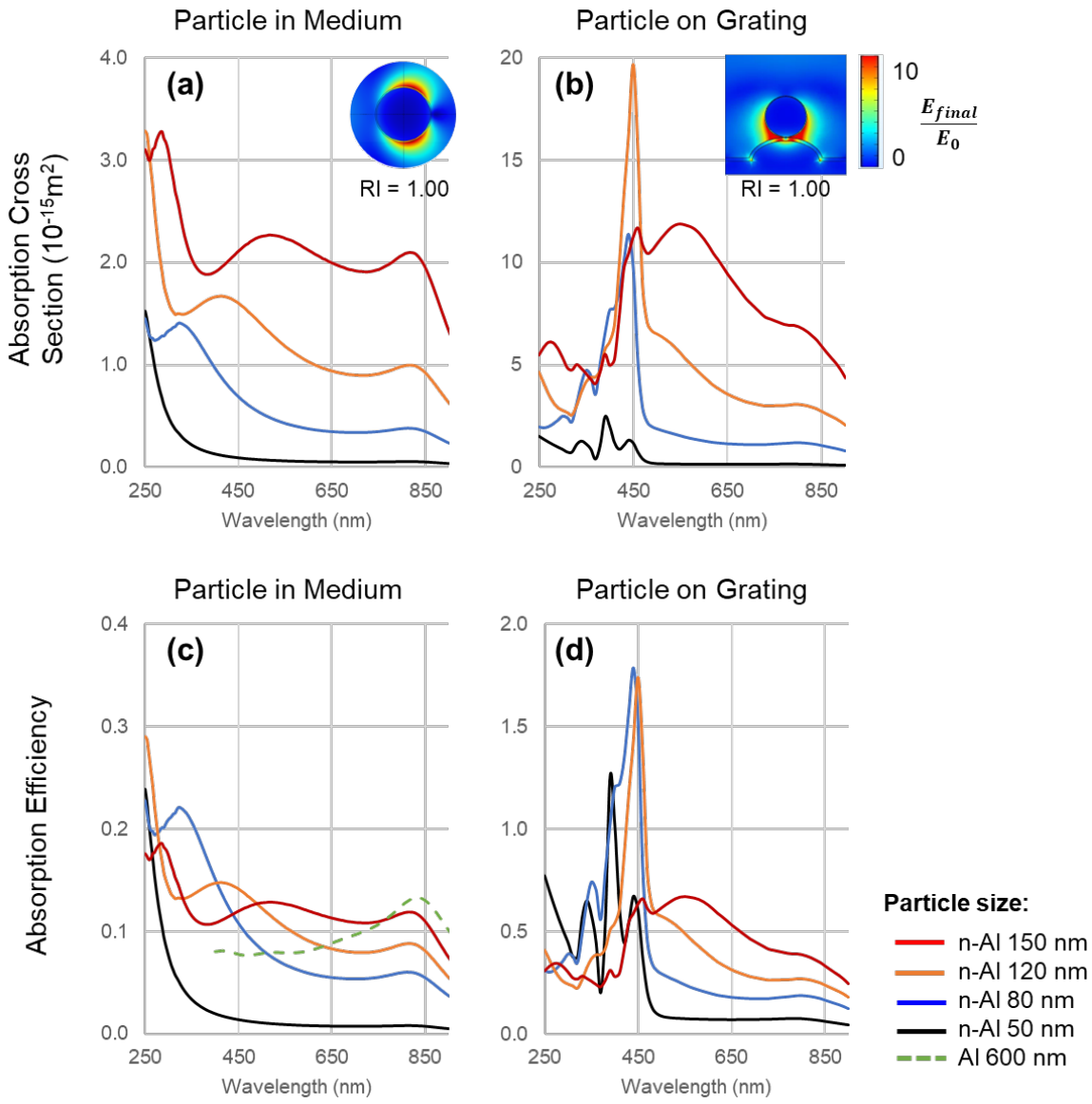

Figure 3-3. COMSOL simulation of (a-b) absorption cross section and (c-d) absorption efficiency in air medium for a single Al NP suspended in medium and residing on a grating, respectively.

Additionally, the absorption efficiency of Al micron particles is in the same order as their nano-sized counterparts, as indicated by the green dotted line in **Figure 3-3©**. the simulation was not able to calculate the lower wavelength (250-400 nm) because of the solution was not converging at these wavelength values. A different mesh or geometry model might be needed to simulate the Al micron particles to resolve the

absorption efficiency at this wavelength region. As a side note, the electric field distribution map can be generated by calling the emw.normE function in the COMSOL post-processing outcome. Then, to normalize the resulting electric field, the formula is emw.normE/E0, denoted as E_{final}/E_0 in the insets of **Figure 3-3(a-b)**.

The same Al NP dimensions, 50, 80, 120, or 150 nm, were then simulated while resting on the ridge of a plasmonic grating substrate to determine the electric field enhancement, as shown in **Figure 3-3(b, d)**. A horizontal span of three grating pitches was modeled to reduce the computational workload, while the scattering boundary condition was applied so that no inward waves were entering the domain. The electric field source was a periodic port placed 1.2 μm above the grating at a 0° incident angle, normal to the substrate. The electric field source is represented as uniform intensity with a peak power density of 4.2×10^5 W/cm^2 as used in the actual experiment. Properly selecting the laser wavelength can enhance coupling between the nanoparticle to the grating. For example, at around 450 nm, the coupled electromagnetic field interaction enhanced the energy absorption by 8-18 times relative to an Al NP in the open air. Therefore, selecting a blue laser 446 nm can enhance coupling Al NP and grating substrate for photothermal ignition application.

Once the electromagnetic response is obtained, COMSOL then simulates particle heating, where the photoexcitation of material by electromagnetic radiation results in thermal energy or heat production. The COMSOL Heat Transfer module accounts for the material properties to accurately simulate the thermal response of photothermally heated Al NP. Detailed derivations of the model were previously discussed in **Chapter I**. After the electromagnetic and thermal responses are simulated, the particle's

temperature can be obtained and presented as a function of time, as shown in **Figure 3-4**.

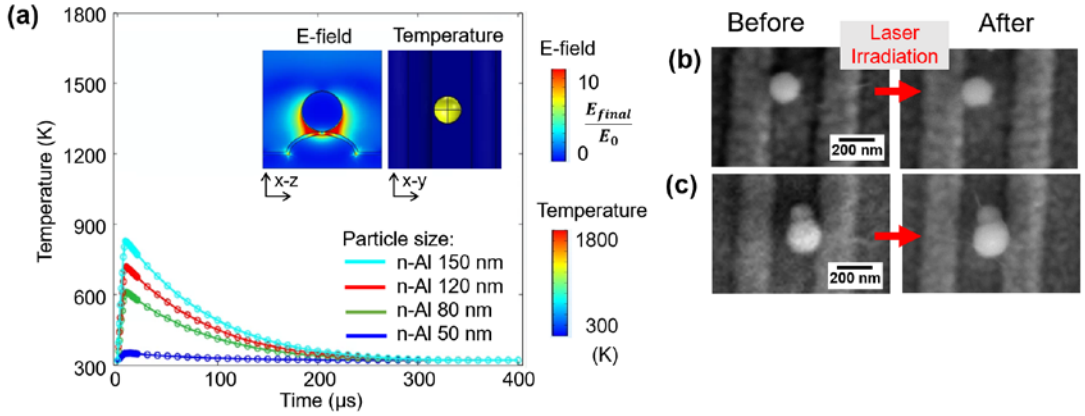

Figure 3-4. (a) COMSOL simulation generates the thermal transient response of a laser-heated single Al NP with various particle diameters. The simulation is performed using a 446 nm blue laser with a 7-μs pulse on Al NP residing on a grating ridge in an air medium. Experimental results indicate no effect after laser irradiation upon (b) a single Al NP and (c) two Al NPs residing on the grating substrate.

Figure 3-4(a) summarizes the simulation of a 7-μs blue laser irradiating a single Al NP with different diameters: 50, 80, 120, and 150 nm, on a grating substrate and an air medium. The insets also provide maps of the electric field and temperature distribution at their respective cross-sectional views. The electric field map is normalized and denoted as E_{final}/E_0 to observe the intense coupling between the particle and grating. The temperature of an individual Al NP was recorded over time. The temperature rises for 7 μs which follows the intrinsic rise time of the diode laser, then exponentially decreases for around 200 μs. Note that in this simulation, all Al NPs reside within the region of maximum laser intensity. The simulated peak temperature for all particles can be observed. Among them, the 150 nm Al NP reaches the highest temperature of ~850 K, which is still lower than the melting temperature of aluminum at 934 K. This temperature simulation can be a crucial insight into experimental

observations in which a 7-μs laser pulse provided no effect when irradiating a single Al NP or two Al NPs. As shown in **Figure 3-4**, the temperature rise was roughly about 300-500 K in a 7-μs duration, which gives a heating rate of ~4.3-7.1 × 10^7 K/s. Although the rapid heating rate of greater than 10^7 K/s, the temperature of >1100K required was not achieved for observing spallation as previously shown in **Figure 1-4**. For less than two Al NPs, we have yet to observe any reaction or spallation using any medium or laser configuration, as shown in **Figure 3-4(b-c)**. This reason directs us to employ at least a cluster of 4 Al NPs for the simulation and experiment. Next, a cluster of 4 Al NPs is simulated with the adopted configuration from an experiment in **Chapter 2**. The transient temperature for each particle within the cluster configuration is shown in **Figure 3-5**. For the particle assembly in **Figure 3-5**, all particles reach between 1,000 – 1,500 K within the duration of the laser rise time of 7 μs, generating a heating rate of ~1-2 × 10^8 K/s. The fast-heating rate can be attributed to electric field enhancement of the plasmonic grating and heat accumulation of multiple nanoparticles acting as heat sources.

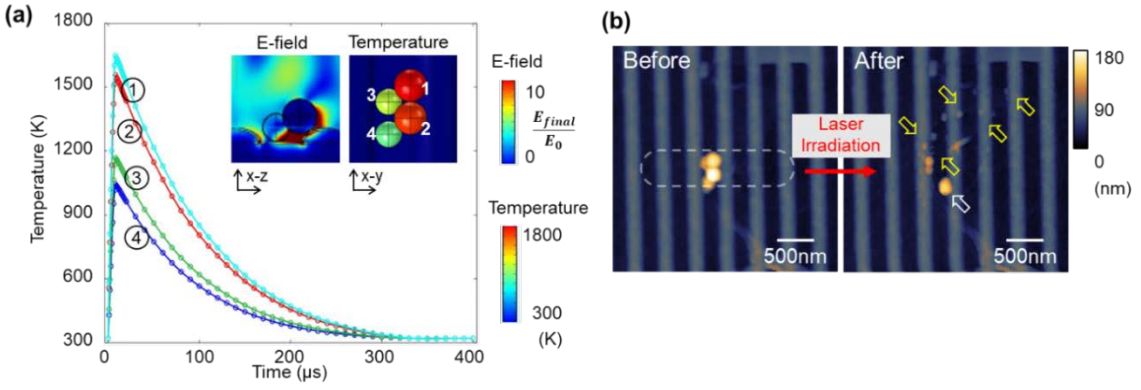

Figure 3-5. (a) COMSOL simulation generates the thermal transient response of a laser-heated 4-Al-NPs cluster. The laser heating profile of a 4-Al-NPs cluster (cluster's arrangement is depicted in the inset) is simulated to obtain the generated temperature as a function of time. The simulation is performed using a 446 nm blue laser with a 7-μs pulse on Al NP residing on a grating ridge in an air medium. Experimental results indicate spallation after laser irradiation

upon (b) a cluster of four Al NPs residing on the grating substrate, as discussed in the previous chapter.

Compared to a few NPs clusters, the larger cluster may lead to a higher heating rate due to a greater plasmonic coupling and total absorbed energy. Ohkura et al. estimated the temperature increase initiated by a light-induced heat source. The theoretical and experimental observation concludes that sparsely distributed Al NPs could not be ignited under flash heating [55]. Previously, we reported that single Al NP residing on the grating platform could not achieve a high enough temperature to initiate any ignition by laser-induced heating [138]. A higher temperature rise rate has also been found for larger packing densities of Al NPs clusters in that more heat per unit volume is absorbed [50]. These findings further support the importance of incorporating larger clusters to achieve a high heating rate. As a result, the following sections only consider laser heating experiments for clusters with four particles or more.

3.4 Aluminum Particles Reaction on Grating Substrate

Photothermal laser heating experiments were conducted on Al particle clusters, approximately 30-50 particles in each cluster. Various particle sizes were studied, and among them are 50 nm, 80 nm, and 120 nm Al NPs. In this experiment, the color camera, in brightfield and scattering modes, captured the image before and after the 7-μs laser irradiation. After the experiment was conducted, high-resolution SEM images were taken to reveal the post-mortem morphology of reacted clusters.

After single 7-μs laser irradiation, the target nano-Al particles cluster on the flat silver substrate only experienced melting and sintered into a lump, as shown in **Figure 3-6** and **Figure 3-7(a)**. Melted and sintered particles from the reaction are usually

associated with a low heating rate of $<10^5$ K/s or a mild oxidation event [47,139]. The result underlines that the actual fluence generated by the laser power density and exposure time was insufficient to cause spallation events.

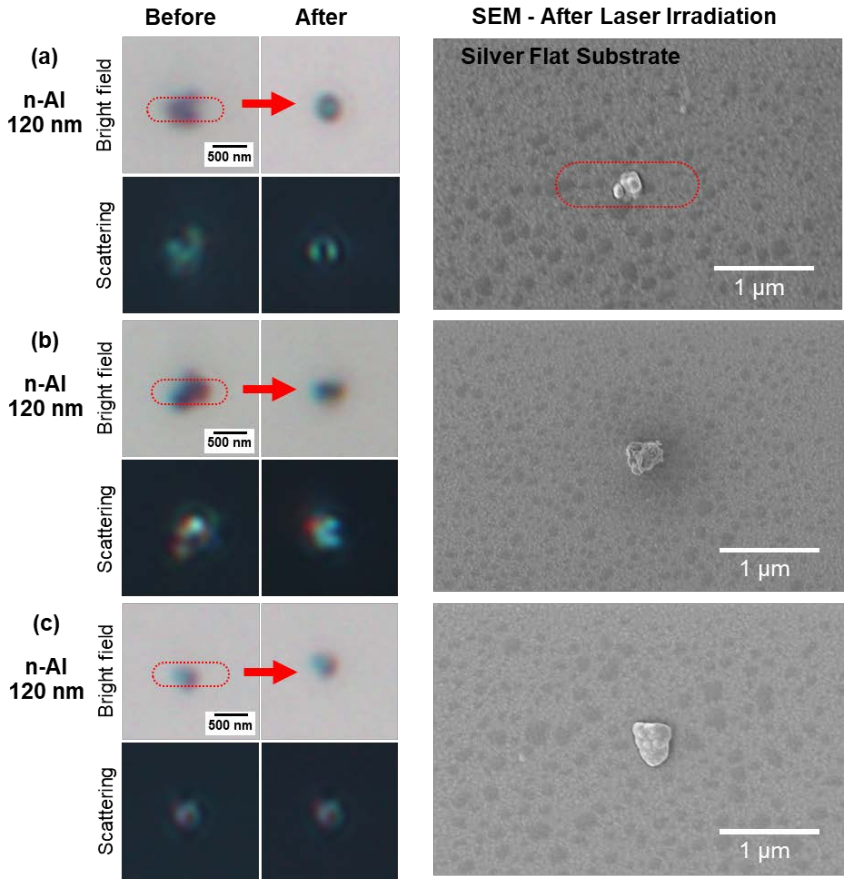

Figure 3-6. Partial sintering and melting were observed for a cluster of 120-nm nano-Al particles on flat substrate after single 7-µs 446 nm blue laser irradiation. No spallation was observed. Optical microscope images (presented in true colors) captured the sample morphology before and after laser irradiation, while SEM reveals the high-resolution post-reaction imagery.

The importance of plasmonic grating in the experiment is well summarized in **Figure 3-7** when compared to a flat silver substrate. All nano-Al particle clusters (50 nm, 80 nm, and 120 nm) reside on grating substrate nanofragment spallation, as shown in **Figure 3-7(b-d)**. According to MDM theory, the observation of spallation events can only occur at a heating rate of $>10^6$ K/s. Moreover, an enhanced

electromagnetic field can be coupled by adequately selecting the particle or cluster's medium and optical absorption of laser wavelength. This finding argues that enhanced fluence from the plasmonic grating substrate can provide an increased heating rate.

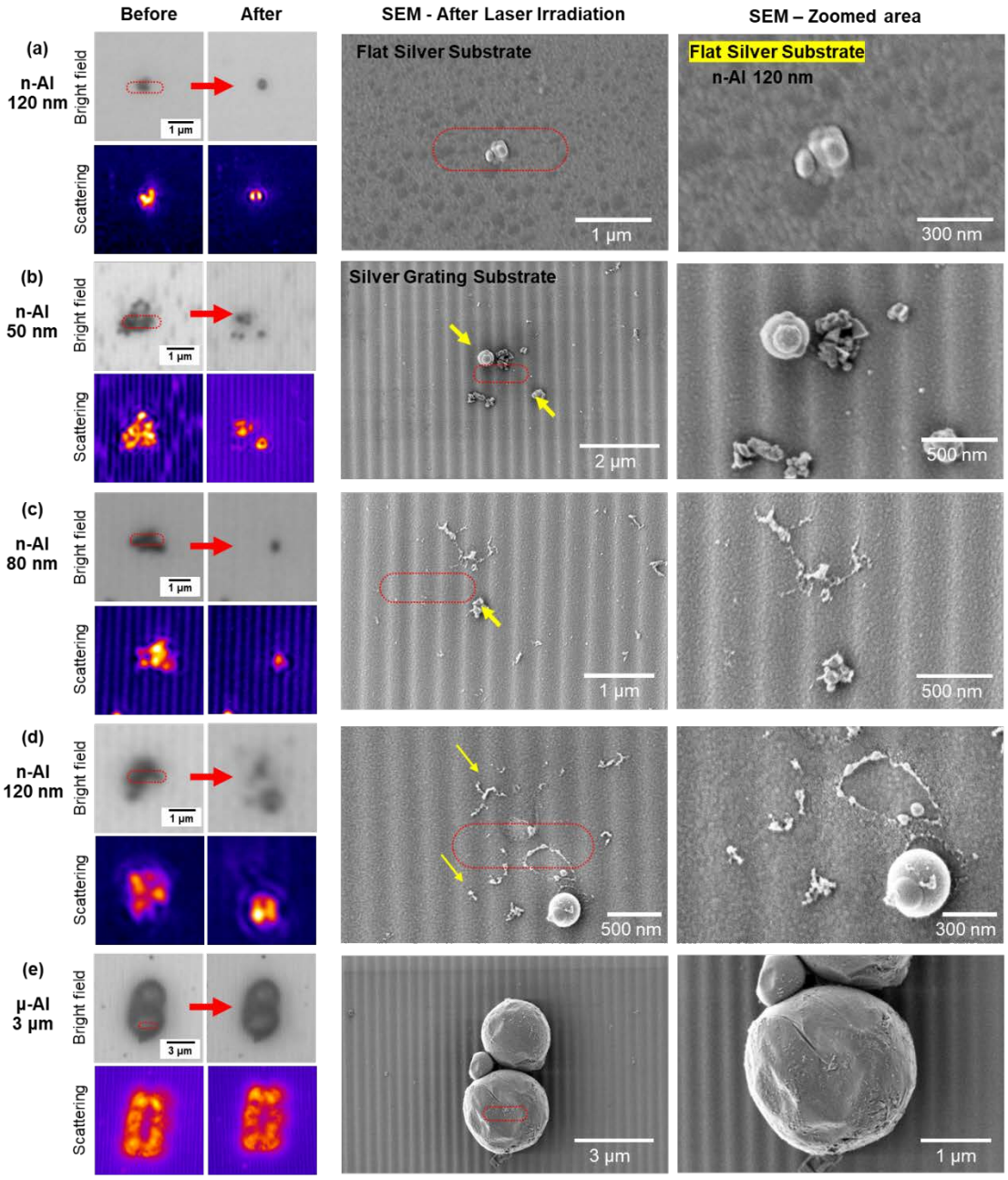

Figure 3-7. Spallation of Al NPs cluster was only observed on nanoparticles residing on grating substrate after single 7-µs 446 nm blue laser irradiation. No spallation was observed for Al NPs on flat substrate, neither was for micron Al on grating substrate. Optical microscope images (presented in false color) captured the sample morphology before and after laser

irradiation, while SEM reveals the high-resolution post-reaction imagery. The different data sets are (a) 120-nm nano-Al particles on a flat silver substrate, (b) 50 nm, (c) 80 nm, (d) 120 nm nano-Al, and (e) 3 μm micron-Al particles on the silver grating substrate.

Figure 3-7(b-d), the bright field image indicates that some nano-Al particles reside outside the laser area before the laser illumination. The post-reaction SEM characterization shows that the particles outside the laser area are either unreacted or sintered into a larger lump, as pointed by yellow arrows in **Figure 3-7(b-d)**. As a result, particles residing outside the laser did not experience spallation as the maximum temperature and the minimum heating rate was not achieved to generate enough Al core pressure and tensile stress at the alumina shell. Instead of spallation into nanofragments, these particles may experience thermally-induced sintering at elevated temperatures and form a sintered lump [53]. The temperature to achieve sintering can be from the laser's low power density outside the perimeter of the dotted region and the heat transfer from the neighboring spalled particles.

In such an experimental setup where local photothermal heating initiates only the target cluster by a focused laser, the location of Al particle clusters in respect to the laser alignment is crucial to observe spallation. **Figure 3-7** indicates the full-width half-maximum laser spot size marked by the red dotted line. Spallation only occurred for the nano-Al particle entirely within the full-width half-maximum (FWHM) profile of the laser, which was revealed in the optical and SEM images. This area has the highest laser fluence and will yield high heating rates sufficient for MDM. The ejecta is well dispersed radially several micrometers away from the initial reaction site. It is worth noting that the ejecta can easily be distinguished from the silver grains of the plasmonic grating substrate, as pointed by yellow arrows in **Figure 3-7**. The distinct feature of the ejecta allows visual observation and tracking of the traveled distance

the dispersal was spalled. The spallation event observed in this experiment contradicts the diffusion oxidation and reactive sintering mechanism where the product has increased in size during the reaction [53,140,141].

Here, COMSOL simulation can compare the estimated heating rates between different particle sizes and substrates. Besides the particle sizes or different substrates, all model parameters are kept constant, including the laser source and particle arrangement. First, the transient temperature response of three Al NP sizes is shown in **Figure 3-8(a-c)**. A cluster of 4 Al NPs was selected and simulated for the simplicity of comparing different nanoparticle dimensions. Because of the low absorption cross section, the 50-nm Al NPs cluster generates a low-temperature response of around 700 K, below aluminum's melting point. Though, the 50-nm Al NPs cluster indicated spallation in the experiment shown in **Figure 3-7(b)**. While the simulation only accounted for one particle, the actual experiment was conducted on a cluster of Al NPs. Therefore, spallation may be observed because of the large number of particles. Further, transient temperature simulation of 80-nm and 120-nm Al NPs clusters indicates that the particle can reach up to 1650 K within the 7-μs laser rise time **Figure 3-8(b-c)**. Hence, the estimated heating rate ($\boldsymbol{\partial T/\partial t}$**)** is 1.7 x 10^8 K/s for 120-nm Al NPs residing on silver grating substrate. This high heating rate of beyond 10^8 K/s may well satisfy the requirement of MDM.

Second, the transient temperature response of Al NPs residing on flat silver and silver grating substrates is shown in **Figure 3-8(a-c)**. While the estimated heating rates for 120-nm Al NPs residing on the silver grating substrate is 1.7 x 10^8K/s, the cluster on a flat silver substrate only reached a heating rate of 4.2 x 10^7 K/s. This is calculated from the peak temperature of ~600 K within the 7-μs laser rise time, as shown in

Figure 3-8(d). Although the heating rate is in the order of 10^7 K/s, the low peak temperature is the reason why Al NPs clusters residing on a flat silver did not satisfy the MDM requirement.

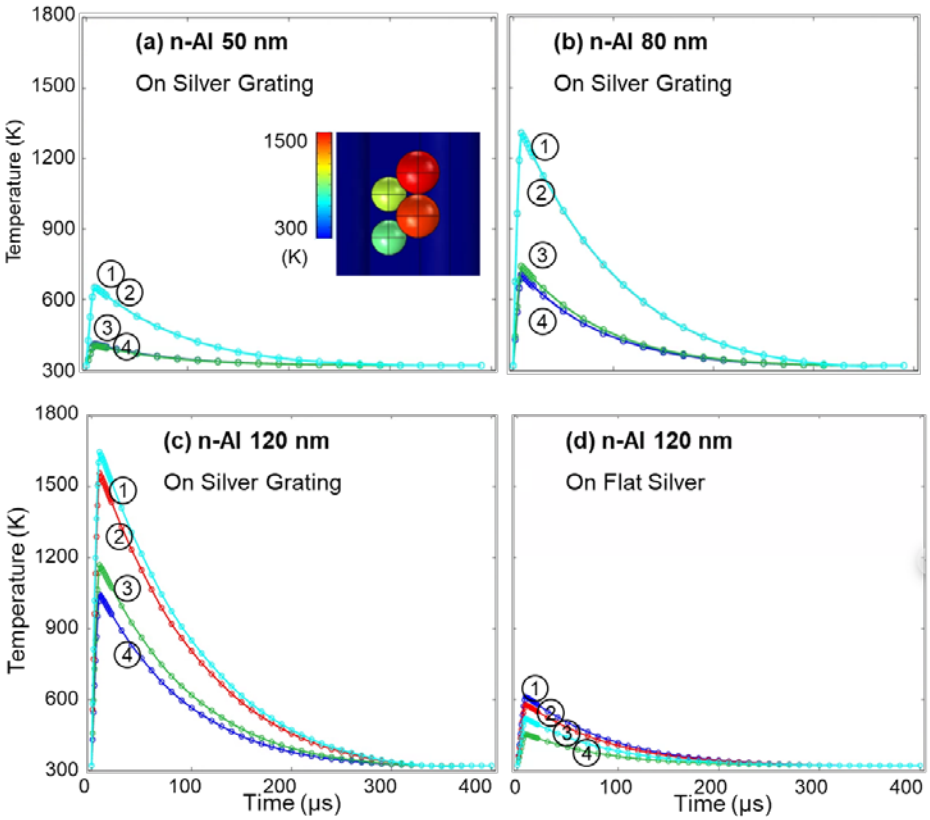

Figure 3-8. The laser heating profile of a 4-Al-NPs cluster (cluster's arrangement is depicted in the inset) is simulated to obtain the generated temperature as a function of time. The simulation is conducted on different particle sizes and substrates, including (a) 50 nm, (b) 80 nm, and (c) 120 nm Al NPs on a silver grating substrate, and (d) 120-nm Al NPs on a flat silver substrate.

This observation of Al NPs spallation is consistent with our previous work (**CHAPTER 2**). Hot molten Al, ejected during the spallation event, can react to the surrounding oxidizing agent available in the air. At the same time, the previous work incorporated the underlying graphene sheet, while in this work, the ejecta lands on the silver grating substrate after oxidizing in the gas phase. One significant difference between the two experiments is the unique shape of the ejecta. It could be assumed

that the parts of the spallation ejecta may evaporate. COMSOL simulation indicates that the temperature can reach beyond the aluminum melting point. Even when the ejecta is presently at a high temperature, few neighboring ejecta could not coalesce during the cooling-off event because the substrate acts as a heat sink. The ejecta's state may cool off or condense through homogeneous nucleation [142]. As seen in **Figure 3-7**, the ejected nanofragments have irregular shapes compared to the spherical ejecta spalled onto graphene observed in our previous work (**CHAPTER 2**).

Nanofragment spallation was not observed on micron-Al particles heated by laser irradiation. However, the high-resolution SEM imagery shows some dents on micron-Al particles after laser irradiation, as seen in **Figure 3-7(e)** and **Figure 3-9**. Insufficient photothermal heating cannot initiate the compressive pressure within the Al core and develop high tensile stress in the alumina shell. Due to the relatively elevated temperature in a short time, the shell may experience plastic relaxation during this heating event instead of fracture [49].

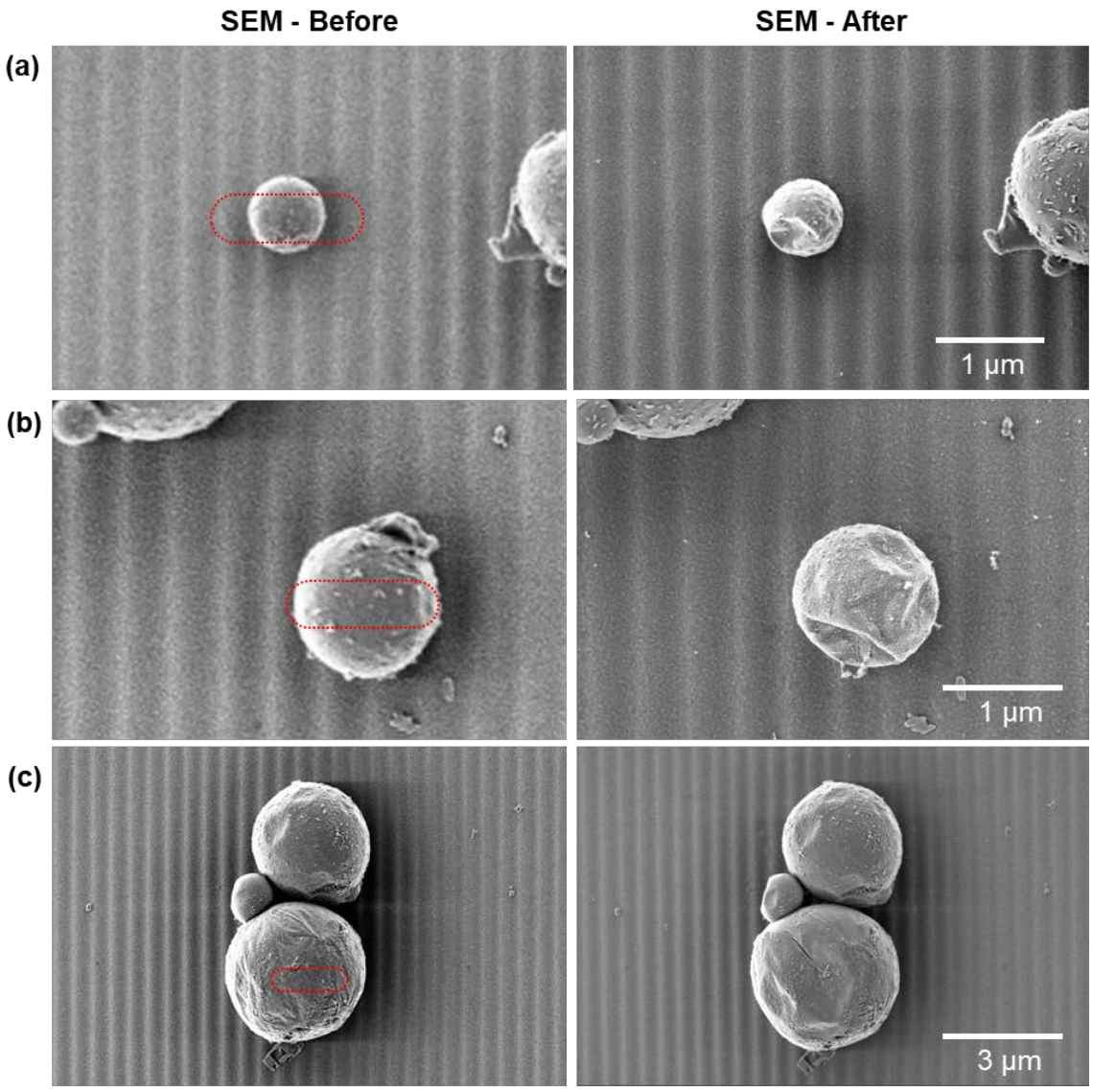

Figure 3-9. SEM reveals the high-resolution imagery of micron-Al particles on the silver grating substrate, before and after single 7-μs 446 nm blue laser irradiation.

3.5 Graphene-Isolated Aluminum Particles Reaction in Oil Medium

In this work, we observe the reaction of isolated 120-nm Al NPs clusters using localized photothermal heating. All experiments were conducted on an optical grating to enhance the photothermal heating effect and the optical imaging of the Al NPs. To isolate the NPs from atmospheric oxygen, single-layer graphene sheets were positioned on the surface of the underlying grating substrate and atop the Al NPs. The

graphene sheets conformed well to the grating surface and Al NPs, as demonstrated by atomic force microscope (AFM, Innova Bruker) and scanning electron microscope (SEM, FEI Scios) images. Similar to our experiment setup described previously [50,138], a diode laser, focused by the optical microscope objective, supplied targeted photothermal heating.

The effect of different medium and laser wavelengths will be studied in this section. Unlike the previous section, which uses an objective lens for air medium, this section will incorporate the 100x oil objective for laser focusing and imaging. The following experiments use different laser wavelengths blue 446 nm, red 638 nm, and IR 808 nm. **Figure 3-10** represents the absorption efficiency simulation of a single 120-nm Al NP in air and oil medium. The individual nanoparticle has a diameter of 120 nm with a 3 nm alumina shell. The baseline spectral absorption of an Al NP surrounded by air was first evaluated in **Figure 3-10(a)** before evaluating Al NP residing on the grating substrate, as shown in **Figure 3-10(b)**. The blue laser is highly coupled in an air medium and shows an 8-10 enhancement factor from the coupling of the 120 nm Al particle to the grating substrate. In comparison, the red and IR lasers show 2-3 enhancement factors from the coupling of the 120 nm Al particle, the grating, and the oil medium.

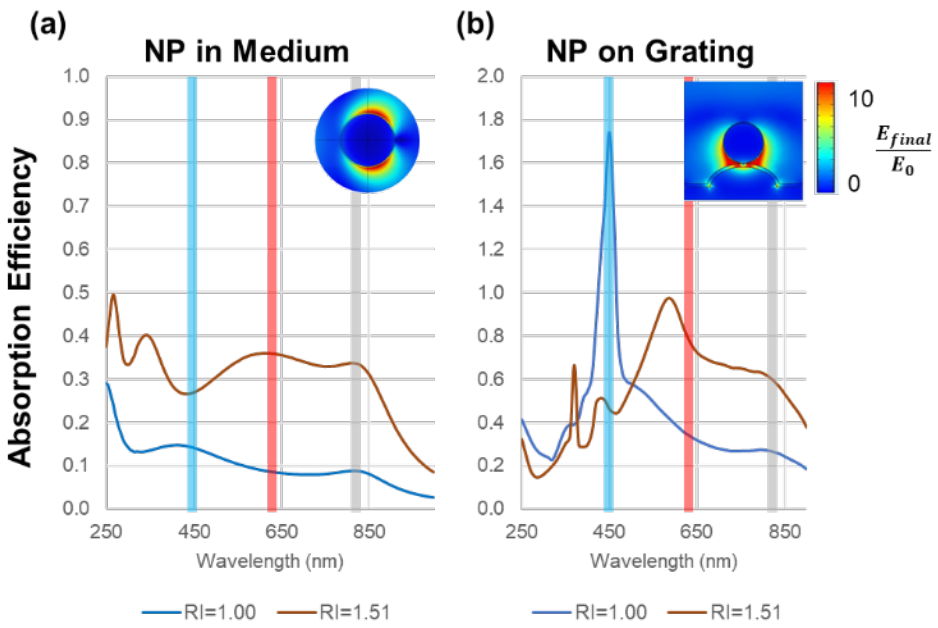

Figure 3-10. COMSOL simulation of absorption efficiency in the air (blue curve) and oil (brown curve) medium for a single Al NP (a) suspended in medium and (b) residing on a grating, respectively. The vertical lines indicate the three different laser wavelengths used in this experiment: blue 446 nm, red 638 nm, and IR 808 nm.

Evidence of Al diffusion or escape is shown in **Figure 3-11 (a-b)**. A cluster of several Al NPs was irradiated to observe Al melting by a long 1-ms laser pulse with a peak power density of 0.9×10^5 W/cm^2. As shown in **Figure 3-12(a)**, the simulation indicates that the 1-ms low power blue laser can reach a temperature of around 1,000 K over the entire laser pulse duration. When the absorbed energy can rise to the Al melting temperature (1,000 K), the corresponding heating rate is approximately 10^6 K/s. Sufficient absorbed energy allowed Al to escape the heated NPs and form an extended, smooth melt zone that solidified upon cooling. Molten Al leaking out through the fractures may be caused by the polymorphic phase transformation of the oxide shell layer [121,122]. The process is accelerated in areas of the shell that contain pinholes or grain boundaries.

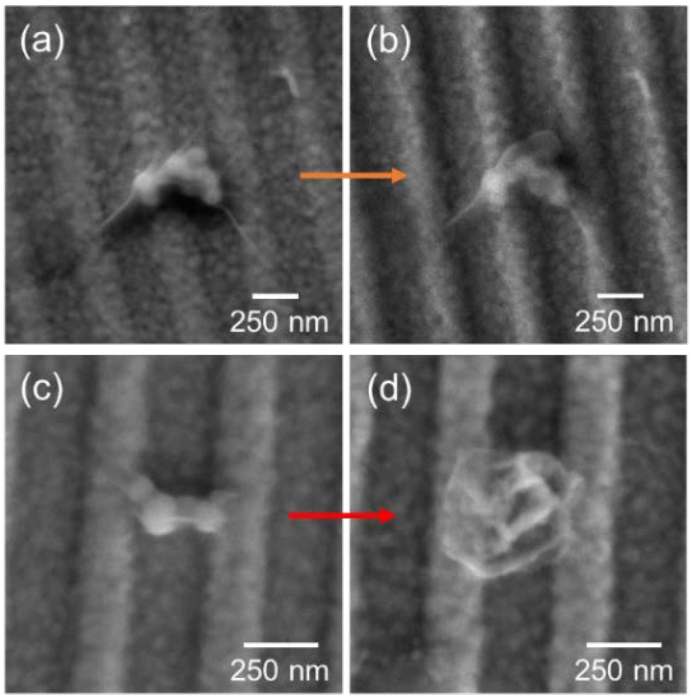

Figure 3-11. High magnification SEM images reveal the morphology of the Al NPs in graphene sheets in an oil medium before and after laser irradiation. (a-b) The low heating rate can be achieved by irradiating a 1-ms low power blue laser pulse. (c-d) A high heating rate can be achieved by irradiating a 7-µs high power blue laser pulse.

In a high heating rate regime, the Al NPs are far from equilibrium, and mechanical effects can break the protective oxide shell and result in spallation of the core. The evidence can be observed in **Figure 3-11(c)** and **Figure 3-11(d)**. A cluster of four Al NPs trapped between two graphene sheets residing on the groove of the plasmonic grating substrate. A single 7-µs blue laser pulse was irradiated to the cluster using a higher power density of 4.2×10^5 W/cm^2. In relatively faster heating, we observed graphene wrinkles expanding more than 100 nm beyond the initial site of the cluster. The altered morphology of the graphene sheets denotes nanoparticle explosion that generated a high pressure or mechanical force. More importantly, the post-ignition figure indicated fragment dispersion as there was no large remnant of the alumina shell. As shown in **Figure 3-12(b)**, the simulation indicates that the 7-µs high power

blue laser can reach a temperature of more than 1,200 K. Considering the laser-induced reaction occurred within the irradiation time, the heating rate can be estimated to be greater than 10^8 K/s. Nanometer-sized fragments as products of photothermally heated Al NPs can be attributed to several causes, including spallation of Al core, shock-induced ejecta, or Al vaporization. The observation leads to the high heating rate's correlation to the reaction products of melted Al droplets reported in MDM theory.

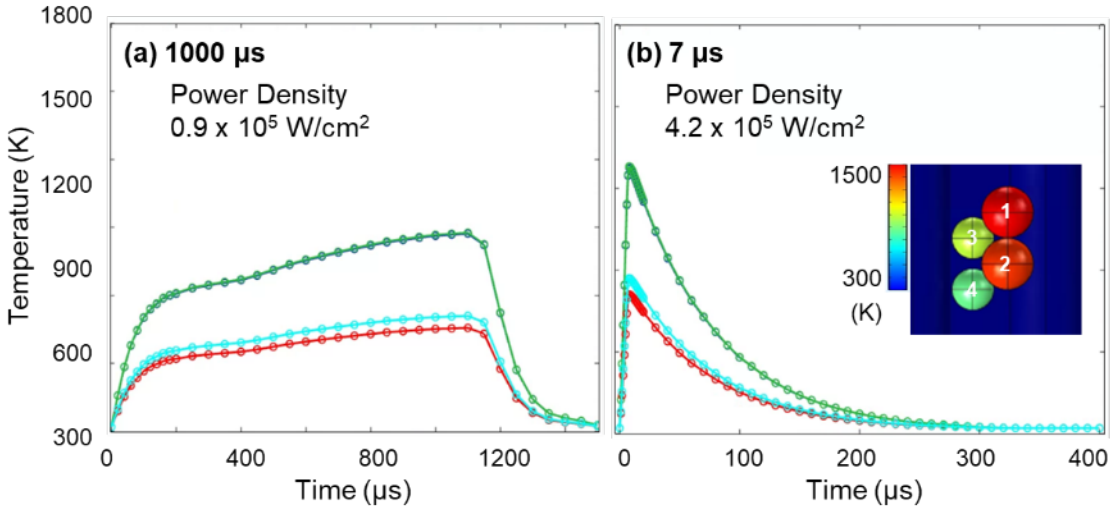

Figure 3-12. Laser heating profiles of a 4-Al-NPs cluster are simulated in COMSOL to obtain the generated temperature as a function of time. The simulation models different pulses and duration: (a) a 1-ms blue laser pulse at a power density of 0.9×10^5 W/cm^2 and (b) a 7-µs blue laser pulse at a power density of 4.2×10^5 W/cm^2.

The discovery in **Figure 3-11(c-d)** was also characterized by optical microscopy. The morphologies of Al NPs trapped in graphene sheets were characterized by brightfield and scattering imaging modes. Brightfield imaging (**Figure 3-13(a)** and **(b)**) was used to locate and align the target NPs cluster at the center of the laser area to deliver the desired power density.

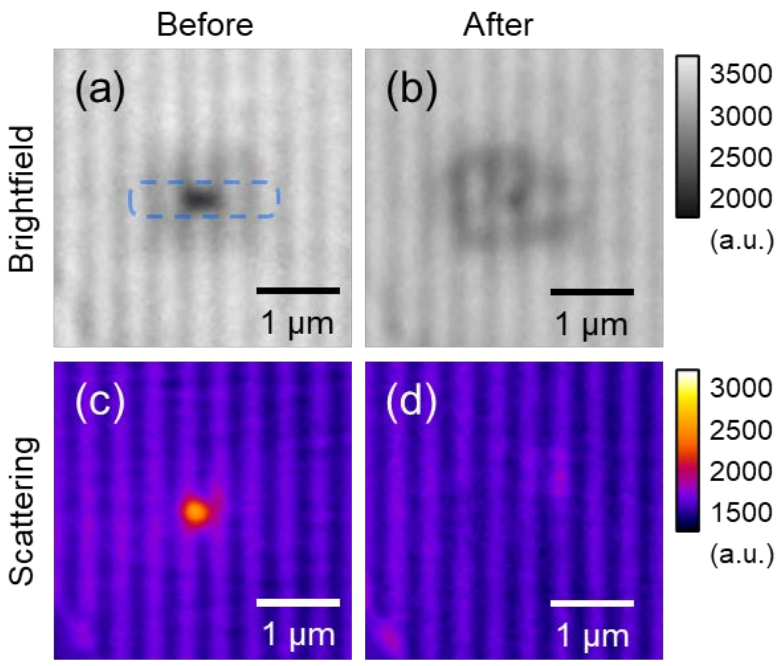

Figure 3-13. Before and after a 7-us laser pulse irradiation, the cluster of Al NPs was imaged using (a-b) brightfield and (c-d) polarization-based scattering modes. (Note: images are false-color with intensity indicated by the intensity bars.)

Scattering imaging can be used to identify the oxidation and morphological reconstruction of the NPs due to laser irradiation. Analyzing scattering intensity change has been utilized extensively for in situ observation of laser-ignited Al NPs [138]. **Figure 3-13(c)** illustrates the high-intensity light scattered by the NPs compared to the low-intensity background of the grating. Scattering mode captured the depolarized light from the metallic content of Al NPs. The backscattered light from the grating was screened out using the polarizer and analyzer at 0° with respect to the grating. **Figure 3-13(d)** indicates a noticeable reduction in scattering intensity after the laser irradiation. As the SEM image revealed in **Figure 3-11(d)** that laser irradiation could cause nanofragment dispersal, it is highly possible that the nanofragments are undetected by the imaging method due to diffraction-limited resolution.

Our previous reports show that scattering mode can identify Al NPs reaction byproducts in the form of aluminum oxide or aluminum fluoride [50,110]. However, graphene also has a role in providing confinement by keeping the Al NPs chemically inert and preventing oxidation from the surrounding air. In the absence of a nearby oxidizer, the reduction in scattering could be caused by the graphene and aluminum reaction. This exothermic reaction leads to the formation of Al_3C_4 starting at around 500 °C [143]. As the metallic content of Al is diminished, the scattering intensity is significantly reduced, and the reaction byproduct appears dark. Additionally, as shown in **Figure 3-14**, scattering images can provide a relatively accurate insight during laser heating experiments.

To study the effect of different laser wavelengths, 638 nm red and 808 nm IR lasers were used to irradiate clusters of Al NPs in the oil medium. The before and after scattering images were used to evaluate the effect of the laser irradiation on the Al NPs cluster isolated between two graphene sheets. It is worth noting that these two lasers only operate in low-power settings. If the lasers are used for 7-µs pulse duration, the maximum power density is around 0.21×10^5 W/cm^2. Hence, the maximum power density can be increased to 8.6×10^5 W/cm^2 by running the laser for 100 µs. In **Figure 3-14(a)**, spallation is observed using a red laser during a 100-µs pulse. Ejected particles trapped in the graphene sheets were observed 2-3 µm away, as observed in the SEM image. A large-sintered lump also indicates particles' coalescence, which often occurs for a large cluster of particles. Additionally, COMSOL simulation shows that the Al NPs cluster irradiated by the red laser can reach a high temperature. The simulation indicates that the 100-µs red laser can heat the Al NPs cluster up to 2,300 K. Hence, considering the laser heating occurred within the 100-µs irradiation time,

the estimated heating rate is ~ $2x10^7$ K/s. The rapid heating rate beyond 10^7 K/s and high temperature rise of >2,000 K are sufficient to satisfy MDM requirement for observing spallation. In contrast, the simulation shows that the 808 nm IR laser with a 100-µs pulse duration, can only heat the Al NPs cluster up to 1,300 K that yields an estimated heating rate of ~ $1x10^7$ K/s. In this case, the spallation was not observed which may be due to insufficient temperature rise. As shown in **Figure 3-14(b)**, SEM images shown the cluster of Al NPs that partially sintered and melted after IR laser irradiation for 100-µs. Both experiment and simulation have shown that the laser wavelength is crucial to determining the reaction mechanism of the photothermally heated Al NPs cluster.

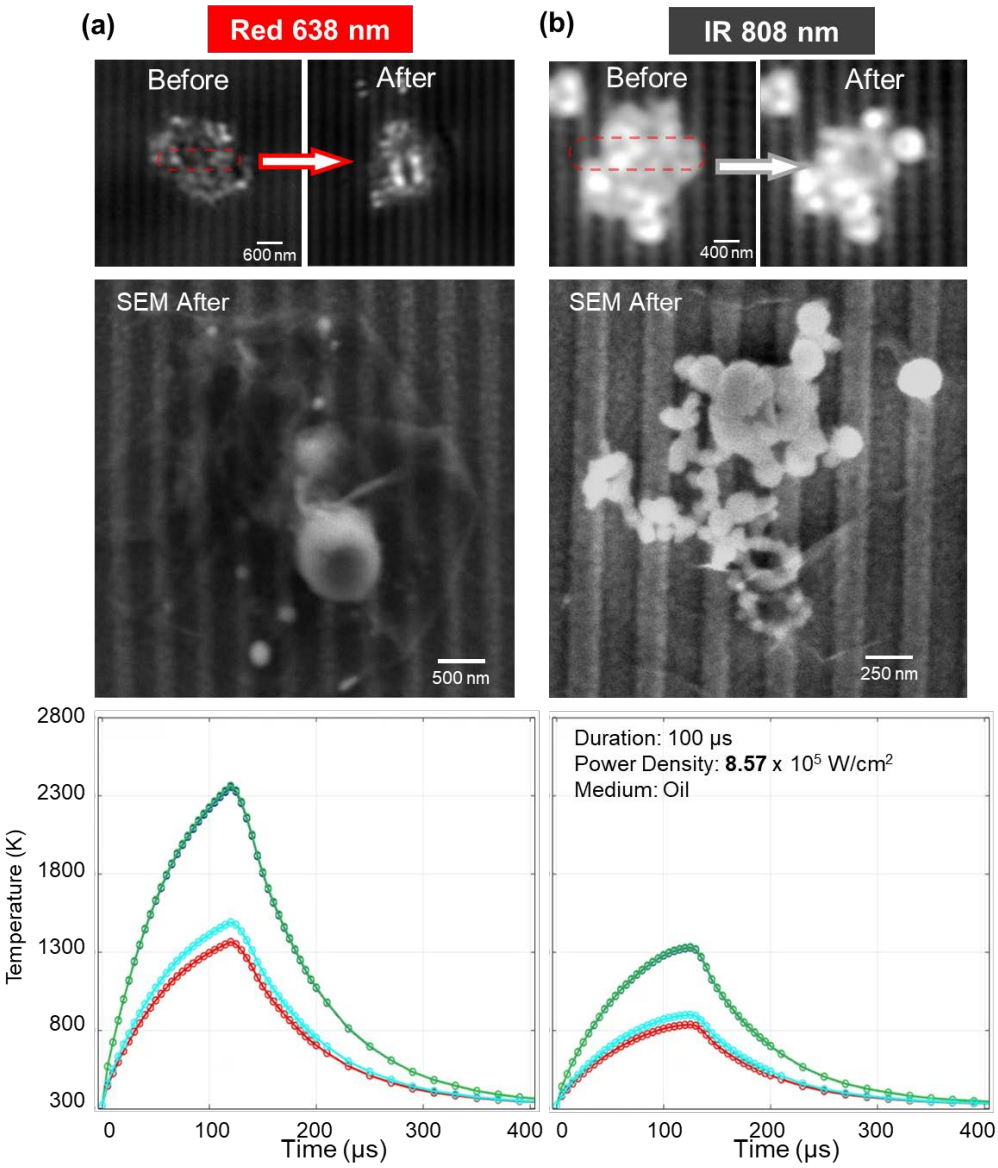

Figure 3-14. Al NPs clusters were irradiated for 100-µs by 638 nm red and 808 nm IR lasers in an oil medium. Scattering images in an optical microscope capture the sample morphology before and after laser irradiation, while SEM reveals the high-resolution post-reaction imagery. Laser heating profiles of a 4-Al-NPs cluster are simulated in COMSOL to obtain the generated temperature as a function of time. The simulation models two different laser wavelengths: 638 nm red and 808 nm IR lasers in an oil medium.

Further, compared to a few NPs clusters, the larger cluster may lead to a higher heating rate due to a greater plasmonic coupling and total absorbed energy. **Figure 3-15(a)** shows an SEM image of ~30 Al NPs cluster trapped in the top and bottom

graphene sheets. The blue dotted line indicates the 446 nm blue laser profile with a full-width half-maximum power density of 4.2×10^5 W/cm^2. **Figure 3-15** displays the ignition product after 7-µs laser irradiation. The reaction events, including the torn graphene sheets marked by the red arrow, show that the graphene layers were removed entirely and wrinkled outward. Defects leading to tearing graphene sheets' confinement were caused by the excessive pressure or thermomechanical stress generated from high kinetic energy fragment dispersion. This event did not occur in a few NPs clusters, indicating that the larger cluster experienced a greater effect during the light-induced reaction.

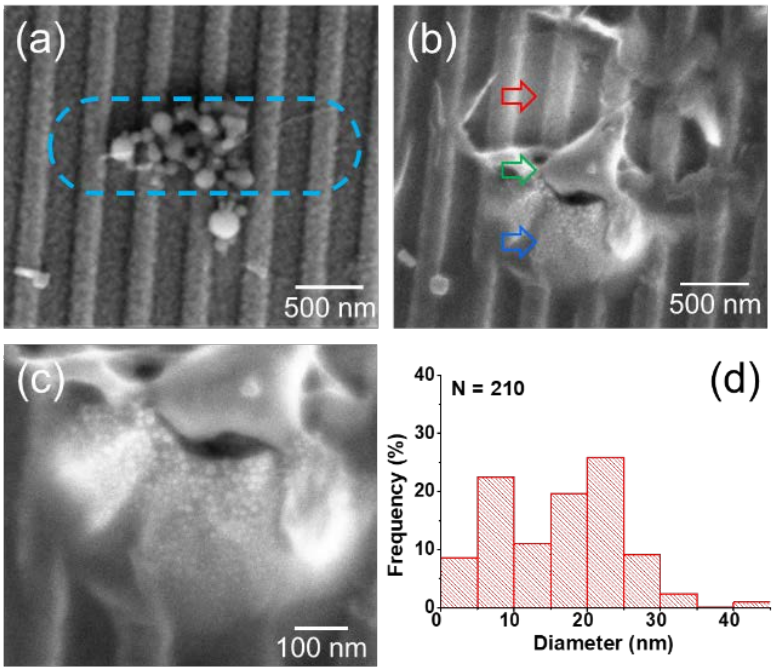

Figure 3-15. (a) SEM images reveal the morphology of the Al NPs in graphene sheets aligned to the laser profile (dotted line). (b) A 7-µs 446 nm blue laser irradiation initiates drastic morphological changes, including the torn graphene sheets (red arrow), molten sintered lump (green), and dispersed fragments (blue). (c) Al droplets were displayed with high magnification SEM images. (d Size distribution of nanofragments less than 50 nm is plotted while the frequency of larger fragments is negligible.

Sintering has been one of the limiting factors in the Al NP combustion mechanism [144]. Recent literature has shown that graphene has significantly reduced the sintering with neighboring particles by removing heat from the fragments/droplets and transmitters through conduction [145]. Our observation (**Figure 3-15** green arrow) shows that the isolated nature and proximity among the initial NPs trapped between the graphene made sintering unavoidable. While the thermomechanical force impact from the NPs explosion can be seen beyond the cluster area, however, the remaining graphene sheets appear to capture the nanofragment dispersion (**Figure 3-15**, blue arrows). The top graphene layer can provide mechanical confinement to contain the dispersed Al fragments and assist the physical confinement by trapping the built-up pressure.

A closer inspection of the dispersed fragments in **Figure 3-15(c)** indicates that graphene confinement captured the fragment dispersions, while its distribution was summarized in **Figure 3-15(d)**. Note that the distribution was accounted for those on the top surface imaged in SEM, while the lower nanofragments were not captured. Interestingly, we observed the nanofragments have a spherical morphology, attributed to the ejecta spallation or the condensed Al vapor onto the graphene. These nanosphere droplets may occur due to the rapid nature of the condensation, which favors the kinetic formation of particles for a thermodynamically favorable morphology [146]. After the laser irradiation diminished, rapid quenching of ejecta's thermal energy can achieve a cooling rate of ~10^3 K/s via the conductive graphene sheets [145]. The grating substrate will act as a heat sink and further accelerate the cooling rate. Removal of accumulated heat prevents the formation of particle coagulation and stabilizes the condensed nanosphere fragments.

The presence of graphene can trap the hot molten aluminum and act as a nucleation growth site for Al ejecta. Recent work reported using graphene sheets as part of the in-situ synthesis process to form nano-Al. A rapid 10-ms Joule heating platform was used to vaporize micron-sized particles and the vapor nucleates to produce uniformly distributed nanoparticles on reduced graphene oxide (RGO), as shown in **Figure 3-16Error! Reference source not found.** [142]. Initially, micron-Al powder (99.5%, Sigma Aldrich) was prepared in ethanol, then mixed into graphene oxide (GO) solution with a weight of 1:1. Ultrasonication mixed the GO sheets and monodispersed micron Al particles. In contrast, the GO sheet is an excellent surfactant to disperse Al micro-powders to form a uniform Al-GO suspension. The paper extensively discusses the reduction and filtration of the materials [142]. The experimental joule heating technique could heat the particles to temperatures of ~1700 K. The heating caused the Al constituents to melt and possibly evaporate. As cooling takes place, the nucleation occurs around the defects on the RGO network and accretes Al atoms to form ultra-fine nanoparticles. Coalescence of the nanoparticles was separated by in-plane graphene defects and several layers of graphene that serve as barriers. Confinements by defects of the RGO resulted in spherical nano-sized particles of 5-40 nm as characterized by SEM.

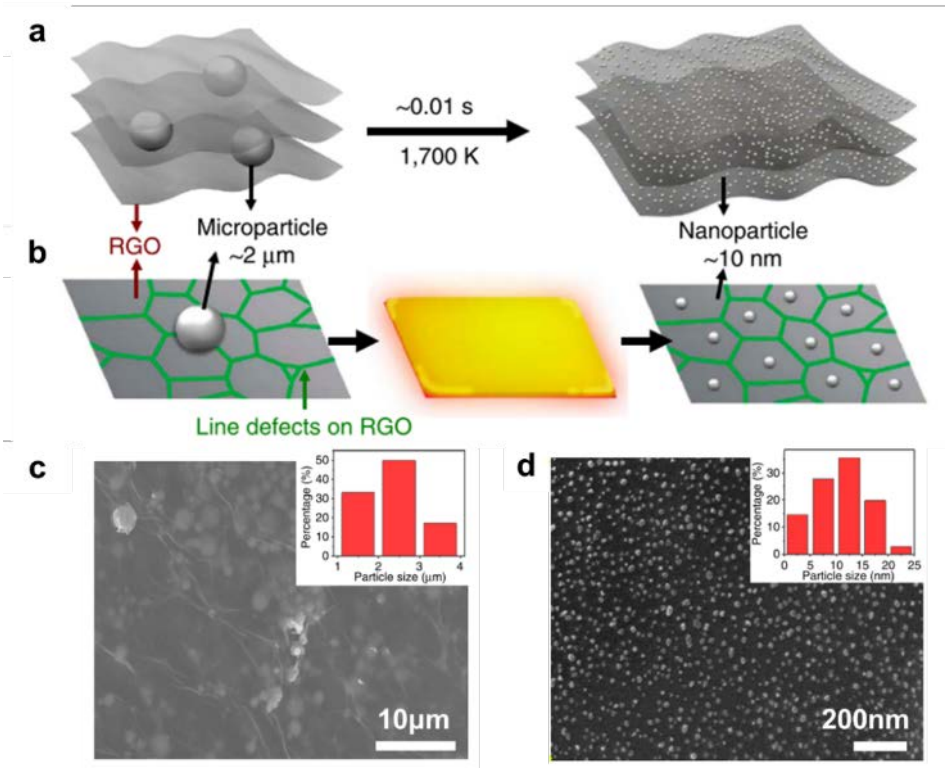

Figure 3-16. Schematic and characterization of in situ nanoparticles self-assembly process. (a) Micron-Al particles in the RGO matrix are self-assembled and reacted into nanoparticles driven by direct Joule heating. (b) Proposed mechanism for nanoparticle formation, where a micron-Al particle melts on heating and self-assembles into nanoparticles due to confinement by the defects of the RGO sheet. SEM image of RGO films with embedded micron-Al particles (c) before and (d) joule heating treatment. The figure is obtained from [142].

3.6 Proposed Reaction Mechanism

For our case, the absorption efficiencies for Al NP without and with a grating substrate are 0.265 and 1.77, respectively. These values are based on the absorption efficiency simulation of 120 nm Al NP in an air medium. Using the simulated absorption efficiencies and the equation **(**1.2**)**, the minimum fluences for MDM are $F_{NP} = 0.46\, J/m^2$ and $F_{NP+GR} = 0.069\, J/m^2$ for Al NP without and with a grating substrate, respectively.

As previously mentioned, MDM requires a heating rate lasting less than 6.4×10^{-5} s for our experiment. Based on our calculation above, the expected regions for MDM

are drawn in the orange and red shaded areas for Al NP without and with a grating substrate, respectively, in **Figure 3-17**.

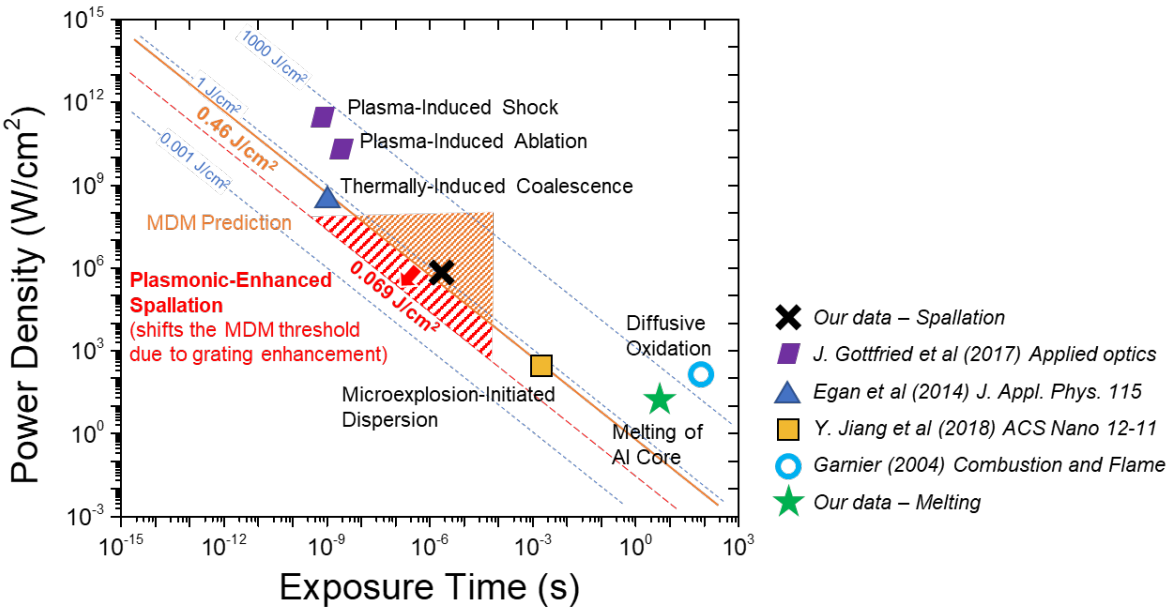

Figure 3-17. Recent works on photothermal-initiated Al particles reaction mechanisms are plotted to the experimental parameters, namely the heating source's peak power density and exposure time. Each diagonal line, representing the laser fluence, is calculated from the range of energy deposited and its irradiation time. Our data is also included for comparison.

Our presented experimental results show that spallation can be initiated via photothermal heating enhanced by a plasmonic grating substrate. As seen in the figure, our laser setup range (marked as ✖ in **Figure 3-17**) is in the order of several microseconds with a power density of ~ 10^6 W/cm^2. By using the plasmonic grating, **plasmonic-enhanced spallation** (red region) of nano-Al particles was observed in our experiment. The plasmonic enhancement was achieved by coupling the electric field of the laser to the Al NPs cluster and the plasmonic configuration. We can achieve the effect of a higher power density by adjusting parameters to construct more optimum electromagnetic field coupling conditions. For example, we select the nanoparticle's optimum medium coupling and optical absorption of laser wavelength,

as shown in **Figure 3-3**. As shown in the calculation, the plasmonic grating shifted the minimum fluences for MDM from $F_{NP} = 0.46\,J/m^2$ to $F_{NP+GR} = 0.069\,J/m^2$ by incorporating the grating substrate. Therefore, we can observe spallation in our laser heating experiment by using the grating substrate.

3.7 Aluminum Particles Reaction on MoO_3 Flakes

Next, the photothermal laser heating experiments are conducted on Al particles residing on MoO_3 flakes. **Figure 3-18** compiles the products of laser irradiation at the target particles at different sizes: (a) 50 nm, (b) 80 nm, (c) 120 nm Al nanoparticles, and (d) 3-5 μm Al microparticles. Spallation of the nanoparticle by photothermal heating has been observed in the absence of a solid oxidizer. The introduction of a nearby oxidizing agent may shed light on how the hot ejecta interacts with the readily available oxidizer. The nano-Al 80 nm particles result shows the most violent reaction among the different nano-Al particles in **Figure 3-18(a-c)**. High-resolution SEM after laser irradiation reveals prominent reaction sites at the MoO_3 flake and grating substrate. Three types of ejecta are found, namely, 1) nano-sized 'light-colored' fragment, 2) the nanofragment with an underlying darkened region, and 3) sintered lump.

The first type of the ejecta is the light-colored nanofragment mainly observed further away from the initial target particle location indicated by the red dotted profile of the laser area. The spalled hot molten Al may react in the air and cooled off after landing on the grating. The irregular shaped and dimensions of the ejecta appears similar to the experiment of nano-Al particles on a grating substrate, as shown in **Figure 3-7**. The nano-sized ejecta is thought to be alumina after being oxidized as no scattering signal was detected in the scattering images, as shown in **Figure 3-18(c)**.

However, one might argue that the ejecta is too small to be detected by the scattering imaging. As a comparison, any metal content in the ejecta or sintered lump will scatter light, as indicated by yellow arrows in **Figure 3-18(a-b)**.

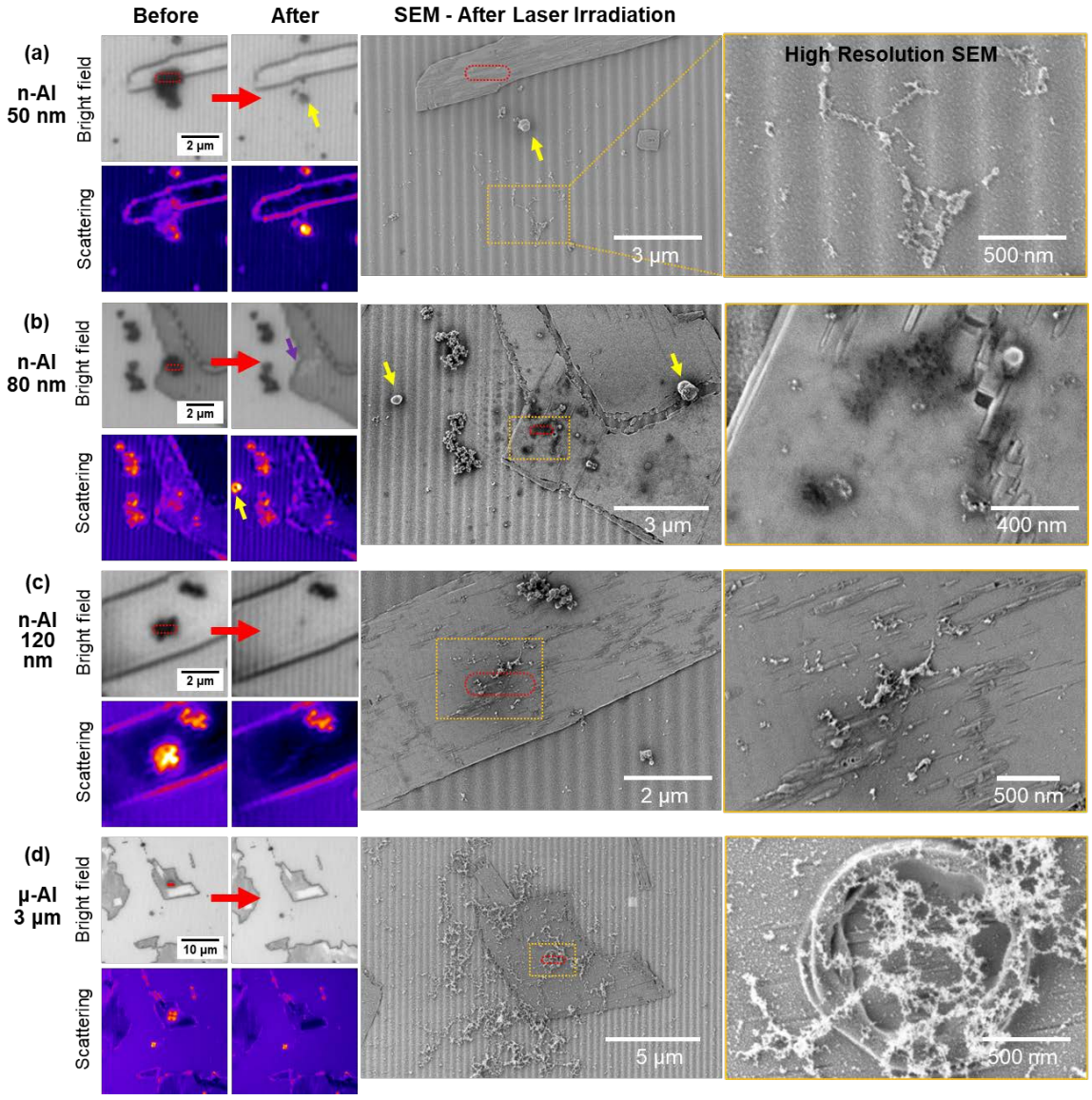

Figure 3-18. Optical microscope images capture the sample morphology before and after laser irradiation, while SEM reveals the high-resolution post-reaction imagery. The different data sets are (a) 50 nm, (b) 80 nm, (c) 120 nm nano-Al, and (d) 3-5 µm micron-Al particles on MoO_3 flakes on the silver grating substrate.

The second type of ejecta with an underlying darkened region is frequently observed in proximity to the initial cluster location irradiated by the laser. In SEM, a

dark spot typically means a less intense SEM signal captured by the detector, which is the secondary electron detector in this case. In such a case, secondary electrons with small energy are influenced by a local charging after the Al NP reaction or a nanostructure, e.g., nano-porous, created by the Al NP reaction. These factors potentially disturb the secondary electron trajectories. As a result, the secondary electrons do not enter the detector, and part of the image appears dark.

Many darkened regions, found both on the MoO_3 flake or grating substrate, may indicate a sub-surface phenomenon after the ejecta landed. When the ejecta landed on MoO_3 flake, the hot ejecta is directly in contact and can react to readily available MoO_3. Once several nano-Al particles initiate the reaction, the heat generated can create a subsequent high heating rate and temperature sufficient for spallation to the rest of the particle cluster. Therefore, as observed by SEM in **Figure 3-18(b)**, a local secondary reaction may occur after the ejecta landed on MoO_3. The extensive nature of the response can also be seen in the change in optical properties of the MoO_3 flake, as shown in the purple arrow in the bright field image after laser irradiation. Furthermore, the ejecta could also land on the grating substrate. As previously mentioned, the grating is made of 100 nm silver layer capped with a 10-nm alumina layer. When hot aluminum ejecta landed on the grating, phase transformation of the grating's alumina layer may be initiated. Different alumina phase, including from amorphous, γ-Al_2O_3, θ-Al_2O_3 to α-Al_2O_3 can be formed between temperature of 800 – 1,400 K [121]. For instance, the transformation of θ-Al_2O_3 to α-Al_2O_3 takes place in the temperature range 1050–1200 °C. These different alumina phases are associated to different physical densities which may alter their interaction to the SEM's secondary electron imaging.

The third type of ejecta is the ~500 nm sintered spherical lump that has traveled above 5 um away from the initial location, shown in **Figure 3-18(b)**. Visual observation of the reacted volume of the MoO_3 flake suggests that most of the lump's content may come from the Al NP cluster. Aluminum may comprise the majority content of the sintered lump as it is highly scattering, as pointed by the yellow arrows in **Figure 3-18(b)**. Additionally, the lump formation may be associated with reactive sintering of Al particles aggregate. A condensed-phase reactive sintering mechanism generally occurs on particles aggregate in surface contact, leading to rapid melting and coalescence into larger structures [140].

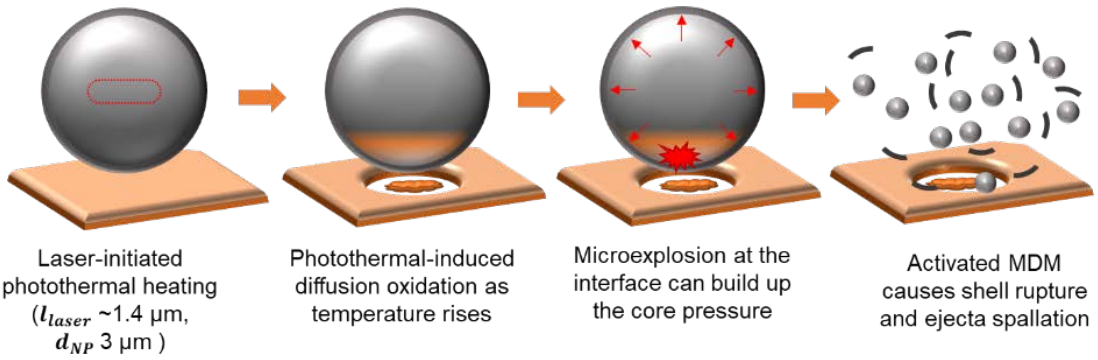

Figure 3-19. For micron-Al particles, the first stage reaction may occur at the contact area between the fuel-oxidizer, potentially via a diffusion mechanism. Then the exothermic reaction initiates the secondary reaction, which is MDM, indicated by the spallation of the Micron-Al.

For the micron-Al particles residing on the MoO_3 flake, intense spallation was also observed, as shown in **Figure 3-18(d)**. Previous observations indicate that micron-Al particles on the grating substrate did not experience spallation. This finding suggests the importance of MoO_3 in initiating the reaction. For micron-Al particles, the governing reaction mechanism cannot be MDM initiated by plasmonic enhanced spallation. Instead, the reaction was observed with the presence of MoO3. This shows first stage reaction may occur at the contact area between fuel-oxidizer, potentially via a diffusion

mechanism. The diffusion oxidation mechanism or condensed phase reaction in the contact point of the micron-Al particles and MoO_3 flake is highly likely to act as the initiating event [47]. Then the exothermic reaction initiates the secondary reaction, which is the MDM, indicated by the spallation of the Micron-Al. After micron-Al particles react, the spallation may first occur and be followed by extensive nucleation between nearby ejecta. Chain-like aluminum oxide nucleation and growth indicate that hot molten aluminum reacted slowly with available O2 at low temperature or with a low O_2 concentration [139]. The ejected material of the micron-Al particle is more abundant in volume than its nano-sized counterparts. Based on a simple volumetric calculation, the micron particle has Al core content roughly two orders of magnitude more than a cluster of nanoparticles. Consequently, the ample amount of nanofragments ejecta at proximity may create chain-like nanostructures, as shown in the high-resolution SEM in **Figure 3-18(d)**.

3.8 Conclusion

To summarize this section, our experiment demonstrated the effect of low and high heating rates targeted to specific Al NPs clusters by local laser-induced heating. The plasmonic grating enhanced the electric field and generated a rapid photothermal heating rate. Graphene sheets were utilized to provide plasmonic, chemical, and mechanical confinements. In addition to keeping the Al NPs chemically inert, graphene is subjected to its optical properties that benefit the coupling of laser wavelength and Al absorption in different mediums. The fast-heating rate generates nanofragment dispersion in the graphene encapsulation.

Our experimental data has shown nanofragment dispersal of isolated Al particles in a fast-heating environment with a heating rate of $>10^8$ K/s. Nano-Al particles results

indicate that the smaller fuel particles dimension may be ignited easily, while the hot ejecta may react to the neighboring oxidizer. The reaction of micron-Al particles residing on the MoO3 flake shows an exciting finding. The first stage reaction may occur at the contact area between fuel-oxidizer, potentially via a diffusion mechanism. Then the exothermic reaction initiates the secondary reaction, which is MDM, indicated by the spallation of the Micron-Al. This can be beneficial for enhancing combustion performance by intermixing the oxidizer with both micron-Al and nano-Al particles. Further, the combination of nano-fuel and nano-oxidizer is widely known to have a superior combustion performance and will be presented in the next Dissertation chapter.

CHAPTER 4 : COMBUSTION STUDY OF ALUMINUM NANOPARTICLES AND EXFOLIATED 2D MOLYBDENUM TRIXODE

Exfoliated two-dimensional (2D) molybdenum trioxide (MoO_3) of approximately 3-4 monolayers in thickness was produced from sonicating bulk MoO_3 powder and then mixed with 80 nm diameter Al nanoparticles to prepare nanoenergetic composites with high interfacial contacts between the fuel and oxidizer. Combustion measurements demonstrated peak pressures as high as 42.05 ± 1.86 MPa, pressurization rates up to 3.49 ± 0.31 MPa/μs, and linear combustion rates up to 1,730 ± 98.1 m/s, the highest values reported to date for Al/MoO_3 composites. TGA/DSC measurements indicate energetic reactions between the Al and 2D MoO_3 sheets occur prior to the melting temperature of Al. SEM and TEM analysis of the composites prior to combustion suggests a high interfacial contact area between the Al and MoO_3. After the reaction, we observe that the 2D MoO_3 sheets are converted to extended alumina flakes during the reaction in a process attributed to Al adsorption and diffusion processes. These alumina features act as a physical barrier against Al NP sintering while also providing separation for reaction gases to flow and preheat unreacted materials.

4.1 Introduction

Nanoenergetic materials, which are comprised of fuel (Al, Li, Si, etc.) and oxidizer (CuO, Bi_2O_3, MoO_3, Fe_2O_3, etc.) constituents with nanoscale dimensions, benefit greatly from the enhanced surface area of interaction between fuel and oxidizer. [12,25,27,29,40,48,134,135] Reduced particle dimensions improve the homogeneity of the mixture, to minimize barriers between reactants and decrease the diffusion distance required for reactions [25,26,29,135]. Previously, researchers have

employed fuel and oxidizer particles having a rich variety of morphologies such as spherical nanoparticles, [147] nanosheets [27], nanorods [134], and nanowires [29] to synthesize nanoenergetic formulations. Most recently, we have reported the self-assembly of Al and Bi_2O_3 nanoparticles directed on to 2D functionalized graphene sheets to synthesize novel nanoenergetic materials with enhanced combustion performance [115]. In these works, functionalized graphene oxide (FGO) was used as an energetic additive (only up to 5 wt. %) and our main oxidizer was Bi_2O_3. The significant improvement in combustion performance is a result of employing 2D FGO stimulated our interest to employ 2D metal oxide such as MoO_3 as an exclusive oxidizer and to study the impact on the combustion performance. Though MoO_3 had been used as an oxidizer in energetic formulations in the past, the MoO_3 material used was a regular micron sized particle [8,42,148]. Furthermore, we have conducted an in-depth study on the combustion mechanism of self-propagating reactions in nanoenergetic composites prepared using 2D oxidizers.

In this work, we report the synthesis of gram scale quantity of 2D MoO_3 nanoflakes per batch by exfoliation of layered bulk MoO_3 utilizing ultrasonication energy, following the method reported by Coleman [13]. Though other methods to produce 2D materials including laser thinning, micromechanical cleavage, and vapor phase deposition have been reported in the literature [39,45,149], scaling up the synthesis is difficult. Aluminum nanoparticles (Al NPs) were used as fuel due to their ability to generate large heat of combustion upon reaction with an oxidizer. Al NPs were assembled on the surface of ultrasonically exfoliated 2D MoO_3 sheets to produce nanoenergetic composites with close proximity between fuel and oxidizer. The physical and morphological properties of 2D MoO_3 sheets were examined for homogeneity of

mixing with Al NPs. The pressure – time and combustion wave speed measurements were performed and compared to similar composites prepared using bulk MoO_3 powder. Effects of slow and fast heating rate ignition on the combustion mechanisms were evaluated across a range of ignition heating rates. The Al/MoO_3 nanocomposites were characterized using a host of characterization tools such as zeta potential analyzer, scanning electron microscope (SEM), transmission electron microscope (TEM), atomic force microscope (AFM), X-ray diffraction, energy dispersive X-ray analyzer (EDAX) and simultaneous thermal gravimetric analysis (TGA)/differential scanning calorimeter (DSC).

4.2 Material Preparation

Micron size molybdenum trioxide ACS Reagent 99.5% grade powder (Sigma Aldrich) was used as the precursor for liquid exfoliation process to produce nanosheets. It was also used directly to produce micron MoO_3/Al composites. Aluminum nanoparticles (Nova Centrix) with an average particle size (APS) of 80 nm, a 2.2 nm oxide shell thickness, and 79% active content were used as the fuel in the nanoenergetic composites. Isopropyl alcohol (Sigma Aldrich, HPLC grade, 99%) was used in the MoO_3 liquid exfoliation process as well as in the synthesis of nanoenergetic composites.

The morphology and structure of the MoO_3 powder precursor were first investigated using SEM. As seen in **Figure 4-1**, the majority of the MoO_3 precursor material is composed of particles from several to tens of micrometers in length and width. Average particle thickness was estimated to be several micrometers.

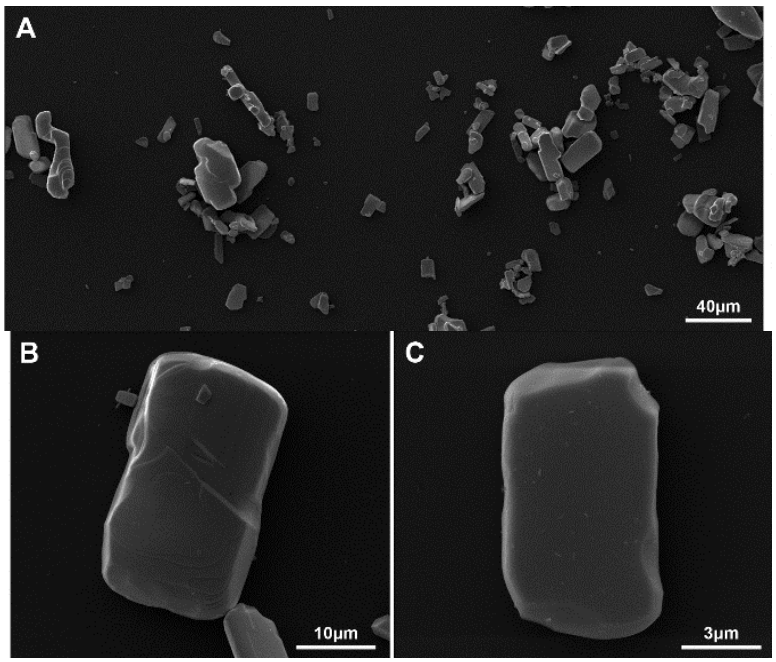

Figure 4-1. SEM micrographs of as-received MoO_3 starting material. (a) The MoO_3 powder dimensions ranged from several to tens of micrometers shown. Higher magnification (b and c) reveals the rectangular shape and layered structure of MoO_3.

4.3 Sonication Process

Molybdenum trioxide powder was oven dried at 100°C prior to exfoliation to ensure moisture was removed. The powder (24 g) was added to 2-propanol, IPA (80 mL) to produce a 300 mg/mL dispersion. IPA provides high stability dispersions of MoO_3 sheets indicated by the zeta potential as discussed later. 53 mL of the solution was placed in an external ice bath maintaining a temperature around 0°C during the sonication process to avoid any overheating. Ultrasonication equipment was Misonix 00 sonic wand with 60 W pulsed power with a duty cycle of 9 seconds on and 2 seconds off for 10 hours. The sonication process, especially the sonication power, was optimized mainly to produce enough energy to break weak interlayer van der Waals bonds and produce exfoliated 2D sheets from the bulk MoO_3. Many well-established methods have been developed and referenced to compare to our method [13]. To separate exfoliated sheets from the bulk powder, the dispersion was

centrifuged for 50 minutes at 3434xg. The residual material was then subjected to further sonication and centrifugation processes. The 2D MoO_3 sheets were then dried at 60°C in a vacuum oven.

The morphology of MoO_3 after sonication was examined using AFM to study the exfoliation process. Previously sonicated and dried MoO_3 material was diluted in IPA, treated in an ultrasonic bath for an hour, and dispersed on a silicon substrate. Representative AFM micrographs, shown in **Figure 4-2**, indicate the exfoliated MoO3 nanosheets have two major distributions in regard to their lateral dimension. Numerous sheets assembled into edge-assembled islands that averaged 742 nm and 2.16 nm in length and thickness, respectively. Individual flakes exhibited and an average of 133 nm and 1.72 nm in length and thickness, respectively. The individual sheets assembled through edge defect interaction in a manner similar to graphene [150]. When comparing these dimensions to the original MoO_3 powder, it is evident that the sonication did not only break the van der Waals plane-to-plane bonding, but also the in-plane bonding of the initial MoO_3 crystalline structure. Based on thickness measurements, the MoO_3 nanosheets after sonication contain 3-4 layers of the material, where an atomic layer is 0.6 nm thick [151,152].

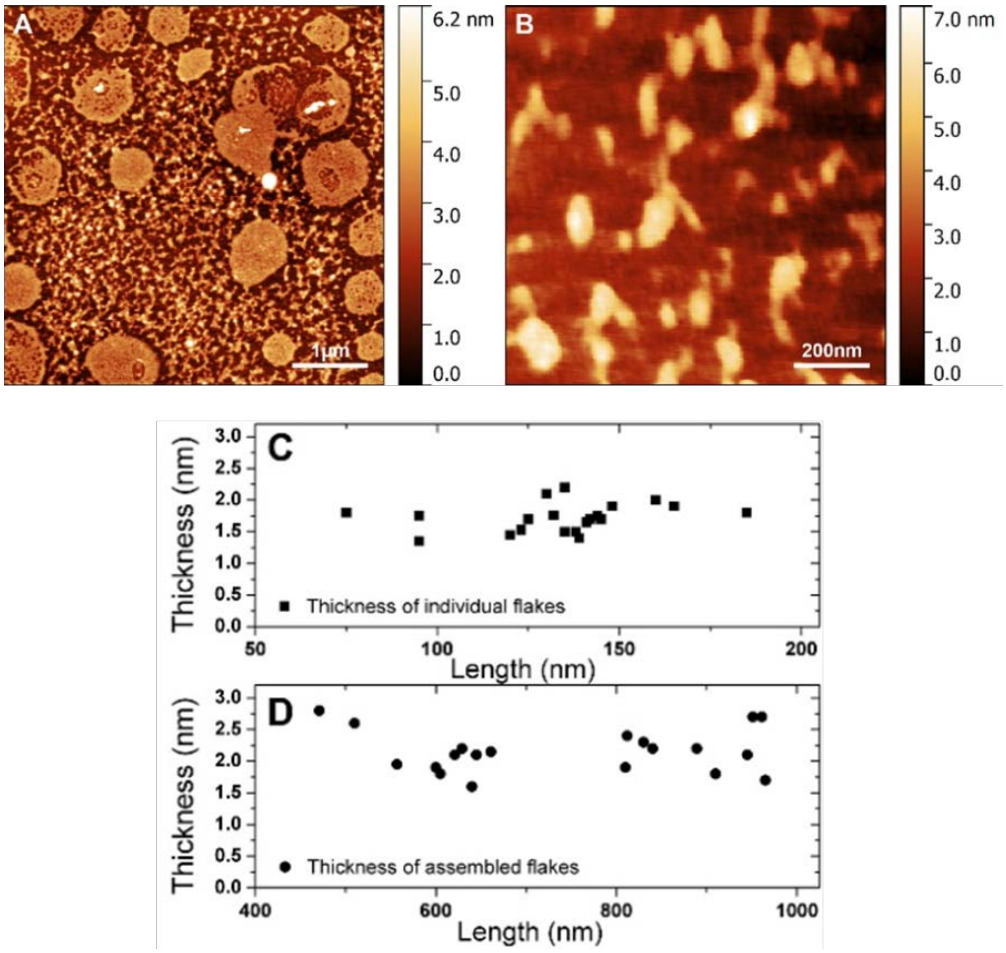

Figure 4-2. (a) AFM micrographs of MoO_3 after sonication may be found as large edge-assembled sheets (b) isolated flakes. The distribution of flake thickness as a function of lateral length for (c) isolated flakes and (d) edge-assembled sheets.

The stability of a suspension is determined by the degree of short-range and long-range forces in colloidal dispersion and can be measured by the zeta potential [153]. Zeta potential measurements were performed on the constituents to study their stability and to understand their electrostatic interaction. Our result indicates that the zeta potential of Al nanoparticle is +34.28 ± 1.61 mV. Similar measurements of MoO_3 after sonication had a zeta potential of -49.43 ± 0.72 mV. These relatively large zeta potential magnitudes indicate that each material is a stable colloidal dispersion. After sonication, repulsive electrostatic forces between nanosheets/nanoparticles prevent

particle agglomeration in suspension. Both Al NPs and MoO_3 nanosheets produced by ultrasonic exfoliation remained dispersed well in the suspension for at least five days if left undisturbed.

4.4 Assembly Procedure

Various Al/MoO_3 composites were prepared by using either the as-purchased MoO_3 powder or exfoliated 2D MoO_3 sheets for experimentation. To obtain a specific fuel-to-oxidizer mass ratio, MoO_3 and Al NPs were mixed in equivalence ratios from 1.0, 1.2, 1.4 and 1.6. These equivalence ratios were calculated considering the aluminum oxide shell thickness of 2.2 nm and 79% active Al weight percentage. Each constituent material was separately weighed and ultrasonically dispersed in 1 mL of IPA for 3 hours using an ultrasonic bath to ensure stable precursor dispersions. Then, MoO_3 and Al NPs suspensions were added and ultrasonically mixed for another 1 hour. After sonication, the homogeneous mixtures were vacuum-dried at 60 °C for 3 hours to evaporate the IPA.

It is worth noting that there is a small portion of the MoO_3 material remains in bulk size due to our inability to filter them out completely during the centrifugation process. However, a majority of the MoO_3 is observed to be thin sheets, as observed in **Figure 4-3**. The opposing zeta potential polarities of the constituents facilitate assembly of Al NPs and MoO_3 nanosheets due to electrostatic attraction. **Figure 4-3** illustrates the ordered layer-by-layer assemblies of Al and MoO_3 produced after mixing. The intimate contact between fuel and oxidizer that may greatly improve the reaction kinetics. A small portion of samples also shows random mixing of Al and MoO3 2D sheets (**Figure 3(a)**). Increased magnification, shown in **Figure 4-3(b-c)**, further illustrates that the

exfoliation process created 2D MoO_3 sheets that are thin enough to be electron transparent, as Al particles may be observed underneath the sheets.

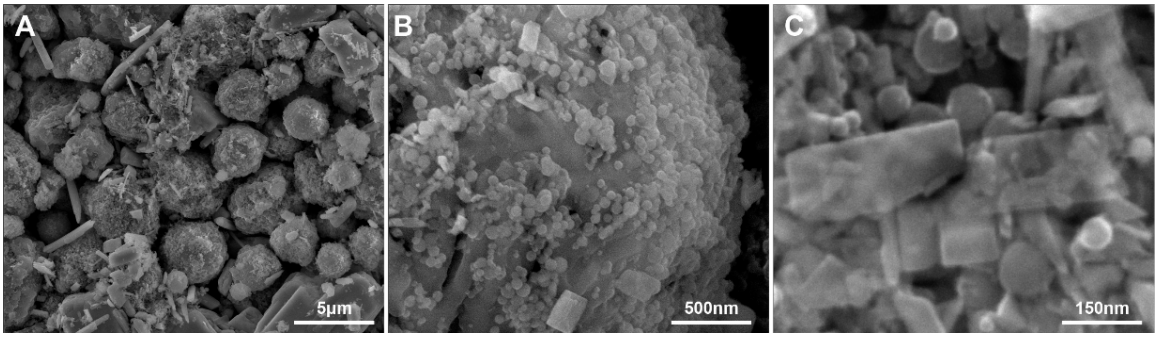

Figure 4-3. SEM micrographs showing (a) self-assembled clusters of tightly-packed Al nanoparticles and MoO_3 sheets showing long-range order to many microns. (b) Higher magnification of one of the clusters shows the intimacy of Al and MoO_3. (c) The 2D morphology of the MoO_3 flakes is readily apparent on the surface of the randomly mixed nanoenergetic composite.

4.5 Material Characterization

The zeta potential, thermal, and surface properties of the constituent materials and mixed composites were characterized using a variety of techniques. Zeta potential and particle size of the material were measured using a Delsa Nano C instrument (Beckman Coulter). Thermal characterization of Al/MoO_3 nanothermite was conducted using a TGA/DSC (TA Instruments Q600-SDT) with dual beam balance. Six milligrams of each sample was evenly dispersed to cover the entire base of the sample container and provide good thermal contact. The sample was heated from room temperature to 1400°C at a rate of 20°C/min under an argon flow. Surface morphology and elemental analysis of the materials were examined using several characterization techniques. A Bruker Innova atomic force microscope (AFM) was used to observe the topology of 2D MoO_3 sheets after sonication. An FEI Quanta 600 FEG scanning electron microscopy (SEM) and FEI Tecnai F30 twin 300 kV High-Resolution Transmission Electron Microscopy (HRTEM) were used at various stages of processing to inspect

the nanoenergetic material composition. Energy dispersive X-ray spectroscopy (EDS) was used in both SEM and TEM to provide elemental analysis of the corresponding material. The HRTEM is equipped with an Oxford ultra-thin window EDX detector, a Gatan ultra-scan, and Fischione high angle annular dark field detectors for STEM imaging. Powder x-ray diffraction (XRD) patterns were recorded on a Rigaku Ultima IV powder X-ray diffractometer operated at 44 kV and 44 mA using a copper X-ray radiation (λ =1.5438 Å). Samples were scanned for XRD patterns from 10^o to 80^o (2θ) with a step size of 0.02^o and scanning speed of 2^o /min.

Nanothermite materials were prepared correspondingly to each microscopy measurement. For AFM imaging, 100μL of dispersed material in IPA was drop cast on an AMD-cleaned low-doped silicon wafer. The sample was then dried under vacuum for 2 hours. Electron microscopy imaging was performed before and after slow and fast heating. For SEM inspection small amount of each material was deposited onto carbon tape adhered to an SEM stub. Diluted solutions in IPA with 0.001 mg/mL concentration were deposited on a lacey carbon grid for TEM inspection.

4.6 Reactivity Characterization

Nanoenergetic composite combustion was evaluated using a closed pressure cell configuration [27]. More specified details of this reactivity and combustion wave speed measurement setup can be obtained in our previous work. For the confined pressure experiment, 30 mg of Al/MoO_3 nanocomposite powder was loaded into a 6.2 mm diameter and 2 mm deep cylindrical metal well. A 0.13 mm-diameter Ni-alloy fuse wire was used as an ignitor by applying a DC voltage pulse. Pressure release was recorded using a piezoelectric pressure sensor (PCB Piezotronics Model 119B12), which was

clamped to the top of the cylindrical metal well after the fuse wire had been installed. Schematics of these measurement setups are shown in **Figure 4-4**.

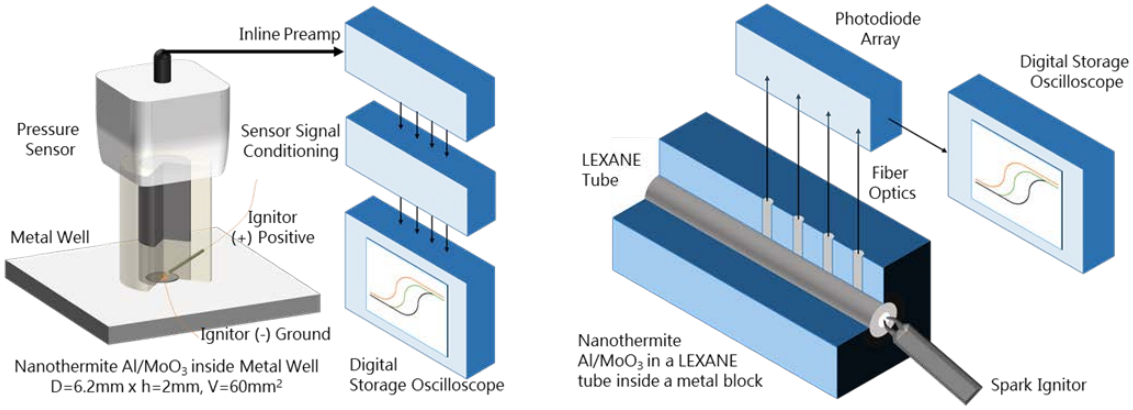

Figure 4-4. Reactivity (left) and combustion speed (right) measurement setup schematics

Linear combustion rate was recorded using an optical sensing method [27]. The experimental setup consisted of a transparent Lexane tube with a dimension of 95 mm length, 9 mm outer diameter, and 3.2 mm inner diameter. Approximately 200 mg of nanocomposite material filled about a half of the tube cross-section at one end of the tube. A spark plug ignited the powder at one end, and a lid confined the other end of the tube. The tube resided within an aluminum block with up to eight fiber optic channels separated by 10.0 mm along the length of the block. Light propagation during combustion was captured via a photodiode array connected to a Tektronix TDS3014B digital oscilloscope. More detailed descriptions of the pressurization rate and linear combustion rate measurement configurations are provided in our previous work [115,154].

4.7 Slow Heating Reaction by TGA/DSC

Data from TGA/DSC measurements of 2D MoO_3 sheets alone is presented in **Figure 4-5(a)**. Note that the instrument was calibrated using several known materials to facilitate the determination of total heats of reaction. A broad exothermic peak

initiated at a temperature above 350°C. Two strong endothermic peaks at 785.76°C and 827.33°C, representing the melting and the decomposition temperatures of MoO_3, respectively, were accompanied by a significant weight drop of about 84.95%. The nanoscale confinement of the MoO_3 sheets may be responsible for reducing the bulk melting MoO_3 temperature of 795°C [52].

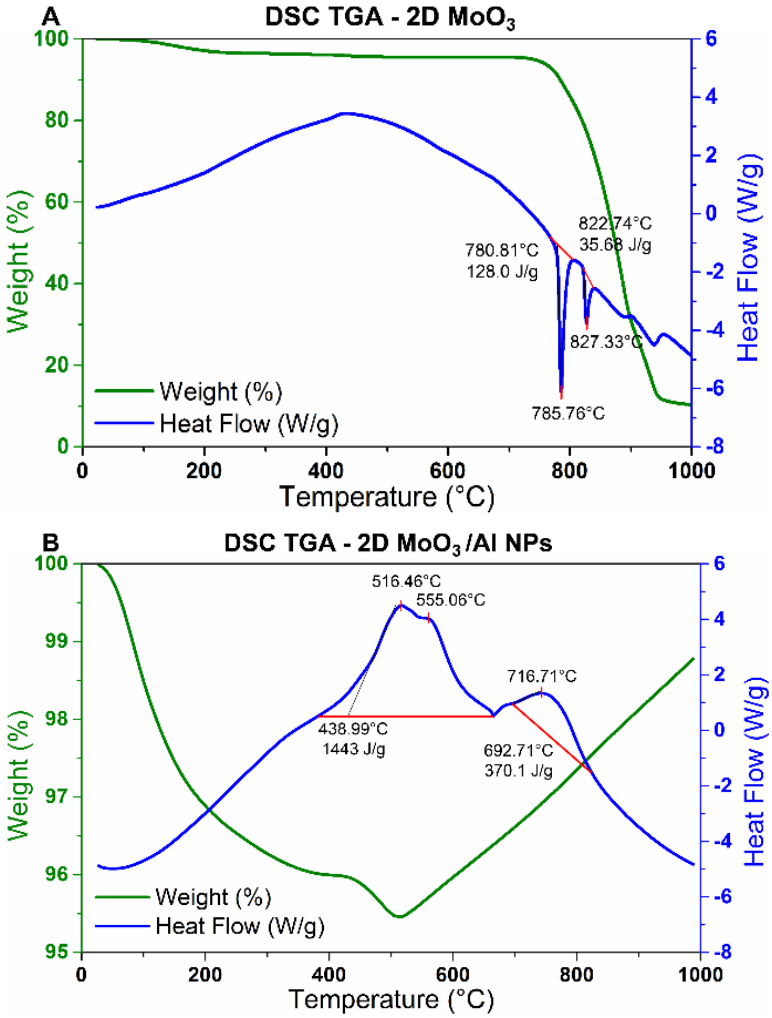

Figure 4-5. TGA/DSC corrected baseline curves of (a) 2D MoO_3 nanosheets and (b) Al/MoO_3 nanocomposites with an equivalence ratio of 1.4.

A baseline corrected TGA/DSC measurement of the composite of Al NP and MoO_3 2D sheets at 1.4 equivalence ratio is presented in **Figure 4-5**. An exothermic peak with an onset temperature at 438.99°C and peak temperature at 516.46°C

represents the majority of the thermodynamic reaction in the system, releasing 1,443 J/g. This peak terminates with an endothermic peak at 658°C, indicative of Al melting. Within this temperature regime, Al is in the solid state, and the reaction mechanism is limited by transport of Al through the native alumina shell. In addition to the relatively slow process of Al diffusion, a compositional transformation of the shell could possibly occur from amorphous alumina to γ-Al_2O_3 at 590°C resulting in oxide void formation and exposure of the bare Al core [122]. The escaped Al reacts with available MoO_3, leading to early exothermic activity even before the melting point of the aluminum core [155,156]. An overlap between exothermic oxidation and the endothermic reaction from aluminum melting is observed between 600 to 658°C [52]. A second exothermic reaction occurred with an onset temperature at 692°C and peak at 716°C and produced 370.1 J/g of heating. This peak represents the initiation of liquid-solid reactions, as it is above the melting point of the Al core yet below the melting temperature of MoO_3. The melting of the confined Al inside of an alumina shell leads to volumetric Al expansion that is restricted by the surrounding oxide shell. As a result, the Al core is compressed, and the oxide shell is in tension, further increasing the diffusion rate of the liquid phase Al and providing a driving force to push Al through potential alumina voids.

Regardless of the escape mechanism, Al that is liberated from the shell is free to react with solid MoO_3. Recent density functional theory (DFT) studies indicate that Al atoms may spontaneously adsorb into the top-most layer of a MoO_3 crystal with little to no energy barrier [157]. Upon surface or sub-surface adsorption of Al by MoO_3, the oxygen in the lattice binds more tightly to the Al than to the host Mo, leading to the reconstruction of the MoO_3 surface layer and an exothermic release of energy. The

oxygen is retained in the solid state as the Al is incorporated into the host MoO_3 lattice. In our experiments, a mass decrease of than 5% during TGA/DSC reaction indicates that much of the available oxygen was retained in the solid state in agreement with the proposed mechanism. The proposed reaction mechanism is facilitated by a solid MoO_3 lattice, restricting the temperature regime of this reaction to below approximately 785°C, the melting temperature of MoO_3 observed in **Figure 4-5(a)**. The lack of an endothermic TGA/DSC peak near the MoO_3 melting temperature indicates that the MoO_3 sheets have reacted with Al and are no longer present in the form of MoO_3.

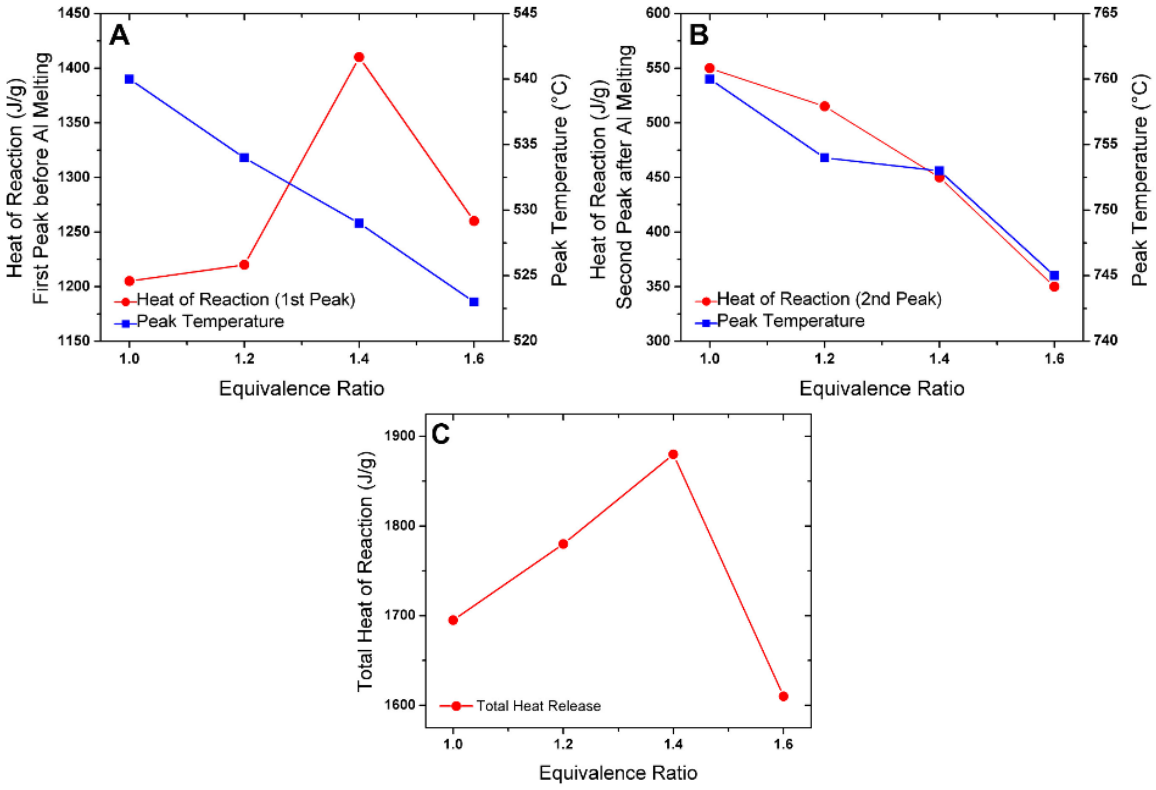

Figure 4-6. The heat of reaction and peak temperature from the (a) first (solid Al) and (b) second (liquid Al) exothermic peaks from Al/MoO_3 as a function of variable equivalence ratio, measured by TGA/DSC. (c) The total heat release from solid and liquid-phase reactions.

TGA/DSC measurements were also performed as a function of Al/MoO_3 equivalence ratio using exfoliated MoO_3 sheets. The first (before Al melting) and

second (after Al melting) exothermic peaks were evaluated, in addition to the temperatures at which the exothermic peaks were observed. **Figure 4-6(c)** shows that as the equivalence ratio increases from 1.0 to 1.6, the temperature associated with the onset of first and second exothermic peaks decreased monotonically by 17^{o}C and 15^{o}C, respectively. In our results, the trend of decreasing peak temperature corresponds to a significant decrease in the heat of reaction occurring after Al melting, as observed in **Figure 4-6**. The heat of reaction in the solid state, prior to Al melting, generally increases with equivalence ratio, with a strong peak at 1.4. The total heat of reaction increases linearly with equivalence ratio between 1 – 1.4 from 1,700 – 1,880 J/g, and then diminished dramatically to 1,605 J/g at a ratio of 1.6. The homogeneity and proximity of 2D MoO_3 sheets and Al nanoparticles provide a reduced diffusion path for reactive species to proceed in the condensed state, resulting in an elevated heat release from the exothermic reaction [158]. Even at low temperature, this additional heat may accelerate reactions between fuel and oxidizer. At equivalence ratios greater than 1.4, we suggest that a relative lack of MoO_3 availability decreases the overall heat of reaction.

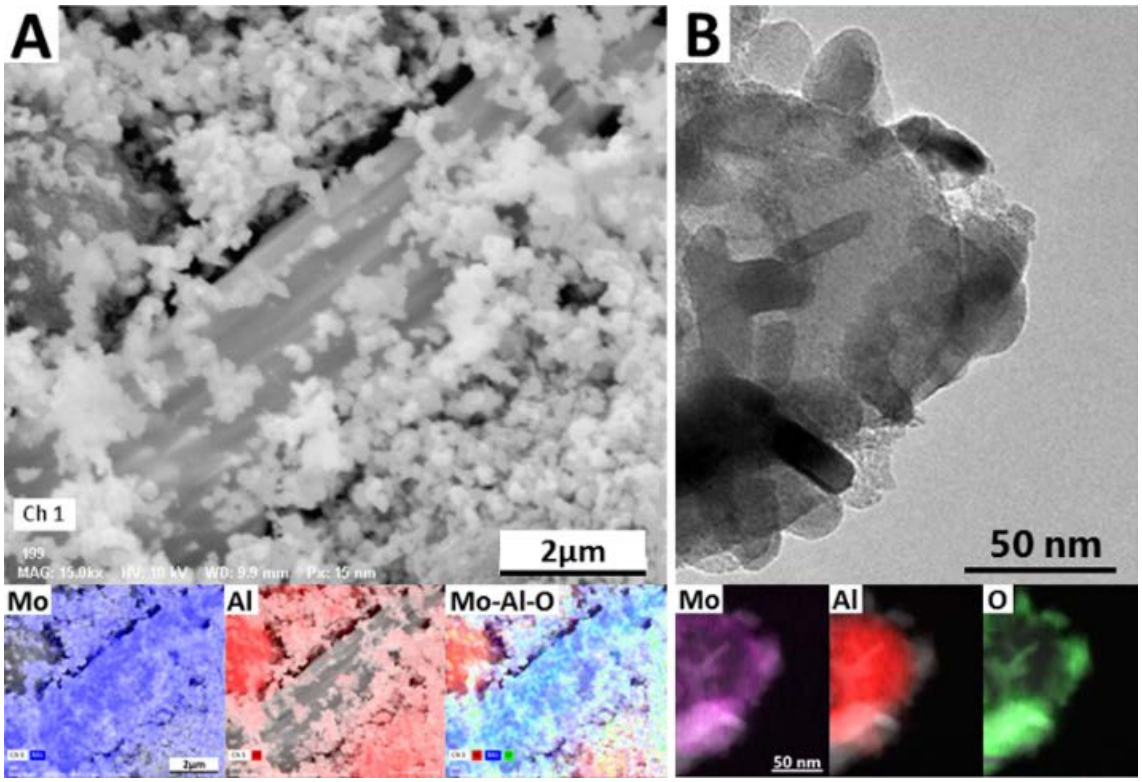

Figure 4-7. Al/MoO_3 sample heated to 575 °C (TGA/DSC) are examined using (a) SEM and EDS mapping and (b) TEM bright-field imaging and EELS elemental mapping. Both analyses show well mixed Al and MoO_3, with nanoscale MoO_3 nodes were only observed residing on the surface of Al nanoparticles in (b).

SEM and TEM analysis of the TGA/DSC product further revealed the morphological evolution and the potential reaction pathways of the nanoenergetic system. Two samples were prepared by limiting the maximum TGA/DSC temperature to 575°C and 1,000°C. The SEM and TEM micrographs of Al/MoO_3 heated to 575°C can be seen in **Figure 4-7**. Low magnification SEM showed numerous Al and MoO_3 nanostructures and some bulk MoO_3 flakes, as seen in **Figure 4-7(a)**. EDS mapping in SEM revealed dispersed Al, Mo, and O throughout the sample. After heating, numerous small nodes appear on the external surface of spherical Al nanoparticles that were not previously present on the Al nanoparticles prior to heating. TEM micrographs of the same material in **Figure 4-7(b)** shows a spherical Al NP with

external nodes containing Mo and O, suggesting that the 2D MoO_3 sheets were mobile on the Al NPs surface during heating and assembled, in part, as oblong nodes along the exterior of the Al NPs. The external surface of the oxide shell appears coarse, and traces of Al are observed outside of the spherical particle using EELS, suggesting some diffusion of Al through the alumina shell. These images suggest that Al diffusion and escape occurs at a temperature lower than the bulk melting temperature of 660°C, as supported by TGA/DSC and by findings that suggest that surface tension in nanoscale particles suppress melting temperature [159].

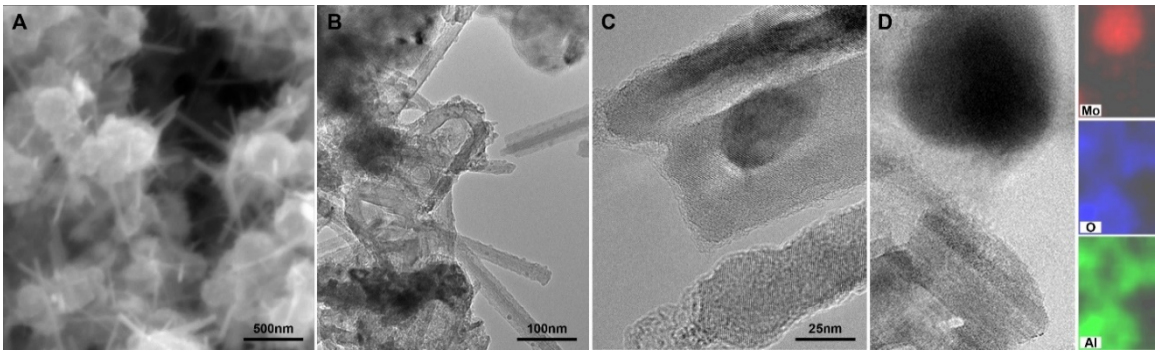

Figure 4-8. Al/MoO_3 sample heated up to 1,000 °C in TGA/DSC are examined under electron microscopy. (a) An SEM micrograph shows that controlled heating produced nanorod-decorated spheres. High magnification TEM micrographs of the needle-like structure (b) and (c) show the crystalline nanosheet structure. (d) TEM EDS mapping shows that the sheets produced during the reaction are comprised of aluminum oxide, while the darker nodes represent particles of reduced Mo.

SEM and TEM analysis of the material heated to 1,000°C by TGA/DSC is shown in **Figure 4-8**. Note that the exothermic reactions observed by TGA/DSC have completed at this temperature, so the observed products represent fully reacted material. SEM inspection shows a dramatic change in nanoparticle morphology. Numerous extended sheets are observed protruding from the spherical nanoparticles. This particle morphology is observed uniformly throughout the sample. TEM analysis (**Figure 4-8(a)**) indicates that metallic Al has escaped the shell, leaving behind a

hollow shell with a thickness (20 nm) that is drastically greater than the original shell thickness. This finding indicates that at least some of the Al from the core has oxidized on the external particle surface. The extended sheets observed protruding from the oxide shell in SEM are also observed in TEM. The sheet widths are on the order of 50 nm, and exhibit lengths extending up to 1 μm. The sheets exhibit long-range crystallinity, as observed in **Figure 4-8(c)**. EDS elemental mapping of the resulting flakes, shown in **Figure 4-8(d)**, indicates that the main constituents of the sheets are alumina, comprised of Al and O. Mo is not found within the flakes, but is rather found in a reduced form as particles dispersed throughout the sample, suggesting that it has been displaced from its original MoO_3 lattice during reaction.

Based on the DFT simulations performed by others [157], we hypothesize that mobile Al anions that escape their shell diffuse on the surface of MoO_3 sheets and are adsorbed by a process notionally shown in **Figure 4-9**. DFT simulations suggest that Al ions are adsorbed beneath the (010) surface of MoO_3 with no energy barrier, while surface adsorption requires overcoming as little as a 0.2 eV energy barrier. Both processes are highly exothermic and are, therefore, self-sustaining. As Al ions are adsorbed, regardless of the adsorption site, oxygen in the lattice migrates from the MoO_3 and towards the Al, forming ionic bonds. The host MoO_3 lattice reconfigures and weakens the bonds between Mo and O. The bond energy between Al and O within the lattice exceeds that between Mo and O, and we hypothesize that at sufficient temperature Mo becomes displaced from the original MoO_3 lattice sites and forms small clusters on the surface of the evolving alumina sheet. The entirety of the MoO_3 sheet is converted to alumina sheet during the process, with the host MoO_3 serving as a solid-state template to facilitate ion exchange from Mo to Al. Aluminum diffusion

may also interact with neighboring MoO_3 sheets that are not in direct contact with the Al NP, thereby grafting multiple MoO_3 host sheets into a single extended alumina sheet. The 2D morphology of the original MoO_3 sheets is critical in this step, as Al adsorption and lattice reconfiguration is limited to the surface MoO_3 layers. As a surface phenomenon, Al adsorption on bulk MoO_3 powder will influence only a fraction of the MoO_3 volume, while a complete transformation occurs when using 2D MoO_3 sheets. Note that **Figure 4-9** schematics are not intended to suggest specific crystalline structures or to indicate specific Al adsorption sites but is rather a phenomenological guide.

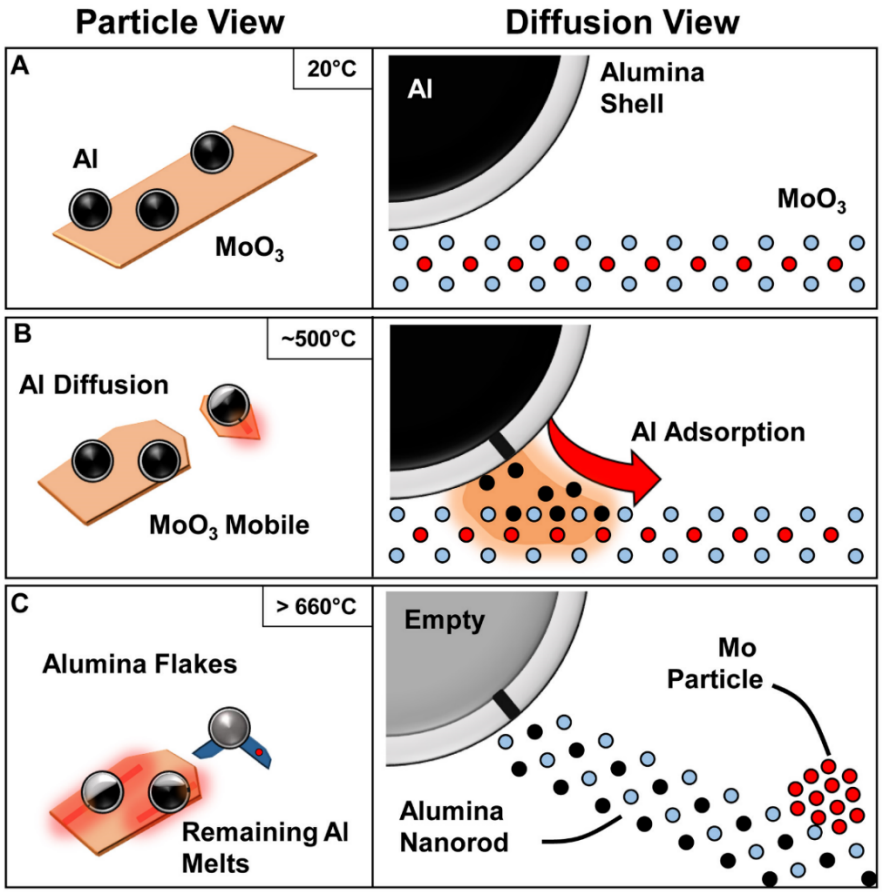

Figure 4-9. Schematic of the proposed combustion mechanism of a nanoenergetic Al nanoparticles and 2D MoO_3 sheets. Note that in all figures, the position of atoms is not meant to denote a specific crystal structure. (a) At ambient conditions, intermixed Al and MoO_3 particles are well mixed. (b) Heating to elevated temperatures leads to MoO_3 migration to

promote intimate contact between solid particles. Al ions escape some of the nanoparticles and begin an exothermic reaction in which Al adsorbs into the 2D MoO_3 lattice. (c) As heating increases past the melting temperature of Al, liquid Al escapes from more of the Al nanoparticles, initiating more Al adsorption and additional energy release. Extended alumina flakes decorate Al NP shells, discouraging particle sintering. Excess heat displaces Mo from the host MoO_3 sheets, leaving behind reduced Mo particles.

The electron microscopy analysis corresponds well to the two exothermic peaks observed in DSC observation. The first exothermic peak represents the diffusion and/or escape of Al through the oxide shell causing a condensed phase and highly exothermic reaction. As the Al remaining in the particle core melts, it is released from the shell to drive the secondary reaction. Furthermore, the extended alumina sheets produced at relatively low temperatures act to separate neighboring Al fuel particles from each other to prevent large-scale agglomeration at the slow (20°C /min) heating rates observed while keeping MoO_3 oxidizer in intimate contact with Al. Because alumina has a greater melting temperature than Al, these alumina extensions are expected to persist at temperatures far greater than those necessary to initiate and sustain combustion. If these surface extensions could be formed and retained during rapid combustion, the particle morphology could encourage the flow of heated gaseous byproducts and oxidizers between Al particles while preventing Al agglomeration and a decrease in reactive surface area.

4.8 Fast Heating Reaction by Reactivity Test

The reactivity of several different equivalence ratios for Al/MoO_3 nanothermite was compared using both as-purchased microscale MoO_3 powder and 2D MoO_3 sheets shown in **Figure 4-10**. Pressurization and combustion speed tests were investigated using equipment and techniques described previously, with a heating rate of approximately 10^8 K/s.

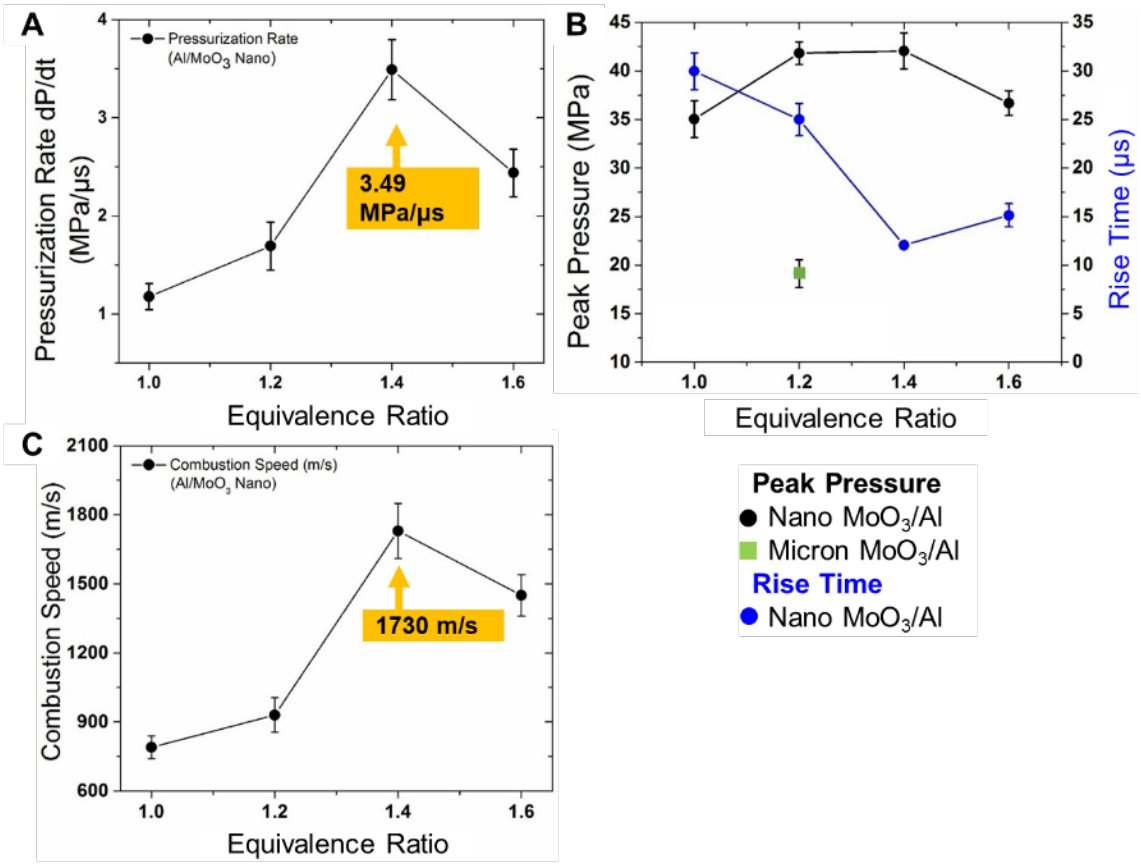

Figure 4-10. Al/MoO_3 combustion testing. (a) Pressurization rate using 2D Al/MoO_3 sheets as a function of equivalence ratio. (b) Peak pressure and rise time for 2D Al/MoO_3 sheets compared to bulk microscale Al/MoO_3 powder. (c) Combustion speed using 2D Al/MoO_3 flakes. An equivalence ratio of 1.4 generates the greatest pressurization rate, peak pressure, and combustion speed.

In the Al/MoO_3 energetic system, reactivity is sensitive to the equivalence ratio of the fuel and oxidizer, in addition to the relative size of each precursor material. In our experiments, we find that an equivalence ratio of 1.4 produces the greatest peak pressure, pressurization rate, and the fastest combustion speed. The optimum equivalence ratio of 1.4 agrees with several previous works [26]. The peak pressure and pressurization rate produced by the Al/MoO_3 nanocomposites are at least two times greater than those produced by the Al/MoO_3 using micron-scale oxidizer particles. At 1.4 equivalence ratio, the peak pressure of micron Al/MoO_3 was 19.2 ±

1.43 MPa with a rise time of 172 ± 9.54 μs, leading to pressurization rate of 0.11 ± 0.02 MPa/μs. Whereas the peak pressure using 2D MoO_3 sheets was 42.05 ± 1.86 MPa with a rise time of 12 ± 0.73 μs, leading to a rate of 3.49 ± 0.31 MPa/μs. The combustion speed of the micron Al/MoO_3 powder was 51.3 ± 7.34 m/s, while nano-scale Al/MoO_3 produces a combustion speed of 1,730 ± 98.1 m/s. To the best of our knowledge, this is the highest combustion speed using a MoO_3 oxidizer reported to date, as observed in **Table 4-1**.

Table 4-1. Several reported data of Al/ MoO_3 combustion wave speed are compared to our measurement result.

Author	MoO3 Dimension	Al NPs	Speed (m/s)	Publisher	Year
Pantoya [25]	Micron	108 nm	19	Propellants, Explosives, Pyrotechnics	2005
Our Data	Micron to tens of microns	80 nm	51.3		
J.A. Puszynski [135]	Micron 1.5 m^2/g in BET	40 m^2/g	80	Powder Tech.	2005
J.A. Puszynski [135]	Nanosheets 76 m^2/g in BET	40 m^2/g	362	Powder Tech.	2005
Pantoya [160]	Nanosheets 42 m^2/g in BET	120 nm	410	Propellants, Explosives, Pyrotechnics	2006
Foley [26]	Nanosheets ~50nm in length	38 nm	680	P. Combustion Institute	2011
S. Son [40]	Nanosheets 30 x 200nm in size 64 m^2/g in BET	80 nm	950	J. of Propulsion and Power	2007
Our Data	Nanosheets (size of 130-600nm and thickness ~1.4-2.8nm)	80 nm	**1730**		

Previous work has measured the reactivity of micron-scale Al/MoO_3 composites, including both pressure and combustion speed measurements. The propagation speed is affected by the thermodynamic state of the products and it is observed that the 1.4 equivalence ratio has the optimum proportion between the gas production and fuel interaction. Son et al. analyzed an Al MoO_3 nanosheet material system with thicker MoO_3 flakes mixed with APS 80 nm Al nanoparticles [40]. Their fastest combustion speed was ~950 m/s and maximum peak pressure of 1.66 MPa. Foley et al. conducted Al/MoO_3 reactivity experiments using Al nanoparticle APS 38 nm and MoO_3 particles ranging in size from ~50 nm to 1 μm long [26]. This work also confirms an optimum

equivalence ratio for Al/MoO_3 of 1.4. The measured combustion speed reached ~680 m/s.

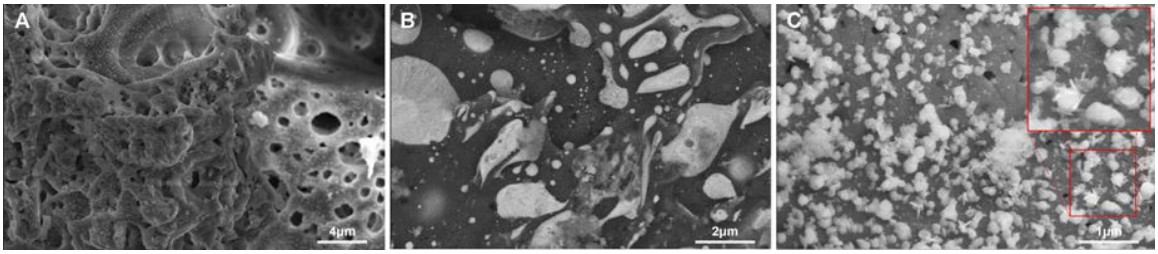

Figure 4-11. SEM micrographs of combusted nanoparticle Al / MoO_3 nanocomposite show varying morphology. (a) Porous regions indicate solidified regions from which reaction gasses escaped during combustion. (b) Resolidified and phase-separated regions of Mo (bright) within an Al (dark) matrix indicate that the material was molten during combustion. Arrows indicate the presence of unreacted particles. Adjacent to fully reacted material, (c) unreacted spherical Al nanoparticles with nanorods are observed, indicating that Al sintering was mitigated at reaction temperatures.

The post-combustion analysis provides insight into the relative temperature of the reaction and the morphological evolution of the reactants during combustion. The combustion product was inspected in SEM by adhering material directly onto carbon tape. SEM images, shown in **Figure 4-11**, indicate that the reaction temperature was sufficient to fully melt the reactants. The products appear phase-separated, as Mo-rich regions appear isolated in an Al-rich matrix. The combusted product was heterogeneous in nature, showing highly porous regions and relatively smooth regions. We propose that the highly porous areas represent regions that were molten during combustion and from which reaction gasses escaped, leaving behind a porous structure after re-solidification. Note that the porous regions do not resemble large particle agglomerates that would be anticipated from a high-temperature sintering process. Backscatter electron imaging facilitated differentiation between material compositions via grayscale contrast, whereby elements having a higher atomic number appear brighter. A typical backscatter electron image is shown in **Figure 4-11**.

Note that relatively bright spheroidal inclusions were surrounded by a relatively dark matrix without an interfacial gap, indicating phase-separated regions of Mo surrounded by Al, as confirmed by EDS in **Figure 4-12**. The intermixing and geometry of the Mo inclusions further indicate that the after-reacted material was molten during combustion, suggesting that the reaction temperature exceeded the melting temperature of Mo (2,896 K) and Al_2O_3 (2,345 K). Similar regions were not observed when observing the post-combustion product of micron-scale MoO_3 powder oxidizer as shown in **Figure 4-12**.

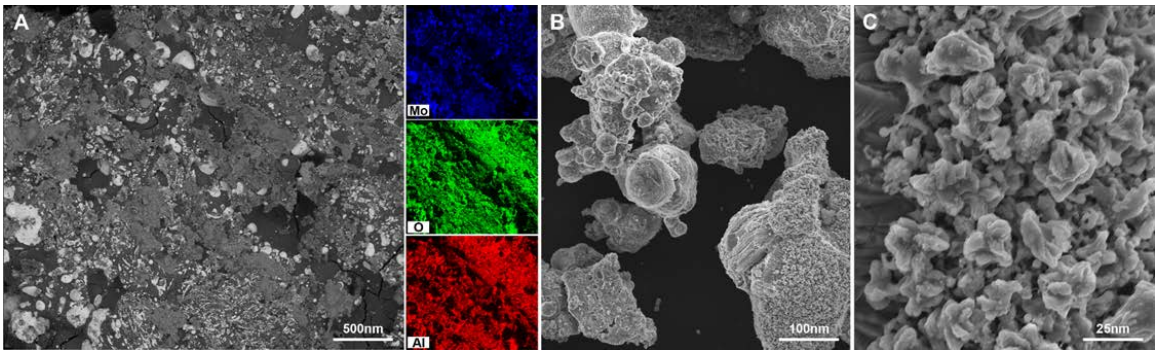

Figure 4-12. (a) Backscattered electron (BSE) SEM micrograph of MoO_3 and Al NPs after combustion in a confined well is presented along with the EDS mapping of area (inset). (b-c) Secondary electron SEM images of the post-combustion product of micron-scale MoO_3 powder oxidizer.

Solid spherical particles were often found near or on solidified reaction products, as indicated by the red box region in **Figure 4-11(c)**. Because of the proximity of these particles to the molten region during the reaction, it may be assumed that these particles were heated to an elevated temperature during the reaction. Surprisingly, these particles are found isolated or in small particle assemblies, indicating that the particles resisted sintering even at high temperatures. Further, the particles are in close proximity and are directly decorated with extended alumina protrusions similar to the particles observed after slow TGA/DSC heating to 1,000 °C. Based on these

observations and the enhanced combustion properties observed for this system, we hypothesize that the Al particles having extended alumina protrusions provide a physical barrier against sintering while allowing a pathway for high-temperature reaction gasses to preheat particles in the vicinity of the reaction zone. Furthermore, because of the elevated melting temperature of Al_2O_3, the protrusions could sustain their morphology even at temperatures at which the Al nanoparticle fuel initiates combustion. These material attributes and mechanisms promote more rapid and more efficient combustion.

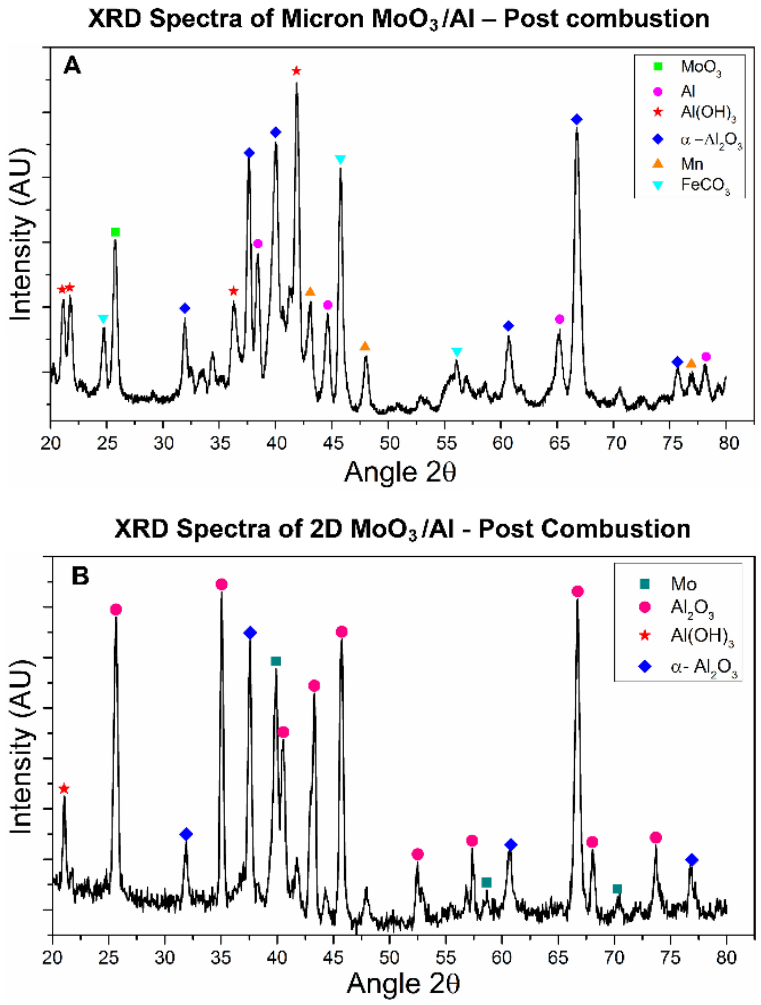

Figure 4-13. XRD result comparison between the combustion products of (a) micron MoO_3/Al and (b) 2D MoO_3/Al.

Finally, separate XRD spectra were obtained from combusted material utilizing exfoliated 2D MoO_3 and microscale MoO_3 powder oxidizers at an equivalence ratio of 1.4. As seen in **Figure 4-13(a)**, the combustion product when using micron-size MoO_3 powder oxidizer shows γ−Al_2O_3, unreacted Al, and unreacted MoO_3 peaks. By contrast, the combustion products produced from 2D MoO_3 exhibits strong peaks α−and γ−Al_2O_3 without unreacted Al or MoO_3, as shown in **Figure 4-13(b)**. Further, Mo peaks are observed when using 2D MoO_3 oxidizer, indicating that MoO_3 was fully reduced in the reaction, consistent with the proposed combustion mechanism. Contaminants such as $FeCO_3$ and Mn in the XRD spectra are thought to originate from the synthesis of MoO_3 powder and are largely removed during the exfoliation and centrifuge processing to form 2D sheets.

4.9 Conclusion

Exfoliated 2D MoO_3 sheets were assembled with Al NPs to form a highly reactive nanoenergetic composite material. The exfoliated MoO_3 sheets provided high surface area and exhibited enhanced intimacy with Al NPs. By providing a larger surface area of interaction and reducing the mass diffusion length between the fuel and oxidizers, nanosheets greatly enhanced the nanoenergetic energy release of the system. Combustion experiments indicate that exfoliating the MoO_3 oxidizer increased the maximum pressure and pressurization rate by a factor of greater than four while retaining an optimal equivalence ratio of 1.4. The observed combustion speed of 1,730 m/s is the fastest-reported value for this material system. Analysis of the combustion products indicates that MoO_3 sheets produced a greater reaction temperature, sufficient to melt the Mo and Al_2O_3, and approaching the adiabatic reaction temperature of 3,253 K. A morphological and chemical transition of the MoO_3 sheets

at elevated temperatures was observed in both slow heating and rapid heating environments. Here, MoO_3 sheets were converted to extended alumina flakes located on the exterior of Al NPs by Al surface diffusion and adsorption onto and within the host MoO_3 sheets. The heat from the reaction acts to displace the host Mo ions from the solid lattice, where they then form reduced Mo particles on the reaction products. The 2D nature of exfoliated MoO_3 oxidizer sheets facilitates complete and rapid reaction via the proposed mechanism, whereas complete combustion of MoO_3 micron size powder cannot proceed along a similar path. These results stress the importance of nanoscale material geometry to increase reactive surface area and reduced diffusion lengths within nanoenergetic materials and the importance of material self-assembly to ensure homogeneous distribution of reactants.

CHAPTER 5 : PLASMONIC ENHANCED REACTION OF ALUMINUM NANOPARTICLES EMBEDDED IN POLYMERS

5.1 Introduction

The objective of this study was to examine the optical coupling effect of plasmonic silver grating microchips using various polymer systems. Silver-coated polymethylsilsesquioxane (PMSSQ) gratings with protective alumina coating (10 nm) were fabricated using the previously mentioned microcontact lithography stamping process [68]. Aluminum nanoparticles (Al NPs) mixed with different types of polymer films were deposited on the grating microchip. A surface plasmon resonance (SPR) study used a variable-angle spectroscopic ellipsometer to examine the light coupling at the grating and polymer interfaces. The coupling is sensitive to the refractive index of the materials. The coupling parameters, including the refractive index, can further be identified using a dispersion curve of the grating illuminated with light from the front- and backside of the grating. Interfaces from the front side of the grating consist of the medium interfaces, the polymer, silver film, and PMSSQ. Whereas interfaces from the backside of the grating consist of the glass substrate, PMSSQ, silver, and the polymer. With each material having specific optical properties, the goal is to obtain the matching condition at either side of the grating indicated by the symmetrical dispersion curve. The absorption wavelength of varying nanoparticle sizes is studied to determine the optimum coupling of the Al NPs to the grating system. Subsequently, the optimum laser wavelength range can be selected as photothermal heating source. Enhancement of the coupled incidence light in the form of a laser source that constructively interferes with several resonance peaks could ultimately generate the best coupling for the system, providing localized heating that leads to Al NPs ignition.

We report a proposed reaction mechanism of polymer and Al NPs systems. A standard laboratory inverted microscope was modified for testing apparatus capable of an in-situ and before-and-after investigation to study the reaction mechanism. Aluminum was used as fuel, whereas fluorinated polymers, for instance, are Teflon, and THV, as oxidizers. Additionally, Nitrocellulose is used as binder and particularly attractive for use as a nanothermite binder because it decomposes into gaseous products during combustion [161]. These polymers have been previously investigated in their optical properties using an ellipsometer. The materials, consisting of fuel aluminum nanoparticles embedded in a polymer oxidizer, are heated by a pulsed laser. A microscope's tunable laser heating and imaging setup are designed for in-situ photothermal heating on polymer/Al NPs systems. Localized reactions involving clusters of Al NPs are captured using high-resolution and high-speed color cameras. We can monitor the nanoparticles' movement and morphology changes during laser photothermal heating based on microscopic imaging. In addition, two-color pyrometry is used to estimate the reaction temperature.

5.2 Preparation of Al-Polymer Sample

Aluminum nanoparticles (Al NPs) with 120 nm average diameter and an alumina shell thickness of 3.7 nm were purchased and used as received from Novacentrix (Austin, TX, USA). THV 220A is a fluoropolymer purchased from 3M company (St. Paul, MN, USA); THV is composed of tetrafluoroethylene, hexafluoropropylene, and vinylidene fluoride. The glass transition temperature (T_G) of THV 220A is 26 °C, and the melting point (T_M) of THV 220A is 120 °C. Nitrocellulose (NC) NC flakes (<12.6%nitrogen content) were obtained from DowWolff Cellulosics (Bomlitz, Germany). Teflon^{AF} 1600 were purchased and used as received from Dupont. Typical

molding temperatures for Teflon® AF 1600 range from 240 to 275°C (464 to 527°F), which begins to decompose above 360°C (680°F). FluroSylTM FSM-660-4-52 (FSM) was purchased from Cytonix Corporation (Deltsville, MD). FSM-660-4-52 is a 4% solution of a fluoroaliphatic triethoxy silane in a fluorinated solvent providing low surface energy to oxide surfaces and good adhesion for fluoropolymer. FSM monolayer provides good adhesion of fluoropolymers on oxide surfaces via salinization. The FSM will mainly be used in the sample preparation before the coating Teflon on the sample. FSM was spin-coated first on grating substrate which was precleaned by acetone-methanol-DI water (AMD) method. FSM monolayer on the treated surface was left cured for 24 hours in ambient condition at room temperature.

Each polymer sample has a different dispersing solvent without changing its property physically and chemically. Al NPs and THV were dispersed in acetone, NC was dispersed in Methyl Ethyl Ketone (MEK), and Teflon was dispersed in FC-75. Al and the polymers have starting concentrations of 0.5 mg/ml and 55.56 mg/ml, respectively. Samples were individually dissolved and sonicated for 3 hours. The final concentration of Al in each polymer is 0.1% after mixing each of the polymer systems following an hour of additional sonication. Then, the mixture was immediately deposited on an FSM-treated 40 nm silver gratings. A thick film can be deposited by drop-casting 0.5 mL of the mixture on the grating substrate, followed by an oven drying process. The thick film of Al/polymer has a thickness of around 10 μm.

5.3 Thermal Analysis of Al/Polymer nanoenergetic systems

Chemical reaction pathways can be observed by measuring the phase transition and reaction temperatures of the polymer/Al NPs. Using differential scanning calorimetry (DSC) and thermogravimetry analysis (TGA), we can correlate the

possible reaction for each polymer/Al NPs system. DSC/TGA of THV indicates the melting temperature shown by the endothermic peak starts at 120°C in **Figure 5-1(a)**. An endothermic peak at 507°C with an onset temperature of 463°C represents the decomposition of THV into gaseous products. Fluorine-contained gaseous species such as C_2F_2 and C_2F_6, are commonly produced from THV. This reactive species can react and remove the alumina shell, then subsequently release the Al core content. As demonstrated by the onset temperature in Al/THV shown in **Figure 5-1(d)**, the reaction can start as early as 476°C. The exothermic peak is located around 534°C. Since the reaction is in the decomposition temperature range, the potential reaction mechanism is more likely to occur in the gas phase than the liquid phase.

Figure 5-1(b) shows the neat Teflon sample with no endothermic peak, indicating that the melting may occur. A slope change starts at 250°C, indicating Teflon's glass transition point. An endothermic peak at 513°C with an onset temperature of 485°C represents the decomposition/evaporation of Teflon, consistent with many observed [162]. Al/Teflon, in **Figure 5-1(e)**, experiences two exothermic peaks at 462°C and 531°C, with the first onset temperature at 438°C, where the latter has shown a greater heat release. Based on reported literature, the exothermic peak at 550°C corresponds to the AlF_3 transition from α to β phase [162]. **Figure 5-1 (c, f)** shows that the onset decomposition of NC is at around 197°C and the thermal decomposition is in the proximity mentioned in the literature [113]. The energy release of the Al/THV was 1302 J/g, Al/NC was 415 J/g, and Al/Teflon was 405 J/g. In all samples containing the fuel, the endothermic peaks occurred at approximately 663°C, indicating the melting of the unreacted Al NPs. It shows that most of the Al NPs reacted to the polymers are well below the melting temperature of aluminum.

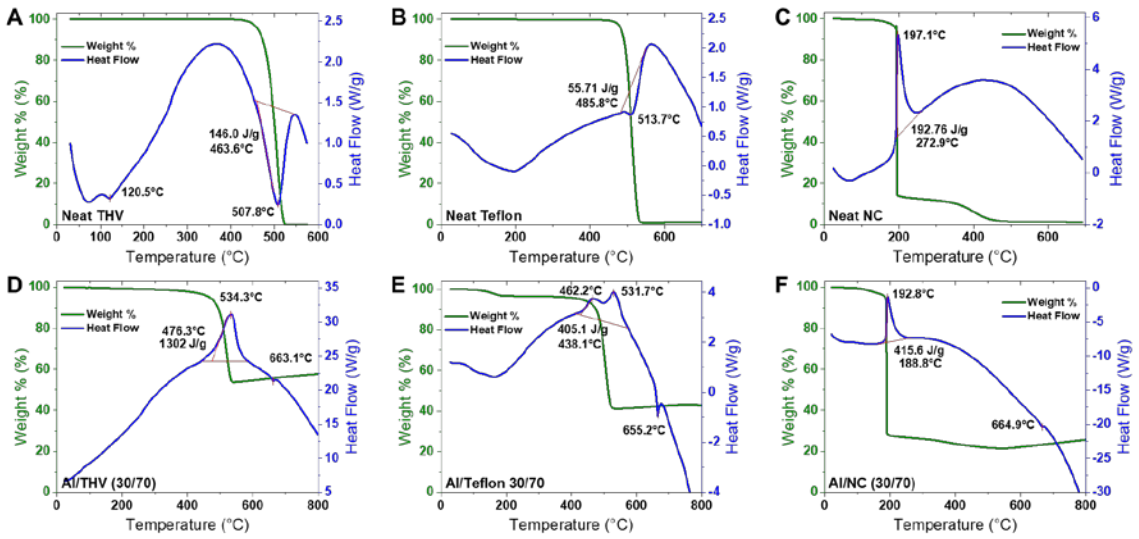

Figure 5-1. Thermal characterization of aluminum polymer samples. Differential scanning calorimetry (DSC) and thermogravimetry analysis (TGA) of the precursor polymers (a) THV, (b) Teflon, (c) Nitrocellulose, and the aluminum polymer samples (d) Al/THV, (e) Al/Teflon, and (f) Al/Nitrocellulose.

5.4 Effect of Refractive Index

Polymer/Al NPs films were deposited on grating microchips and studied from the top side of the grating using a diode laser as an ignition source. This setup only allowed both laser source and imaging equipment to be from the top side of the grating. Previously, the experiment setup incorporated a 40x objective imaging lens and a laser source at an angle of 30° or greater. This setup provided a limitation as a higher magnification, e.g., 100x, is also more desirable to improve our observation of the reaction at microscale resolution. However, using a 100x objective lens in our experiment setup raises several challenges. For instance, the relatively small working distance (~300 μm) eliminates the possibility of incorporating a laser source from the same side of imaging equipment. Therefore, the design of the experiment should incorporate the imaging equipment from the top side of the grating (frontside measurement), the laser source equipment is placed from the bottom side of the

grating, or vice versa. The illustration of the experiment design is shown in **Figure 5-2**. For these reasons, we attempt to design a transparent grating microchip that can be imaged from either side of the grating. This design utilized a 40nm thin layer of silver (Ag) and alumina layer deposition on a thin 200μm glass substrate, making this grating semitransparent. With this new design of transparent grating microchips, we can now image the particles from either side of the grating. The design further enables the observation of the reaction in each polymer system with Al NPs.

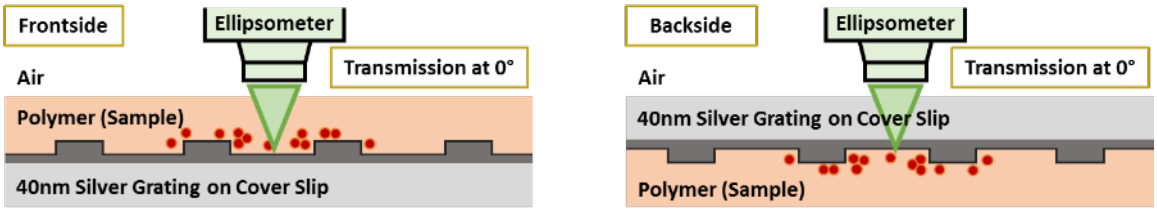

Figure 5-2. Experiment design incorporates imaging and laser source equipment from each grating side. Frontside measurement is used by having imaging equipment from the top side of the grating, whereas backside measurement is used by having imaging equipment from the bottom side of the grating.

This study aims to use an ellipsometer to measure the optical coupling effect of the polymer at some specific range of wavelengths. The polymer's transmission and reflection data on the plasmonic grating microchip generate a dispersion curve to show the SPR modes at different interfaces. In this experiment, polymers with varying refractive index and optical properties are Teflon, THV, and NC. In **Figure 5-3**, ellipsometer data in transmission and reflection mode from 0° to 30° of incidence angle was translated into dispersion relation curves. The resonance wavelength is indicated by the locations of the dip in reflection measurement at is summarized in **Figure 5-3**. There are three dominant peaks in each polymer measurement, namely the first- and second-order SPR modes of Ag/polymer in addition to the SPR mode of PMSSQ/Ag.

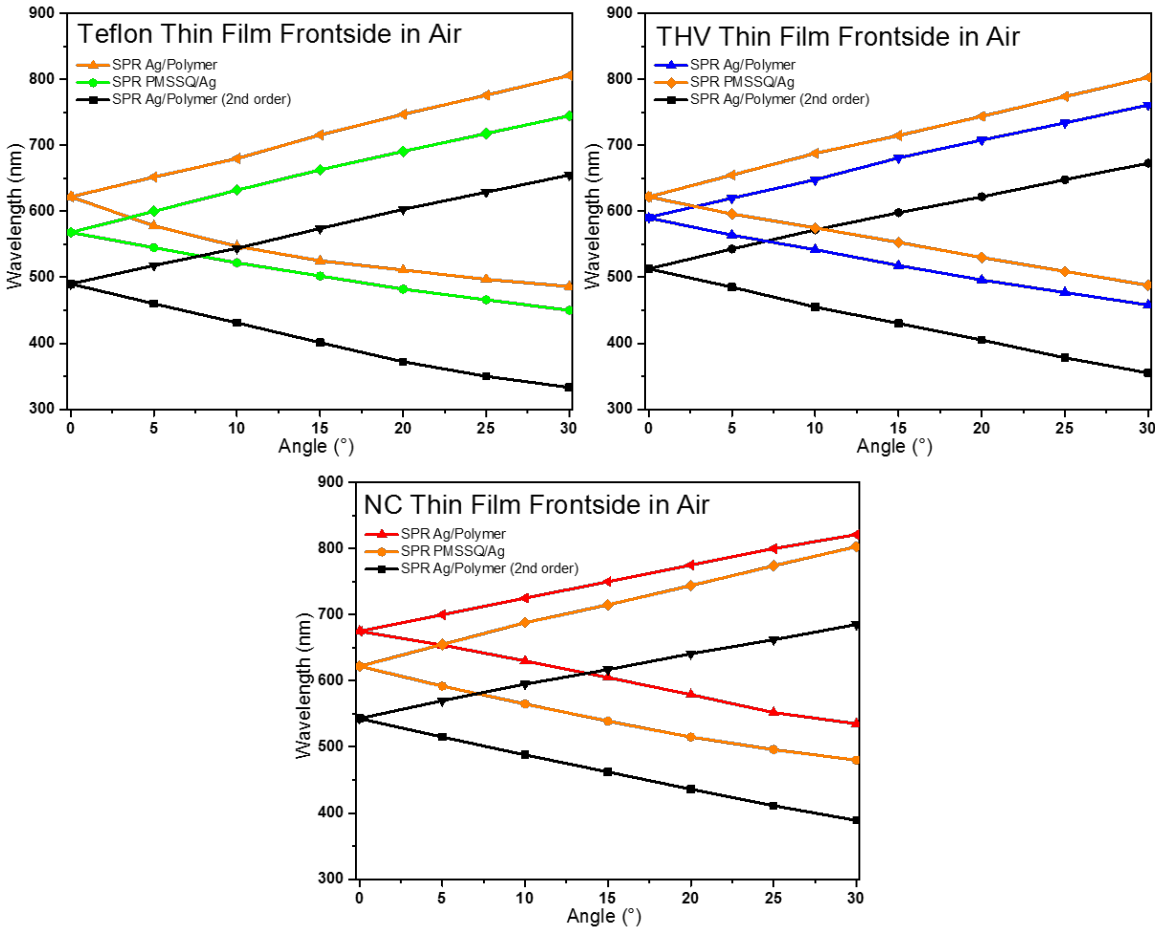

Figure 5-3. Dispersion curve of different polymer systems: Teflon, THV, and NC deposited on a plasmonic grating microchip. Dispersion curves translate the wavelength of each dominant peak as a function of the angle of measurement from the transmission and reflection data of the ellipsometer

The advantage of having a perfect match of the grating substrate and polymer film affects both the laser-induced heating and the imaging resolution in the combustion experiment. Dispersion curves of the SPR mode of PMSSQ/Ag and the first order SPR mode of Ag/polymer are summarized in Figure 53. The indicated SPR modes show each peak's intensity in transmission mode at a 0° incidence angle was also shown. The peak of the SPR mode of PMSSQ/Ag is located at 625nm. Therefore, the optimum coupling occurs when the coupling of the polymer media and the grating is located closely.

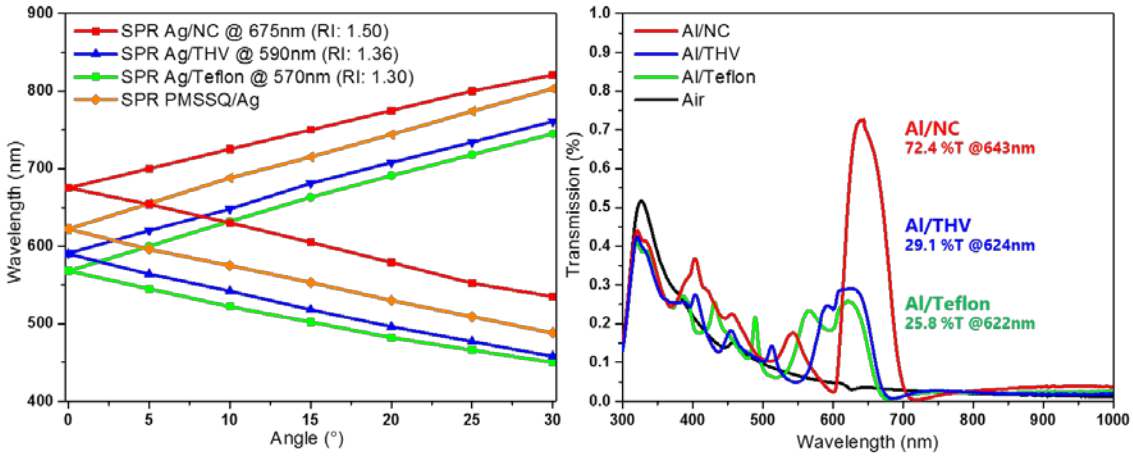

Figure 5-4. Dispersion relation curve of Al/Polymer films frontside in an air medium (a) and ellipsometer measurement in transmission mode (b) has shown the effect of different polymers due to the refractive index.

The combustion experiment design of the polymer/aluminum nanoparticle system employed a laser source at a 0° angle of incidence. In addition, the dispersion relation curve provided the SPR coupling modes for all angles and wavelengths. Therefore, the transmission scan is a helpful tool to determine the optical transmissivity at a 0° angle of incidence. **Figure 5-4** shows that NC matches best among different polymers due to its SPR matching the SPR of PMSSQ/Ag and having 72.4% transmission at 0° angle of incidence with a peak at 643nm.

Next, the dispersion curve also shows that THV can provide a good coupling due to the adjacent SPR locations of the PMSSQ/Ag and Ag/THV. However, the transmission data at a 0° angle of incidence is much lower than NC, with THV having only 29.4% transmission with a peak at 624nm. A similar condition is also seen in the Teflon system, where the SPR of PMSSQ/Ag and Ag/Teflon were further apart.

5.5 Development of Laser Heating System

The combustion dynamics of reactive materials were studied using laser-ignition heating with high-speed and high-resolution imaging. This section reports the recent

development of in-situ characterization using an inverted optical microscope. A pulsed laser setup is incorporated to initiate localized photothermal ignition, as shown in **Figure 5-5**. The objective is to observe the energetic material reaction mechanism of the Al/polymer.

Furthermore, the inverted microscope enables laser illumination from the bottom side of a semi-transparent grating microchip with the feasibility of turning the laser to any angle of interest. Most importantly, it allows high-resolution in situ imaging under 100x objective, opening the capability of in situ ignition and imaging of single nanoparticle combustion under a conventional microscope. This setup facilitates sub-wavelength resolution while allowing a field of view of hundreds of microns. Our previous work indicates that the plasmonic grating microchip can achieve 60nm spatial resolution using localization microscopy for super-resolution imaging. [105]

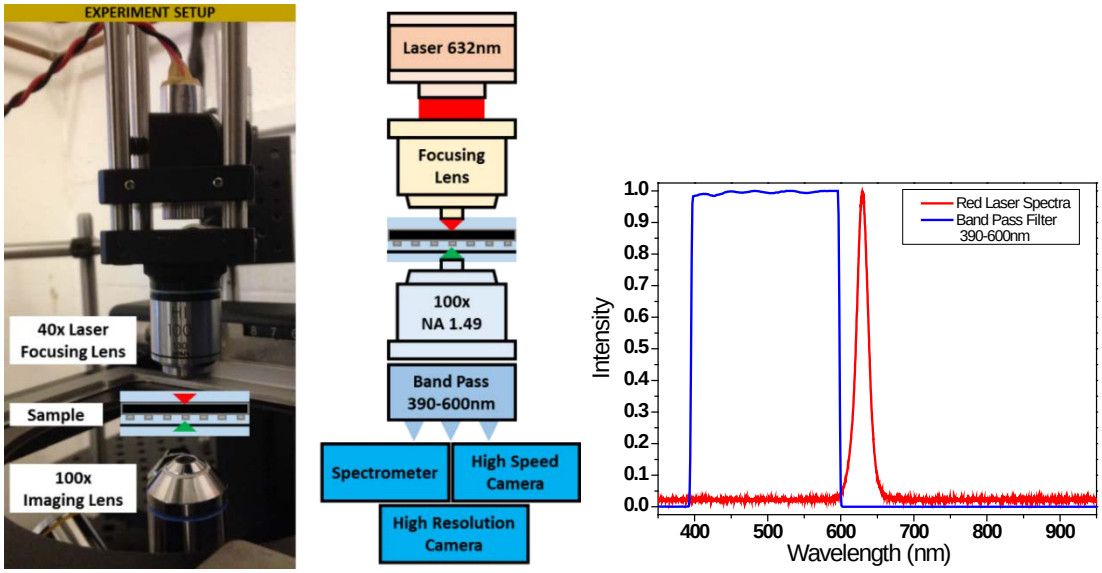

Figure 5-5. Setup (left) and schematics illustration (middle) of the laser-heating experiment incorporates a red laser and 100x high-resolution imaging. (Right) the incident laser, plotted in red, is blocked using a bandpass filter of 390-600 nm indicated in the blue curve. High-speed image acquisition only captures the transmitted region.

A new diagnostic methodology was developed using a plasmonic grating microchip incorporated in an inverted microscope shown in **Figure 5-5**. One is that the laser heating in this system can be illuminated from both sides of the grating. A pulsed laser system illuminated one side of the grating for localized photothermal heating, whereas a high-resolution imaging system was utilized on the other side of the grating. Further, having laser-ignition and imaging apparatus on two different sides of the grating has enabled a more comprehensive range of laser angle tenability. The effects of different Al/polymer systems were studied to demonstrate the role of refractive index matching in the light coupling leading to photothermal ignition. In-situ images using high-speed and high-resolution imaging recorded instantaneous phenomena, including particle movements, polymer phase change, and flame generation and propagation during laser exposure.

Moreover, for ex-situ measurements, 100x high-resolution optical scattering images of polymer/aluminum nanoparticles before and after the laser exposure were investigated using the polarized light microscopy technique. In addition, to enable particle counting, this technique can determine whether a reaction occurred.

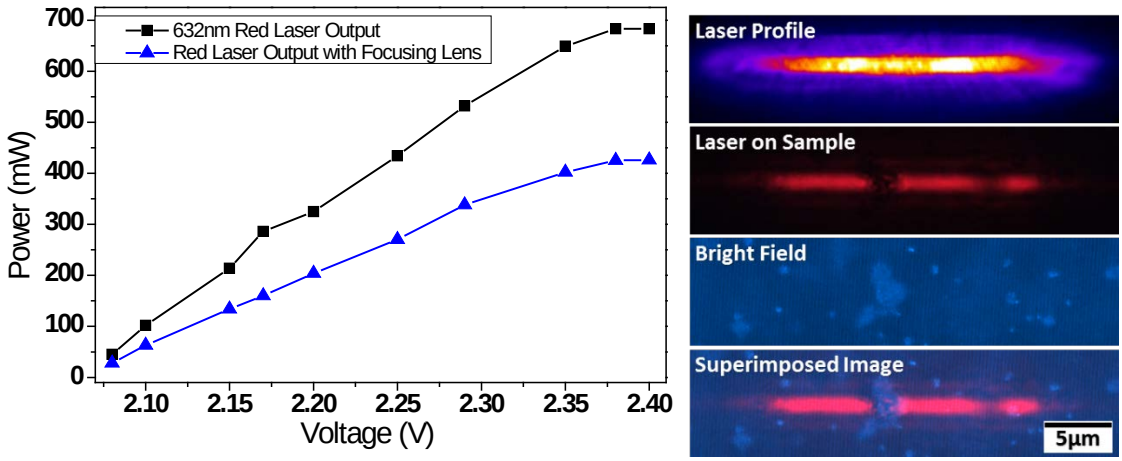

Figure 5-6. Power delivered of the laser heating is reduced from the original power of 700mW to 425mW after it is focused using a 40x objectives lens (left). However, the laser beam size

is reduced from the millimeter range to only 20 μm using the focusing lens. The image of the laser profile indicates the laser alignment during the combustion experiment.

Laser focusing is essential in delivering power to the aluminum nanoparticle target. A power meter is used to measure the initial laser power and the power after the focusing lens, as plotted in **Figure 5-6**. The laser power initially has a maximum of 700 mW, whereas the maximum power was only 425mW after the laser-focusing lens. However, having a focused laser beam was crucial to maximize the delivered energy flux to the Al NPs. The laser-focusing lens successfully reduced the size of the laser beam from a millimeter range to only 20 μm, as shown in **Figure 5-6**. Before exposing the laser for the combustion experiment, the laser was correctly aligned to the desired aluminum nanoparticles target.

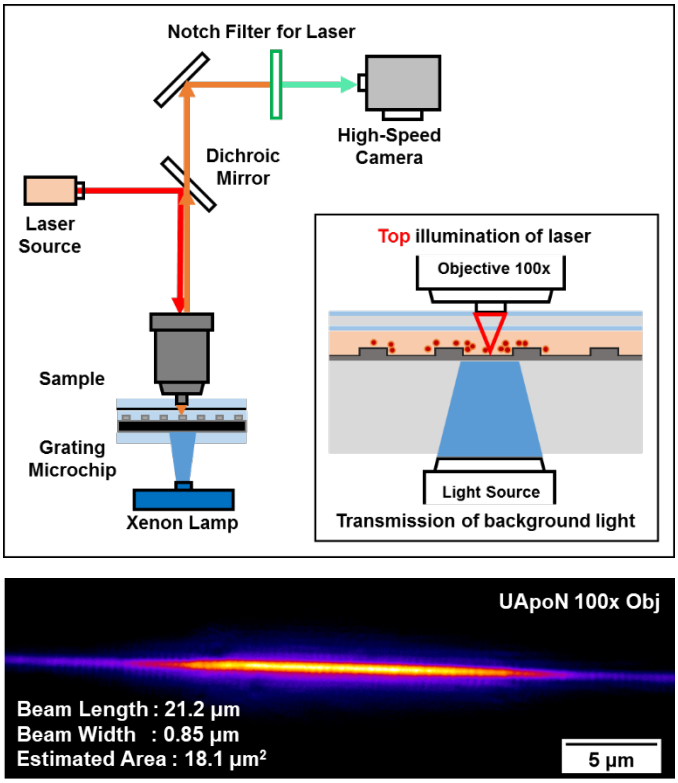

Figure 5-7. Laser ignition experiment schematics. The experiment setup, including a laser source and high-speed color camera, is incorporated into an inverted microscope. A high-quality TIRF 100x oil objective is used as a laser focusing and imaging lens. The laser source

is limited by a bandpass filter (100%T at 625-645nm), while the emission filter uses a notch filter (0%T at 620-650nm). Inset illustrates the Al NPs suspended within the polymer on the grating surface.

Our recent development incorporates a high-quality UApoN 100x oil objective for laser-focusing and imaging purposes. Although the beam power is reduced, the beam profile is highly focused and uniform due to the apochromatic aberration correction from the lens. The power density [W/cm^2] is measured by the power delivered over the beam area—the average power density of 3.1 x 10^4 W/cm^2. Since the setup gives a relatively uniform laser beam, it is safe to assume that the power density is the same throughout the entire beam. However, the bottom illumination uses fewer lenses resulting in the beam having multiple nodes. The laser fluence [J/cm^2] is measured by the power density and the laser irradiation time. Assuming the laser irradiation time is 1 ms, the laser fluence is 31.3 J/cm^2. The recent development also includes some improvements in the laser triggering, allowing the laser irradiation time to be in the range of tens of microseconds for future applications.

Table 5-1. Power profile of the red laser characterized and installed in the inverted microscope

Obj. Lens	Power	Time Pulse	Beam Area	Pulse Energy	Power Density	Fluence
x	mW	ms	μm^2	μJ	W/cm^2	J/cm^2
UApoN 100x	5.66	1	18.1	5.66	31,270	31

5.6 Imaging Methodology – Thin vs Thick Films

The objective of this section is to observe the aluminum nanoparticles embedded in polymer and coated on a plasmonic grating microchip. A semi-transparent

plasmonic grating microchip enhances the imaging and electric field coupling of the Al/polymer systems. Samples were composite thin films of 120 nm Al NPs suspended in different polymer systems: Teflon, THV, and NC. The mixing procedure to ensure uniform films was described in detail earlier. In short, Al NPs were suspended in a solvent that also dissolves the corresponding polymer. Each Al NPs and polymer were separately weighed and sonicated to ensure well-dispersed suspension. After mixing, the final concentration of the mixture was as low as 0.1 wt% ratios of Al to the polymer. Then, the mixture is spin-coated to make a thin film (500 nm) or drop cast to make a thick film (10 μm) on a grating microchip.

High-resolution imaging evaluated the number of particles before and after the reaction in the bright field and scattering modes. In optical microscopy, bright field mode uses the source light either being transmitted or reflected, giving contrast by the reduced light intensity at the denser area. Bright-field optical images are obtained in 100x oil to show the well-distributed Al NPs sitting on the grating. Bright-field imaging can quickly identify and provide insight into the object's presence and location shown by the darker region. Bright-field image in **Figure 5-8** (left) shows that Al NPs will appear dark, whereas the lighter areas represent the neat polymer.

In contrast, scattering imaging uses the idea of dark field microscopy, where the direct light is blocked from passing through the sample. Instead of using a hollow cone to block the initial light, the imaging setup uses polarization-based scattering by utilizing a polarizer and a polarizer's analyzer.

The scattering image in **Figure 5-8** (right) shows the metallic content of Al NPs that intensely scatter light and have a higher color intensity. Due to the distinct contrast of the Al NPs to the grating substrate, the approximate number of particles can be

estimated by adjusting the image focal plane. This high-resolution imaging method is significant in further experiments since it can determine the particle's presence and the number of Al NPs in a cluster.

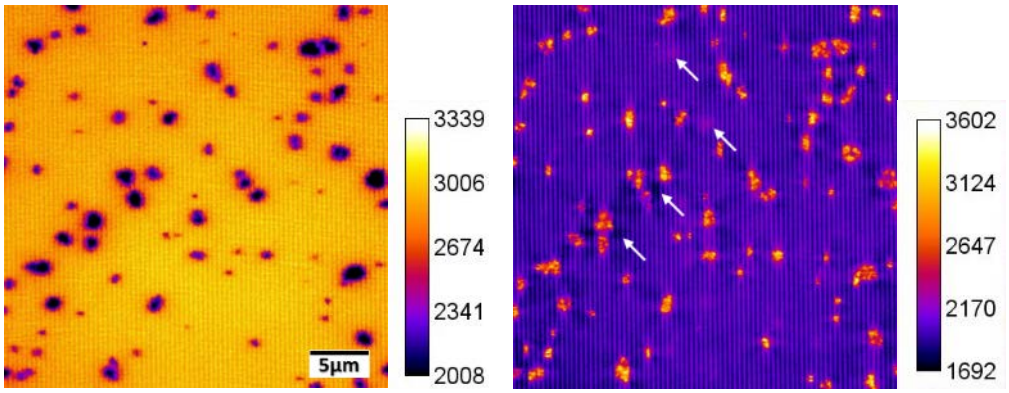

Figure 5-8. Top-illumination high-resolution imaging was taken in (left) bright field and (right) scattering modes of 120 nm Al NP embedded in THV thin film on the semi-transparent plasmonic grating microchip.

A thin film of aluminum nanoparticles embedded in THV is shown in **Figure 5-8**. High-resolution imaging using 100x immersion oil provides a depth of view that captures both the grating and most of the Al NPs at the same focal plane. The matching and coupling of the field discussed in the earlier section have resulted in a clear and good contrast between the particles and grating with several individual particles in their presence. Some particles sit further away from the grating. Hence some areas appear darker or brighter due to particles in the different focal planes, shown by the white arrows.

A thick film of aluminum nanoparticles embedded in THV is shown in **Figure 5-9**. High-resolution imaging using 100x immersion oil provides a depth of view that captures both the grating and the aluminum nanoparticles close to the grating. Compared to the thin film, the thick film has many more particles on different focal

planes. The focal plane difference in the thick film shows that many particles are not in focus, creating shadows in both bright-field and scattering (pointed by the arrows).

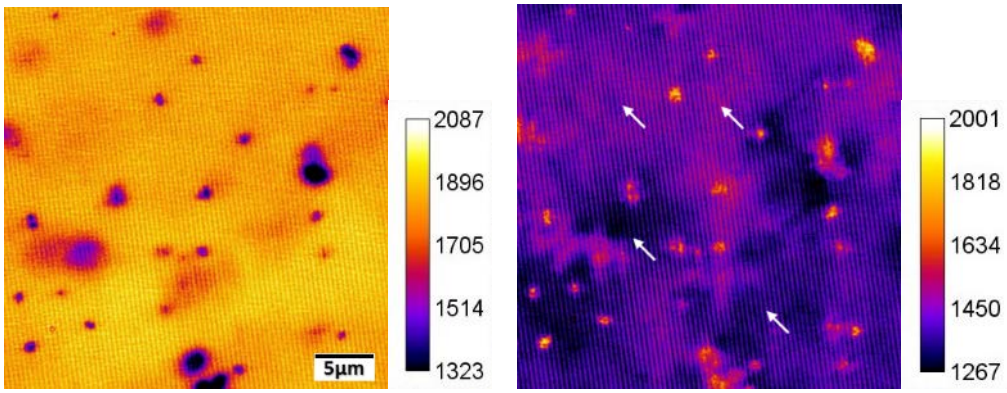

Figure 5-9. High-resolution imaging was taken in (left) bright field and (right) scattering modes of 120 nm Al NP embedded in THV thick film on the plasmonic grating microchip.

5.7 Two-Color Optical Pyrometry

This section presents an imaging-based instrumentation system calibration for temperature reconstruction of a reaction flame. Image processing techniques and two-color radiation pyrometry were utilized to generate the flame temperature distribution based on the ratio of the color camera channels. The pyrometry has been optimized for high-temperature operation and discussed in previous work [50]. A tungsten lamp was chosen and calibrated in the inverted microscope system used as a standard temperature, proven reliable and accurate [163,164]. Constant driving voltage was used ahead of the constant current source due to the ability for faster stabilization of the lamp temperature. The lamp spectrum was calibrated at incrementing voltage, and system response calibration was done to yield absolute irradiance. Then, the spectrum was fitted to a tungsten emission model to get the fitted model shown in **Figure 5-10**.

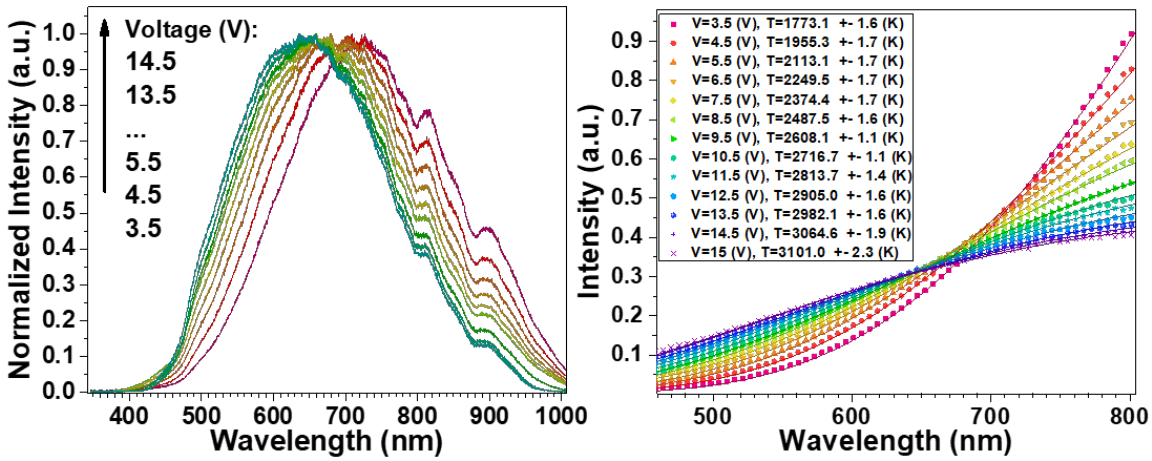

Figure 5-10. System response calibration of the tungsten light source measured in temperature as a function of driving voltage source

The calibration of the tungsten lamp in the system has enabled obtaining the intensity per millisecond vs. the source voltage for green and red channels shown in **Figure 5-11**. The fitted temperature calibration can be used directly for the flame reconstruction of temperature map in a blackbody system [50].

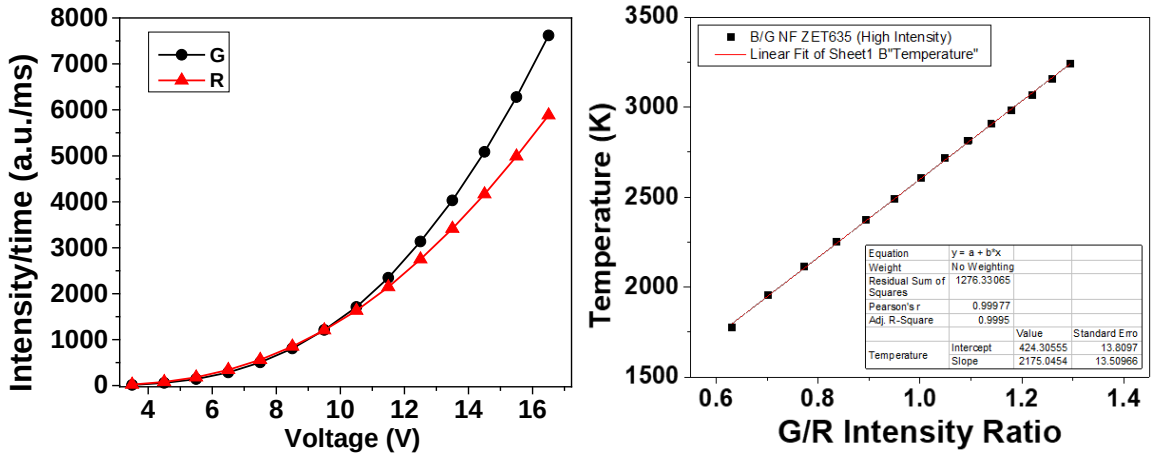

Figure 5-11. Intensity per time at a different working voltage and temperature vs. G/R channels gray intensity ratio of our calibrated system.

The linear fit of the curve in **Figure 5-11** can be expressed as follow:

$$T_{G/R} = 2175.05 * R_{G/R} + 424.30$$

5.8 Laser Ignited Combustion

The effects of different polymer/aluminum nanoparticles systems were studied to demonstrate the role of aluminum polymer chemical properties and the medium refractive index matching of the coupled light leading to photothermal ignition. A single-pulse 632 nm red laser system was illuminated from bottom side of the grating for localized photothermal heating. At the same time, a high-resolution imaging system was utilized on the top side of the grating. In-situ images using a high-speed camera recorded any reaction phenomena during the laser exposure, including particle movements, polymer phase change, and flame generation and propagation. Moreover, the polarization-based scattering technique captured Al/polymer before and after the laser irradiation.

Photothermal ignition of Al/polymer sample was recorded in a high-speed video to evaluate their reaction mechanism. **Figure 5-12** shows some video snapshots representing the typical reaction when the samples were excited by the 632nm laser. The image brightness was increased by 10 times to assist the visual observation. The contrast enhancement is vital to observe any change in polymer form or the presence of the flame.

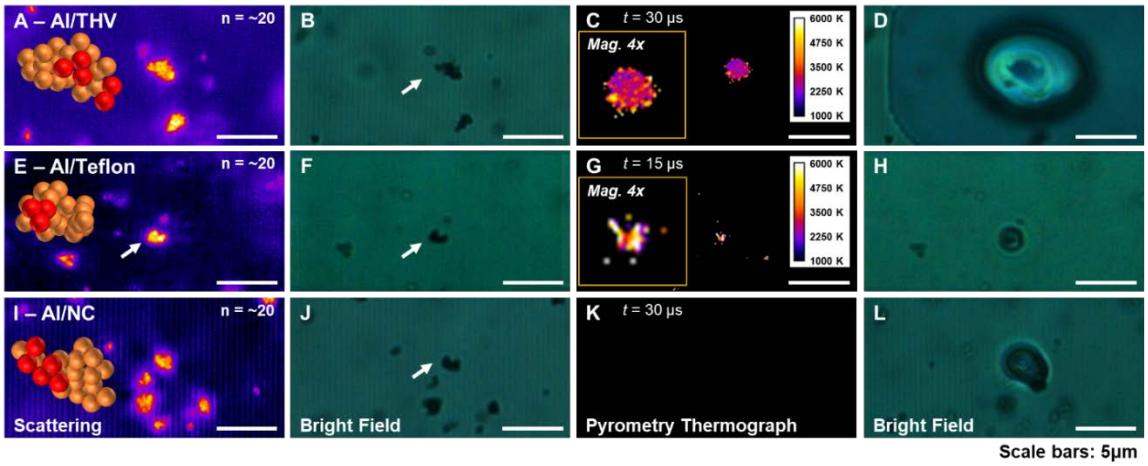

Figure 5-12. Laser-ignited combustion of Al/THV, Al/Teflon, and Al/NC. (a) Scattering image showing a small cluster of ~ 20 Al NPs embedded in the THV polymer film. Al NPs highlighted in red are at the topmost location relative to the cluster. This target cluster is laser-ignited with an excitation time of 1 ms and laser fluence of 31.3 J/cm^2. (b and d) Bright-field images showing the target cluster before and after the laser-ignited reaction. The flame captured (c) is reconstructed in the pyrometry thermograph. Scale bars are 5 µm in all images. The image size is 256 x 128 pixels, while the sampling rate is 60000 fps with an exposure time of 16.5 µs. A similar configuration of experiment methods was applied to (e-h) Al/Teflon and (i-l) Al/NC.

A summary of a typical reaction in all Al/polymer samples is shown in **Figure 5-12**. Several imaging techniques were used to gather information about the combustion event, including the before and after the reaction. Scattering images of the Al NPs suspended in the polymer film provide a precise relative location of the Al NPs regarding the grating plane, which can be illustrated as shown in **Figure 5-12(a)**. In addition, the scattering properties of Al NPs allow the determination of Al NPs whether it is entirely, partially, or unreacted. Reacted particles appear dark due to the product, which absorbs light to indicate a complete reaction. If the Al NPs were partially reacted, the product still slightly scatters light after the reaction occurred. The low scattering light may come from the unreacted metallic content. The Al NPs were unreacted when they scattered light intensely.

Al/THV. Laser heating of cluster consisting of 120-nm Al NPs was investigated using a single 635 nm red laser irradiation. The 1-ms pulse with a total energy of 5.66 μJ at the target cluster created a reacting region over 10 μm away from the center of a 3 μm size cluster. The captured reaction flame was reconstructed using the two-color pyrometry described previously. The thermograph in **Figure 5-12** has shown that most of the flame temperature distribution is within the range of 3000-4000 K, which is well-matched to other reported. [50] This polymer reaction to Al NPs created post reacted region forming a micro bubble structure.

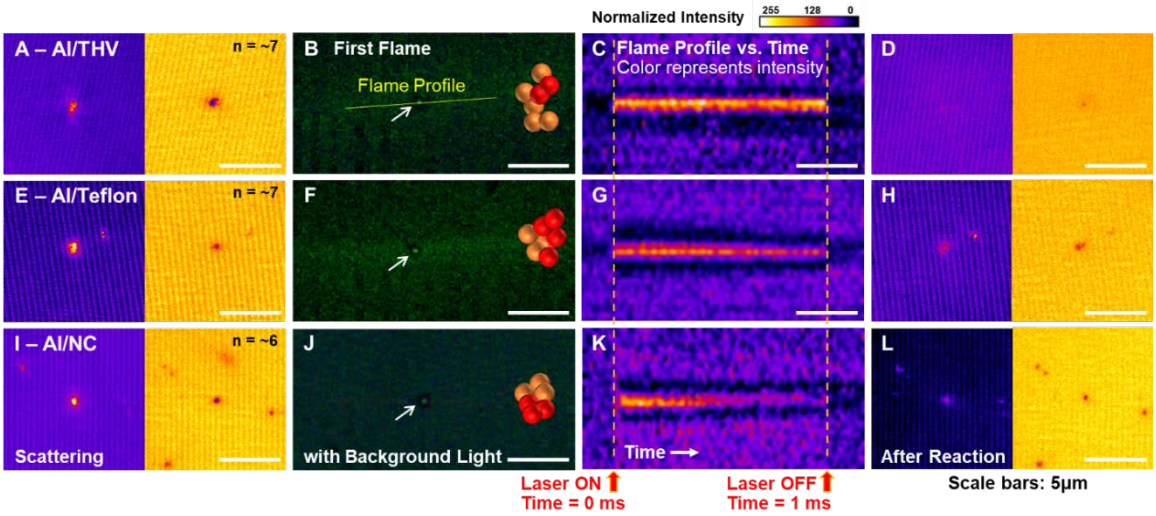

Figure 5-13. Laser-ignited combustion of Al/THV, Al/Teflon, and Al/NC Thin Film. (a) Scattering and bright-field images showed a cluster of 6 Al NPs. Al NPs highlighted in red are at the topmost location relative to the cluster. This target cluster is laser-ignited with an excitation time of 1 ms and laser fluence of 31.3 J/cm^2. (b) Bright-field images showing the target cluster before and after the laser-ignited reaction. The flame captured (c) is reconstructed in the cross-sectional X-axis vs. time graph to see the flame behavior in a thin film. Scale bars are 5 μm in all images. The image size is 256x128 px, while the sampling rate is 60000fps with an exposure time of 16.5 μs. A similar configuration was applied to (e-h) Al/Teflon and (i-l) Al/NC.

Al/Teflon. Teflon chemically contains more fluorine than THV and can be beneficial when reacting to Al NPs. DSC/TGA shows the glass transition temperature of Teflon is higher than the THV melting point. Using a similar laser configuration to

the Al/THV experiment, the 1-ms pulse with a total energy of 5.66 μJ was used to ignite the target cluster. The photothermal heating seemed to initially ignite the topmost particle relative to the cluster, as shown in **Figure 5-13 (f)**. The red-marked Al NPs indicate their initial position that preceded the location of the reaction flame. In addition, scattering imaging shows that some NPs clusters are seen completely reacted while other tests show Al NPs are partially reacted. The partial reaction occurs when the Al/Teflon reaction is rapid, and there is not enough energy to combust the neighboring NPs completely.

Figure 5-13 (c, g) demonstrates the fast nature of the Al/Teflon reaction flame, which does not persist in a way Al/THV does. Many reported that the reaction of Al/Teflon is rapid and has a higher maximum temperature [165,166]. Dana Dlott reported that the initiated Teflon reacts with Al_2O_3 as the first regime initiation process in which the time scale proceeds any thermal conduction event [166]. Another possible pathway is the diffusion of Teflon fragments through the oxide of Al NPs, which could enhance the reaction. Once initiated, Teflon becomes unstable at a temperature near 350 C, leading to the formation of small reactive fluorocarbon fragments capable of reacting with and consuming the alumina shell [162]. The chemical breakdown of the oxide layer by Teflon fragments could also enhance the reaction due to fluorination of the alumina shell. This reaction starts as early as 400 °C to form alumino-fluoro complexes (β-AlF_3), followed by the phase transition from β to α at 550 °C [167]. Once the heat is persisted, a further reaction can also be accelerated by the melt dispersion mechanism where cracking of the oxide shell occurs by Al thermal expansion [168]. However, the mechanism evaluated above may differ from our system because our initiating photothermal heating power is insufficient for the melt dispersion

requirements. Therefore, the material's chemistry occurs during a reaction, while the effect of media matching leads to enhanced photothermal heating from our plasmonic grating.

Al/NC. Nitrocellulose was chosen since it serves as both a binder and an energetic source, although it is considered a mild oxidizer [169]. The low decomposition temperature of NC could significantly increase its reactivity and decrease the ignition delay. Furthermore, based on our ellipsometry data, NC has a better refractive index matching the grating substrate and oil than THV and Teflon. We could not capture any reaction flame when using a similar laser configuration, the 1-ms pulse with a total energy of 5.66 μJ. However, the reaction was still observed and indicated by the reacted region seen before and after images. The chemical structure of nitrocellulose might be why the flame was not captured. While THV and Teflon contain fluorine, NC only releases species of hot gasses that may react to Al NPs, i.e., formic acid, hot gases of NO_2, CO_2, CO, NO, and CH_2O_2 [170].

5.9 Conclusion

There is much room for improvement in the in-situ combustion experiment setup in the inverted microscope. A quantitative study of the reaction using the high-speed video and high-resolution camera was conducted to examine the ignition, phase change, and products and the calibration of the flame temperature. The qualitative study, including the physical and chemical change of the Al/polymer systems, was incorporated. Furthermore, having the surface plasmonic resonance (SPR) shown in the ellipsometer work in the earlier section, in-situ backside imaging of combustion will be tested in the inverted microscope. In addition to 446 nm blue and 808 nm infrared lasers, future works may also investigate other laser wavelengths to study the

plasmonic effect for both SPR of Al NPs and the grating substrate. These recent improvements in the experimental design and parameters are valuable to studying any nanoenergetic system's local reaction.

CHAPTER 6 : SURFACE PLASMON ENHANCED FLUORESCENCE TEMPERATURE MAPPING OF ALUMINUM NANOPARTICLE HEATED BY LASER

Partially aggregated Rhodamine 6G (R6G) dye is used as a lights-on temperature sensor to analyze the spatiotemporal heating of Aluminum nanoparticles (Al NPs) embedded within a tetrafluoroethylene, hexafluoropropylene, and vinylidene fluoride (THV) fluoropolymer matrix. The embedded Al NPs were photothermally heated using an IR laser, and the fluorescent intensity of the embedded dye was monitored in real time using an optical microscope. A plasmonic grating substrate enhanced the florescence intensity of the dye while increasing the optical resolution and heating rate of Al NPs. The fluorescence intensity was converted to temperature maps via controlled calibration. The experimental temperature profiles were used to determine the Al NP heat generation rate. Partially aggregated R6G dyes, combined with the optical benefits of a plasmonic grating, offered robust temperature sensing with sub-micron spatial resolution and temperature resolution on the order of 0.2 °C.

6.1 Introduction

Understanding thermal transport between constituents of energetic nanocomposites containing aluminum nanoparticles (Al NPs) is essential to the design and implementation of more efficient energetic formulations. Nanocomposites incorporating Al NPs are among some of the most widely used solid-state fuels due to the natural abundance of aluminum and high exothermicity of oxidation reactions involving aluminum. In particular, the interaction of Al NPs with reactive fluoropolymer films has attracted significant interest as fluoropolymers may be cast onto a diverse set of substrates and are compatible with additive manufacturing [18,22,166,171,172].

The reaction properties and mechanisms of energetic fluoropolymer films have been widely studied by measuring the reaction temperature evolution to understand thermal characteristics and heating kinetics [173–175]. Recently, we reported an *in situ* study of isolated fuel nanoparticles reactions by photothermal heating on a plasmonic grating platform to understand differences in the behavior of Al NP reactions with fluoropolymer and metal oxide constructs [50,176]. Despite numerous recent advances, many fundamental aspects of energy flow and reaction mechanisms of nanoenergetic materials are poorly understood, in part due to experimental limitations in high-resolution thermal sensing.

Recently, we reported an *in-situ* photothermal heating platform using plasmonic gratings with reversible temperature-induced quenching effect [24]. R6G works particularly well in a grating system with ~400 nm pitch since the coupling angles for the wavelength ranges of both excitation and emission of R6G lie near normal angles of incidence, creating an optimal window for dye fluorescence and detection of temperature effects. In the previous report, the reversible ‘lights-off’ quenching behavior was attributed to the low concentration of R6G dye (1 µM) used in the sol precursor to avoid aggregation of the dye in the nanocomposite film. Meanwhile, temperature-induced disaggregation has been reported in highly concentrated dye films subjected to high-temperature annealing [177]. With a highly concentrated dye film, aggregates in dimer state self-quench, significantly reducing fluorescence efficiency compared to the monomer state. Temperature-induced disaggregation would result in a 'lights-on' increase in fluorescence intensity with increasing temperature. Such a scheme would be preferential to a ‘lights-off’ nanothermograph

as it would be much easier to isolate the temperature-induced response from photobleaching and reduce background interference at high temperature.

Herein, we report a R6G aggregate-based nanothermometer built upon a plasmonic grating platform fabricated by nanoimprint soft lithography [24,68]. The nanothermography system is used to analyze the spatiotemporal thermal response of photothermally heated Al NPs embedded within a tetrafluoroethylene, hexafluoropropylene, and vinylidene fluoride (THV) polymer matrix. R6G dye molecules were dispersed at sufficient concentration to form dimer aggregates in a micron-thick Al NP/THV/R6G nanocomposite film. Individual Al NPs were heated using a high-power-density laser integrated into a tabletop upright microscope with a high-resolution CMOS camera for obtaining spatiotemporal image sequences of the dye response. The time-resolved fluorescence was converted to temperature maps via controlled calibration, and the temperature-dependent response was used to calculate the volumetric heat generation rate of the Al NP.

6.2 Grating Fabrication

Plasmonic grating substrates were fabricated using a microcontact lithography stamping process [68,106,108,125–127,178]. HDDVD grating structure was replicated by curing 5:1 Sylgard® 184 polydimethylsiloxane (Gelest) over a halved, cleaned HDDVD for 24 hours at 50 °C and 55% relative humidity. Meanwhile, glass microscope slides (Corning) were cleaned by successive bath sonication in acetone, methanol, and deionized water, and dried under flowing nitrogen. Cleaned slides were then soaked for 10 minutes in 3:1 H_2SO_4:H_2O_2 (Piranha solution), washed twice and rinsed in fresh deionized water, and dried under flowing nitrogen. Polymer ink consisting of 3% w/w GR650F polymethylsilsequioxane (Techneglas) in ethanol was

spun-cast onto the stamp at 3000 rpm for 30 s and pressed onto the cleaned glass slide. The gratings were then vapor-treated with 1:1 3-aminopropyltriethoxysilane (APTES) in ethanol, pre-baked at 60 °C for 3 hours, and baked at 400 °C for 1 hour. A 5 nm titanium adhesion layer was added before depositing 100 nm silver (Ag) by RF sputtering and a 10 nm protective layer of alumina (Al_2O_3) using atomic layer deposition. Identical to previous reports [68,179], the expected topography (400 nm pitch and 60 nm peak-to-valley height) was confirmed by atomic force microscopy prior to nanocomposite film deposition.

6.3 Nanocomposite Material Fabrication

Aluminum nanoparticles (Al NP) with 120 nm average diameter were purchased from Novacentrix (Austin, TX, USA). The aluminum nanoparticles have a core-shell structure consisting of a metal aluminum core and an Al_2O_3 shell of 2-3 nm as a passivation layer to protect the reactive aluminum content. In the current work, the specific oxide thickness does not play a critical role in the results; however, the shell thickness is important when reacting the Al NPs with oxidizers. Rhodamine 6G (R6G) was purchased from Exciton (Dayton, OH, USA) and THV 220A fluoropolymer with glass transition temperature (T_G) of 26 °C and melting point (T_M) of 120 °C from 3M Company (St. Paul, MN, USA). Al NPs and THV were separately dispersed in acetone with starting concentrations of 1 mg/ml and 60 mg/ml, respectively, and sonicated for 3 hours. R6G stock solution was prepared by adding 10 mM R6G in 2-propanol (IPA) and sonicating 10 minutes. The constituent materials were then mixed to achieve a final concentration of 0.25 mg/ml Al NPs, 50 mg/ml THV, and 100 μM R6G, respectively, and sonicated for 2 hours to ensure a well-dispersed mixture. Immediately after sonication, a 0.5 ml aliquot of the mixture was spin-coated at 3000

rpm for 30 s onto a plasmonic grating substrate produced as described above. A relatively low (0.1% w/w) ratio of Al NP to THV resulted in sparsely distributed particles within a relatively thick (~1 μm) THV matrix. The film was cured in a saturated acetone vapor environment for 4 hours to improve film uniformity and smoothness [50], then dried in a vacuum oven at 60 °C for 1 hour to remove any remaining solvent. The final cured nanocomposite thin film retains the low ratio of Al NP:THV, but dye concentration increases to ~4 mM due to volume reduction from solvent evaporation (**Figure 6-1(a)**).

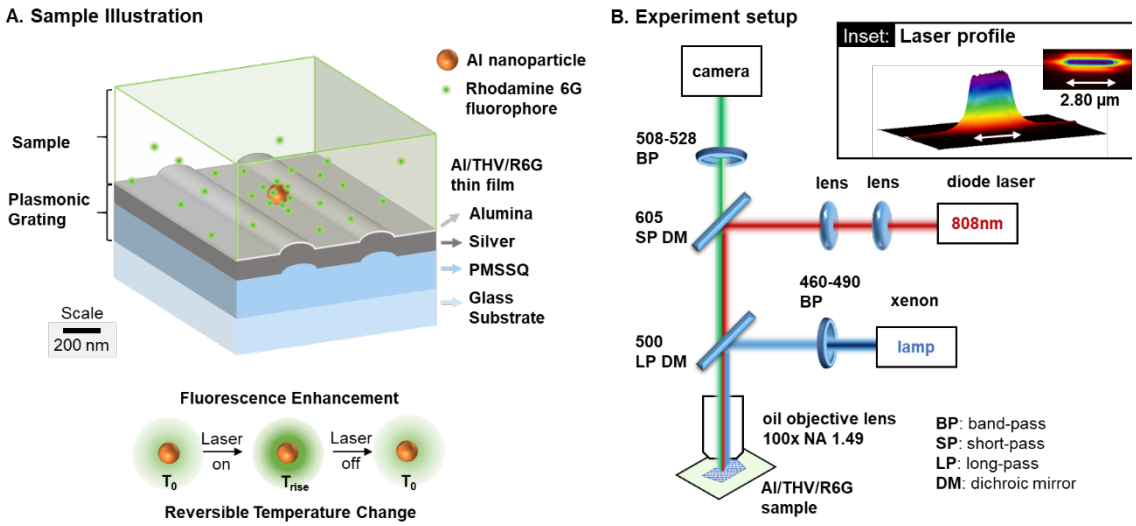

Figure 6-1. (a) Schematic of an energetic nanocomposite thin film deposited on a plasmonic grating substrate and (b) Schematic of experimental setup for in-situ photothermal heating of a single nanoparticle in fluorescence-temperature measurement incorporating laser, microscope, and camera systems. (Inset) Laser profile as focused to deliver energy specifically to the Al NPs.

6.4 Fluorescence Thermography Apparatus

Laser heating experiments to evaluate temperature-dependent fluorescence require the ability to collect fluorescence image sequences during laser heating, focus on specific Al NPs within the nanocomposite, and align the laser in the optical train.

We designed a custom optical setup to accommodate these requirements (**Figure 6-1(b)** and **Figure 6-2**), which includes i) a laser mount with focusing lenses and micropositioner, ii) an optical filter set for beam formation and fluorescence excitation and emission, and iii) a laser synchronization driver. A 300 mW-rated near-infrared 808 nm diode laser was chosen for the heating source since the high absorption efficiency of Al NPs in the near-infrared regime is thought to support photothermal heating by plasmonic coupling and dielectric loss [101]. Meanwhile, the 808 nm laser light will couple weakly to the silver grating at a 0° angle of incidence (i.e. normal incidence) reducing the direct heating of the grating significantly with respect to visible range lasers [24]. The laser produces a beam with elliptical Gaussian profile, which was focused by the lenses and 600 nm short-pass dichroic mirror to a beam of 2.8 µm long x 0.20 µm wide at full width half maximum on the substrate (**Figure 6-1(b)**, inset).

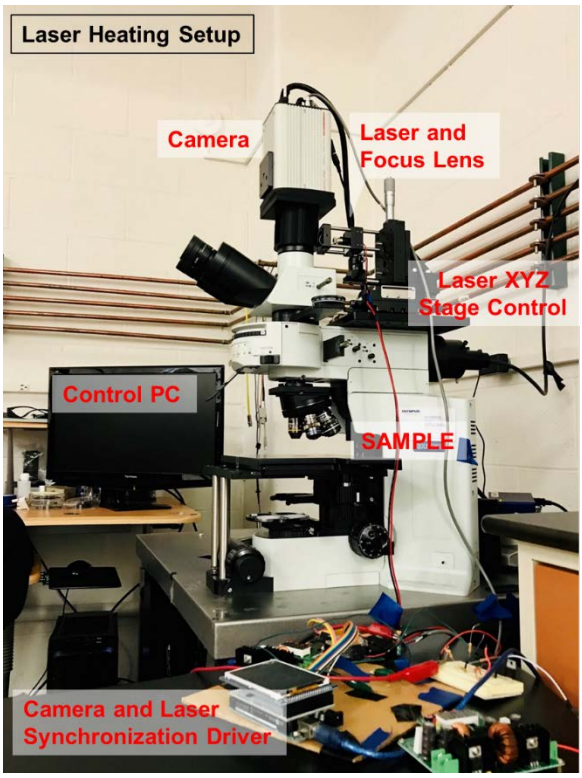

Figure 6-2. A photo of the experimental setup for in-situ photothermal heating of a single nanoparticle in fluorescence-temperature measurement incorporating laser, microscope, and camera systems. (Inset) Laser profile as focused to deliver energy specifically to the Al NPs.

The optical filter setup is arranged to enable both fluorescence excitation and laser light to be delivered through the optical train to the sample while simultaneously screening these wavelengths from the imaging camera. Proper screening was achieved by using a pair of dichroic mirrors, including: i) a short-pass mirror with 605 nm cut-off to reflect the 808 nm laser through the objective lens toward the sample and ii) a long-pass mirror with 500 nm cut-off to both reflect the excitation light and pass the laser to the sample. The excitation filter (460 – 490 nm) and 500 nm long-pass dichroic mirror were placed in a standard filter cube slot in the microscope. The 605 nm short-pass dichroic mirror and a 508 – 528 nm band-pass emission filter were placed in a second filter cube and loaded in a 3D-printed adapter between the microscope proper and the camera.

6.5 Temperature-Intensity Calibration

The temperature-dependent fluorescence spectra of R6G embedded in the nanocomposite matrix was characterized using a BioTek™ Synergy™ H4 Hybrid microplate reader. A xenon white light flash lamp was cut to 480 ± 9 nm excitation band and emission screened from 500 – 700 nm. The microplate reader was programmed to first heat the sample to 30 °C, wait for 15 minutes to achieve steady-state, measure the spectrum, and then repeat in 5 °C increments up to 65 °C, the instrument maximum. Finally, the sample was cooled to 30 °C and measured a final time.

The relationship between temperature and fluorescence intensity was calibrated based upon the lower wavelength/higher energy component of the R6G fluorescence spectrum, namely, the range that experiences the highest relative increase in intensity with increasing temperature (**Figure 6-3(a)**). To accommodate this also in the microscope, we designed a custom fluorescence filter cube that includes 460 – 490 nm band-pass excitation filter, 500 nm dichroic mirror, and 508 – 528 nm band-pass emission filter (**Figure 6-1(b)**). The sample was placed under the microscope objective on a closed-loop heating stage with an embedded thermocouple. The stage was slowly heated from 30 and 70 °C in 10 °C increments. After a dwell time of 15 minutes to achieve steady-state, several images were acquired from different areas of the sample at each temperature. Fluorescence intensity was extracted from the images using ImageJ software for later conversion to temperature maps [180].

6.6 Fluorescence Thermography Experiment Strategy

The power output of the laser was measured to obtain the irradiated power delivered to the nanoparticle through the optical train. A Newport 843-R optical power

meter measured the power output of the 300-mW rated diode laser. The measured laser power was 285 mW denoting the initial power input to the experiment setup. Then, the power meter was placed in line with the 100× objective lens at the end of the optical train. After losses from the optics, laser filters, and dichroic mirrors, the laser power delivered to the sample was 0.1 mW. Using this measured laser power and the laser dimension, the power density of the laser was approximately 17,000 W/cm^2 at the sample surface.

Heating of single Al NP in the THV/R6G matrix was captured using an Olympus BX51WI epifluorescence microscope equipped with Hamamatsu ORCA flash 2.8 CCD camera. Images were obtained at 40 frames per second (fps) at 2.8-megapixel resolution, providing a temporal resolution of 25 ms. The imaging objective lens was an Olympus UAPON 100× oil-immersion lens with a numerical aperture of 1.49. The combination of the high-power objective lens and grating coupling effect provided subwavelength resolution (36 nm per pixel), facilitating the visualization of individual nanoparticle [50]. ImageJ software was used to process experimental images and to convert fluorescence intensity into temperature maps. A time-averaged sequence of the three frames just prior to laser heating was collected to use as an ambient reference image to reduce inherent signal noise. The temperature conversion normalized each frame to the initial ambient temperature intensity. Each subsequent heating frame (I) was normalized by the initial time-averaged frame (I_{30}) and translated to a temperature map via pixel-by-pixel conversion.

6.7 Temperature-dependent Spectral Result

The fluorescence spectra of R6G in the Al NP-R6G-THV nanocomposite taken in the microplate reader is given in **Figure 6-3(a)**. The 'initial condition' spectrum

acquired at 30 °C shows a dominant primary peak at 540 nm and a shoulder peak at ~560 nm. These peak locations are blue-shifted by about 10 nm with respect to the expected peak locations for dye aggregates in either solution [181–183] or solid thin films [184]. We attribute the blue-shifted fluorescence emission to the well-documented surface plasmon-coupled emission (SPCE) effect over plasmonic gratings [101,127], whereby the excited state energy of the fluorophore is transferred nonradiatively back to the grating prior to radiative emission by scattering from the grating itself. This process reduces the energy lost to internal conversion within the dye prior to radiative emission and produces a blue shift regardless of other effects. Considering the plasmon-induced blue shift, we associate the 540 nm peak with the R6G monomer and the 560 nm peak with a population of randomly oriented J-type dimers formed by aggregation in the THV matrix [185]. While the concentration of R6G in solution is 100 μM, solvent evaporation during spin-casting and subsequent curing and annealing steps greatly reduces the total volume of the nanocomposite matrix so that the final concentration of dye is on the order of 4 mM. The interactivity of the fluoropolymer with R6G is expected to be low, suggesting that dye molecules may be sequestered together in pockets formed by the evaporating solvent. Combining these effects, the transition of R6G concentration from 10^{-4} M to 10^{-3} M regime is sufficient to form dimers with lower quantum efficiency, both through increased internal conversion of the J-type dimers prior to emission as well as quenching of remaining monomer units through monomer-to-dimer energy transfer [185].

Upon heating, the primary peak experiences an increase in intensity with increasing temperature and the peak wavelength blue shifts from 540 nm at 30 °C to

535 nm at 65 °C (**Figure 6-3(a)**, solid lines). Meanwhile, the 560 nm shoulder peak decreases in intensity with increasing temperature. The combination of shifting and increasing primary peak intensity and decreasing shoulder intensity indicates that increased temperature promotes disaggregation of dyes, either J-dimer decoupling into individual monomers or separation of monomers beyond the energy transfer distance from adjacent dimers, allowing the recovery of monomer fluorescence emission. In samples both liquid and solid, blue-shifting upon exposure to light may also result from simple photobleaching, which irreversibly damages dyes and isolates remaining emissive molecules as damaged dyes are screened out of the optical system. However, the recovery of the quenched fluorescence emission state on the cooling cycle demonstrates the reversibility of the temperature-induced peak-shifting effect (**Figure 6-3(a)**, dash-dot lines). Moreover, the films are highly stable and reusable over several experiments with little change in spectral properties, including intensity, peak locations, and response to heating and cooling cycles, so photobleaching is not considered a significant contributor to this effect. Two potential mechanisms can explain the reversibility of heating after disaggregation. First, dye molecules participating in J-dimer aggregates may separate or experience a change in angle of association with increasing temperature, recovering quantum efficiency lost to internal conversion and reabsorption in the J-dimer state [177]. Second, disaggregation and separation are further supported by the relatively low glass transition temperature of THV (T_g = 26 °C). Essentially all of the calibration spectra were collected above this temperature, so the polymer chains will become increasingly mobile with increasing temperature and time. Thus, monomers quenched by energy transfer to J-dimers or higher order aggregates may separate sufficiently to recover fluorescence emission. Both effects are likely to contribute to the overall increase in

monomer fluorescence emission. Viscous deformation of THV may also contribute to the residual shift in the spectra upon cooling to 30 °C, as some dyes are permanently isolated from each other and do not return to sufficient proximity for energy transfer as the surrounding matrix relaxes to a new, more thermodynamically favored resting state. While the focus of the present work is to use the dye as a reporter for temperature, the exact processes governing the fluorescence emission of the highly-concentrated state in the presence of plasmonic grating and associated temperature dependence are under further study.

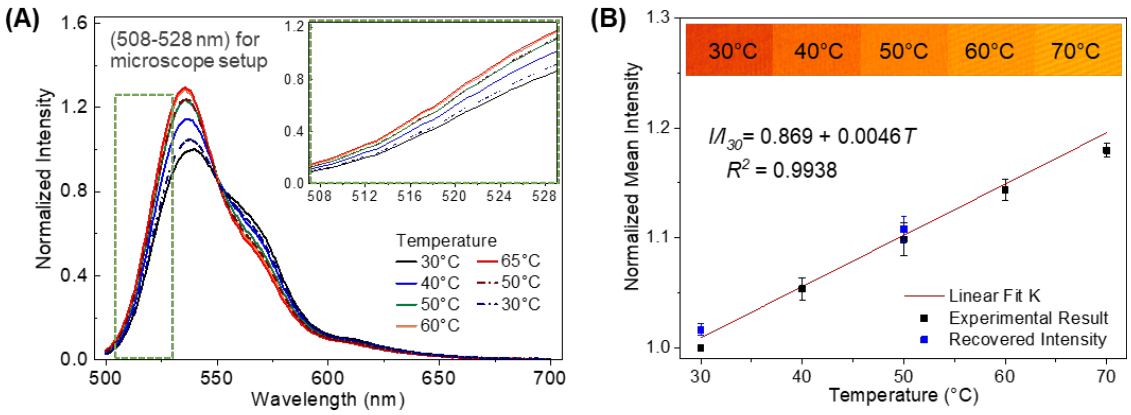

Figure 6-3. (a) Fluorescence emission spectra of R6G as a function of temperature measured using the microplate reader; solid lines represent spectra during heating cycle while dot-dash lines represent spectra during cooling. The green boxed region and inset are the 508 – 528 nm range selected for the imaging experiments. (b) Averaged R6G fluorescence micrograph pixel intensities as a function of temperature captured through 508 – 528 nm bandpass filter and normalized to the reference intensity at 30 °C. Line represents linear fit with equation and associated R^2 in plot. (Inset) False-colored fluorescence micrographs demonstrating intensity changes with increasing temperature.

6.8 Temperature-dependent Image Properties

Correlating the temperature-dependent effects captured by the microscope with the changes seen in the microplate reader is essential to defining the spatial characteristics of the film response during nanoparticle heating [24]. For image-based

thermography, our goal was to selectively capture the 'lights-on' temperature-dependent increase in the primary peak seen in the spectra above. Whereas spectroscopic analysis considers wavelengths of light individually and a ratiometric measurement between the primary peak and shoulder would be preferable, image-based thermography considers all captured wavelengths in a single pixel as one data point for that region in space. A decrease in photons of wavelengths represented in the shoulder peak would also detract from the total photons captured by the camera and dampen any temperature-dependent increase in the primary peak. In other words, we must sacrifice spectral resolution in favor of spatial resolution in this experiment. Hence, a 508 – 528 nm bandpass emission filter was selected to screen out the shoulder peak for imaging experiments and capture only the portion of the primary peak that increases with increasing temperature (**Figure 6-3(b)**, inset). The resulting fluorescence intensities of seven distinct regions of the film without Al NPs were averaged together to produce a single calibration point for each temperature and normalized to the reference intensity at 30 °C (**Figure 6-3(b)**). The relatively small standard deviation about the mean at each point demonstrates the temperature uniformity throughout the entire field-of-view of the sample. A clear linear relationship was observed between film temperature and the fluorescence emission intensity when the film was heated from 30 °C to 70 °C. The fluorescence image intensity increases approximately ~200 (a.u.) over the increasing temperature of 40 °C, the calibrated temperature resolution is on the order of 0.2 °C. A first-order linear approximation was fit to the normalized data (R^2 = 0.994) and given as: $\frac{I}{I_{30}} = 0.869 + 0.0046T$, where I is the fluorescence intensity at arbitrary temperature, I_{30} is the reference fluorescence intensity at 30 °C, and T is the temperature. Solving for T, we find that

$$T = 217.39 * \frac{I}{I_{30}} - 188.9 \quad (1)$$

After one heating cycle, the sample was slowly cooled and the intensities at 50 °C and 30 °C were captured to demonstrate the reversibility of the temperature-dependent response (**Figure 6-3(b)**, blue points). These two points were chosen as settling to steady-state during cooling took significant time after heating with the Peltier device as the grating and glass substrate continue to contribute heat to the R6G-THV system after the Peltier has been cooled. Critically, the fluorescence was found to recover after cycling back to 30 °C with no statistically significant difference in intensity. The reversibility and repeatability of the intensity increase that a single particle might be used for multiple experiments, especially those exploring the effect of increasing laser fluence on heating and heat dissipation.

The temperature resolution and response sensitivity to changes in temperature are of significant importance as these factors determine how reliably we can observe changes in temperature due to laser heating. Temperature resolution (unit of °C) measures the smallest change in temperature in respect to the change in fluorescence indicator, whereas the relative or response sensitivity (unit of %/°C) is the percentage of the change in the fluorescence indicator to itself in respect to change in temperature. Herein, we have achieved temperature resolution of 0.2 °C and response sensitivity of -0.4 %/°C. These values compare well to those of prior reports using molecular dyes as the temperature reporter. As stated above, molecular dyes in the rhodamine family have been widely researched for their thermometry applications. One of the most representative examples is the use of rhodamine B for measurement of fluid temperature in microfluidic systems [72]. The technique measures the temperature

distribution of microfluidic circuits as a consequence of Joule heating. The photoluminescence intensity and temperature response were calibrated up to 90 °C with temperature resolution ranging from 0.03-3.5 °C depending on the signal processing method. The spatial and temporal resolutions achieved were 1 μm and 33 ms, respectively. More recently, fluorescent rhodamine B-doped latex particles were developed as temperature sensing devices with reversible response [186]. The peak fluorescence intensity had a linear response to temperature changes over the range of 30−100 °C with response sensitivity of −0.93 %/°C. This intracellular heat mapping with sub-micrometer resolution demonstrated a nonuniformity of temperature distribution of locally heated gold nanoparticles excited by a laser. Rhodamine derivatives have also been incorporated for super-resolution cell imaging at spatial resolution of 50 nm, although the temporal resolution was on the order of seconds [187,188]. Previously, our group reported a thermometry sensor having fluorescence intensity decreases with temperature attributed to quenching behaviors with temperature resolution of 0.14 °C and response sensitivity of -0.38 %/°C [24]. Although that report demonstrated superior temporal resolution at 2 ms, the 300 nm spatial resolution is lower compared than the 36 nm/pixel achieved in this work. Additionally, the dye concentration has been altered such that fluorescence intensity increases with temperature.

6.9 Characterization of Al NPs Heated in R6G-THV Matrix

The morphologies of Al NPs embedded in the R6G-THV matrix were characterized by bright field, fluorescence, and scattering imaging modes before and after laser-induced heating (**Figure 6-3(a)**). Bright-field imaging was used to locate single Al NPs and to focus and align the laser so that the targeted Al NP was aligned

to the center of the laser beam profile. The bright field imaging mode is particularly useful for identifying single particles in the presence of R6G since bright field interrogation uses the lowest overall light intensity, minimizing the potential for photobleaching prior to laser heating. Initially, Al NPs in bright field mode appear as dark spots against the bright grating background due to the relatively low reflection of light. No noticeable changes in morphology were apparent in the Al NP after heating with 808 nm laser. Previously, we reported that heating of Al NP clusters with 808 nm laser generated a greater heating rate than other wavelengths used in that work [24,101], so the absence of morphology change suggests that no permanent effects (e.g. ignition) occurred during heating with the 808 nm laser at the current laser fluence. This is confirmed by the equivalent image in scattering mode using both polarizer and analyzer at 0° with respect to the grating axis, which reveals depolarization effects due to the metallic content of Al NP. At 0°, any backscattered s-polarized light from the grating is screened out, while p-polarized light is coupled to the grating. Thus, the only remaining high intensity light to reach the camera is the scattered, depolarized light from the Al NP. Analyzing such changes in scattering intensity has been used extensively for *in-situ* observation of laser-ignited Al NP and THV combustion [50,110]. Al NPs heated in the current experiment do not show the characteristic changes in scattering intensity brought about by restructuring and oxidation of the aluminum during laser-induced combustion. This result is critical as the subsequent studies demonstrate the heat dissipation of Al NPs to their environment as a result of heating alone rather than temperature increases due to more catastrophic laser-induced combustion events.

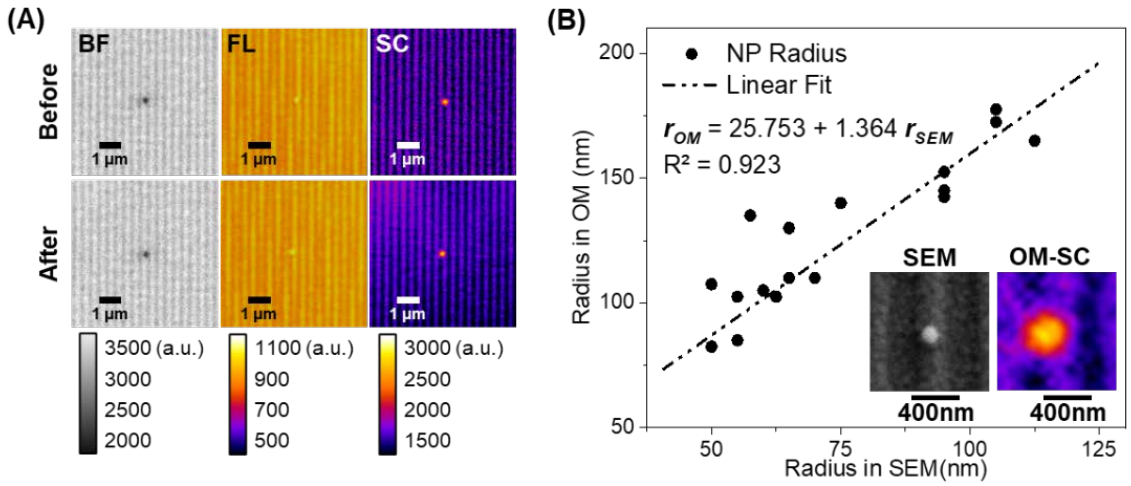

Figure 6-4. (a) Single Al NP imaged before and after laser-induced heating using bright field (BF), fluorescence (FL), and polarization-based scattering (SC) modes. (Note: images are false-color with intensity indicated by the intensity bars. (b) SEM and polarization-based scattering optical microscope images are used to calculate the ratio to measure the actual dimension of the nanoparticle. (Inset) SEM and optical microscope scattering (OM-SC) images of the same Al NP at the same relative scale.

In fluorescence mode, R6G serves as a reporter dye with the initial temperature-independent pixel intensity correlating with the local electric field due to the plasmonic effect and those mentioned in the previous section on calibration. Both R6G excitation and emission spectra overlap strongly with the surface plasmon resonance coupling peaks of the grating at near-normal incidence, resulting in enhanced fluorescence intensity of the fluorophores and enhanced capture through directed emission toward the photodetector (i.e. camera) [24]. Excitation may be enhanced via plasmon resonance energy transfer (PRET), while emission is enhanced due to aforementioned SPCE [108,189,190]. The grating lines are apparent in the fluorescence micrograph as the plasmon-induced electric field varies between the peaks and valleys of the grating. Notably, the fluorescence of R6G localized near the Al NPs is elevated with respect to the surrounding bulk. Previously, we reported that large clusters of Al NPs appeared as dark regions in the center of a bright, fluorescent

field due to the inability of the R6G dye to penetrate between the constituents of the Al NP cluster [24]. By contrast, the particles in **Figure 6-4(a)** appear as bright, contiguous spots, indicating R6G dye can fully coat the Al NP surface and, critically, that we have visualized a single Al NP. This is due in part to plasmonic interaction between the Al NP and the Ag grating across the small dielectric gap created by the Al_2O_3 layer and any R6G-THV matrix between the Al NP and grating surface. This nanogap serves as a hotspot for electric field, which further enhances the fluorescence of dyes localized to the particle than that of dyes localized to the grating. However, this increase in initial intensity over Al NPs does not appear to impact the relative temperature-dependent response and, so, the relative intensities are still governed by Eq. 1 given above. This feature is important to distinguish between single Al NPs and Al NP clusters, allowing us to classify particles by cluster size and isolate classes of particles for further study.

Accurate measurement of the Al NP radius is critical to determining the volumetric energy generation rate of photothermally heated Al NPs. **Figure 6-4(b)** compares the measured radii of several Al NPs determined from scattering images in the optical microscope with the ground truth radii determined for the same particles by FEI Quanta 600 FEG scanning electron microscope (SEM). The observed dimension of nanoscale Al NPs in the optical microscope is slightly larger than the reported dimension due to the diffraction limit and the size-dependent absorption and scattering cross-sections of Al NPs, which produce a cone of light emitting from the particle. The conversion between SEM images to optical microscope scattering images can be fit to a linear relationship with $R^2 = 0.923$ (**Figure 6-3(b)** text).

6.10 Laser-induced Photothermal Heating

The mechanism of Al NP photothermal heating occurs via absorption of incident photons at the surface of the nanoparticle [191,192], which excite electrons and generate phonons through electron-lattice relaxation processes [193]. Thermal conduction spreads the heat within the nanoparticle and to the surrounding THV film. **Figure 6-5** shows sample sequential fluorescence micrographs of the Al NP-R6G-THV nanocomposite in different platform and experimental conditions to demonstrate the importance of grating coupling on the elucidation of laser-induced heating. Notably, the embedded Al NPs supported on a flat silver substrate do not show an appreciable increase in temperature, as seen in the converted temperature map (**Figure 6-5 (a-b)**).

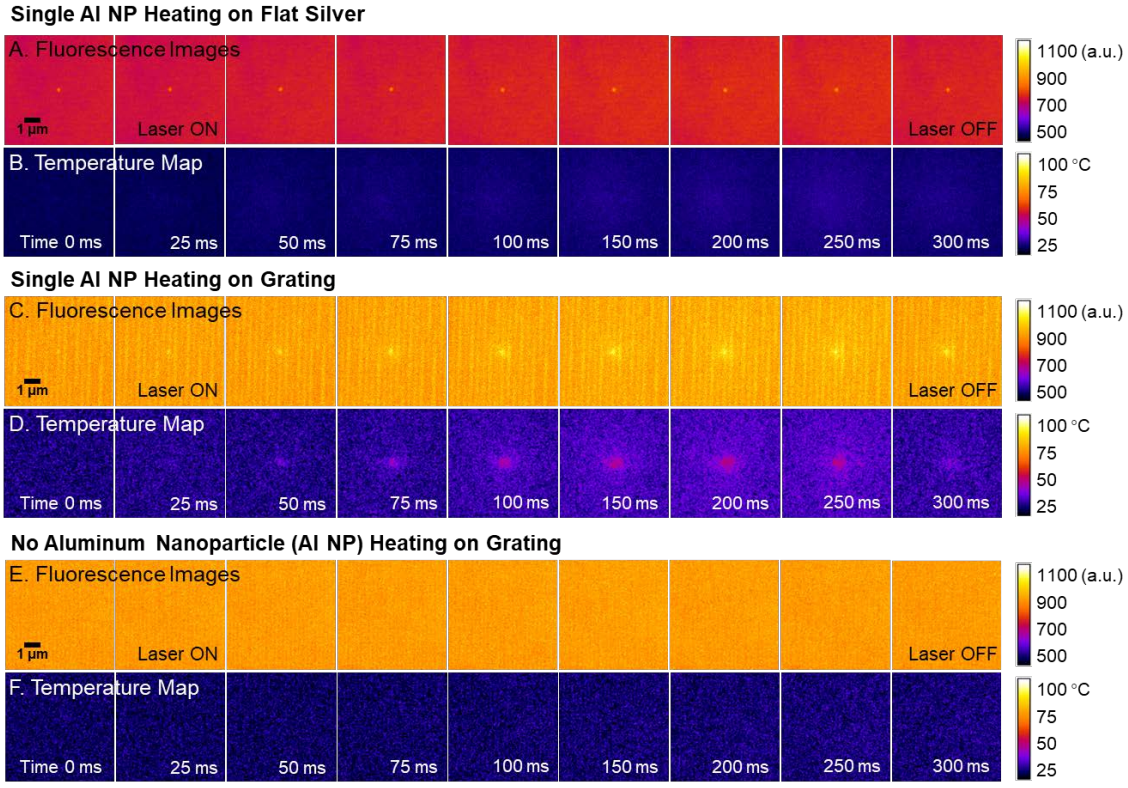

Figure 6-5. The time sequence of fluorescence intensity and temperature during laser irradiation were shown in the false colored images. Heating of single nanoparticle embedded

in a 1 μm Al/THV/R6G film and supported on a (A-B) flat silver and (C-D) plasmonic grating substrates indicating rapid localized heating followed by rapid cooling after the laser is turned off. (E-F) The laser was also irradiated Al/THV/R6G film on a grating substrate with the absence of Al NP.

The plasmonic grating acts as a reflective substrate and a light coupling device to generate more heat than a flat silver substrate under laser photothermal heating (**Figure 6-5**). The heating rate of Al NPs with 808 nm laser is enhanced from the plasmonic coupling, which falls within the broad Al absorption spectrum. Absorption spectra consist of the combination of plasmon resonance and interband transitions [194,195]. The 808 nm near-IR laser overlaps with a portion of Al absorption spectra associated with the dielectric loss [193]. The interband transitions of bulk aluminum has an intrinsic peak at 810 nm and the peak intensity grows with increasing particle diameters [196]. Below 600 nm, Al NPs can exhibit dipole, quadrupole, octupole plasmonic resonances of which peak wavelengths are red-shifted as the diameter increases [130]. The better confinement of light at these lower wavelengths leads to higher absorption such that the 808 nm wavelength exhibits a relatively weak plasmonic coupling compared to other laser wavelengths. For instance, 446 nm blue and 632 nm red lasers have been utilized as a heating source for Al NP and shown a greater electromagnetic coupling due to higher plasmonic absorption, rather than its dielectric loss [50]. The effect of the plasmonic heating leads to the heating of the grating which is undesirable for thermometry purposes. The use of 808 nm laser was beneficial due to the drastically diminished heating of the grating substrate.

The duration of laser heating was selected to study the local temperature of the heated film surrounding the nanoparticle. In a separate experiment (**Figure 6-6**), the

Al NP was exposed to laser heating for a duration of 400 ms with images obtained every 25 ms. The THV/R6G film reached a stable temperature profile at ~200 ms, hence all experiments presented here used a laser exposure time of 250 ms. Each nanoparticle was imaged in bright field, fluorescence, and scattering modes before and after heating. Note that the plasmonic grating is identifiable in the background of the images (**Figure 6-5**). More importantly, the isolated single nanoparticle can be readily distinguished from small Al NP clusters in scattering mode. No optical or morphological changes of Al NPs in the THV film as a consequence of heating were observed, indicating that the NP did not react with the surrounding THV. Excessive laser heating may melt the surrounding THV medium at about 120 °C, causing the particle to shift its position, which was previously reported [24]. Hence, the laser heating was maintained below this critical value to avoid any Al NP translation.

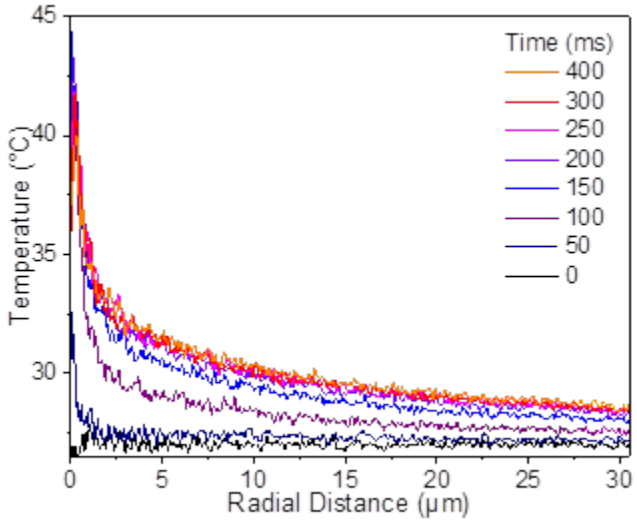

Figure 6-6. Al NP was exposed to laser heating for a duration of 400 ms with images obtained every 25 ms. Only some time steps of the radial temperature profiles are presented to assist observation. The temperature rise of the Al NP is apparent, and the Al NP and THV reach a steady-state temperature profile at ~200 ms - 250 ms

During particle heating, the fluorescent intensity of the dye-coated nanoparticle increased rapidly under laser irradiation. The surrounding THV matrix fluorescent

intensity also increased in the immediate vicinity of the Al. A representative dynamic image sequence demonstrating the transient fluorescence and temperature maps are shown in **Figure 6-5**. These images represent a 6 µm × 6 µm cropped area from the raw images with a dimension of 69.8 µm × 52.4 µm (**Figure 6-7**). The temperature rise of the Al NP is apparent, and the Al NP and THV reach a steady-state temperature profile at ~200 ms. Based on measurements obtained in concentric circles around the heated NP, the temperature distribution was radially symmetric, further emphasizing that no additional heat was generated from the THV medium or the plasmonic grating. When the laser heating was extinguished at 250 ms, the temperature of the THV rapidly decayed.

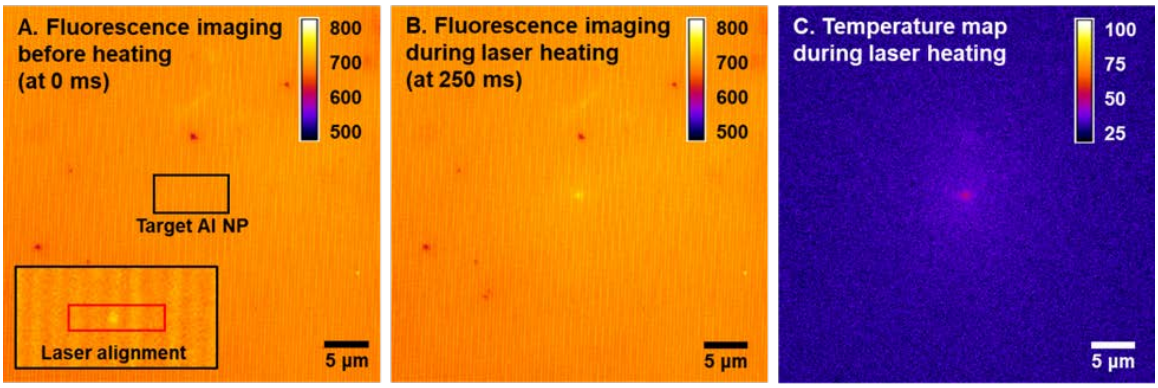

Figure 6-7. False-colored fluorescence image captured before heating showing the location of the target Al NP. The inset depicts the Al NP aligned to the focus of the laser prior to laser exposure. (b) During laser heating, the fluorescence intensity was elevated due to the photothermal heating of Al NP. (c) The temperature map is obtained from the fluorescence image using the calibration equation. Intensity bars for (a) and (b) indicates the fluorescence intensity while for (c) is the temperature (°C).

It is important to note that the fluorescence intensity changes were not observed in the absence of an Al NP. As an initial control experiment, the laser was irradiated on a sample area without Al NPs for 250 ms. No increase in intensity from the initial temperature was observed, indicating that the THV, which has a low optical absorption

at 808 nm, and the grating substrate do not absorb the laser energy shown in **Figure 6-5(e-f)**. Silver is widely used in plasmonic applications due to its inherently low loss [108,197]. In contrary, aluminum, is a high loss material and not an attractive plasmonic material with interband transition located in the near-IR. These findings indicate that Al NP is the only source of laser energy absorption and the heating source to the surrounding THV medium.

6.11 Aluminum Nanoparticle Photothermal Heat Generation

The plasmonic grating not only enhances fluorescence excitation and emission, but also the local electric field and photothermal heating experienced by a nanoparticle in close proximity to the grating. The electric field enhancement factor provided by a plasmonic grating is difficult to determine experimentally and is a complex function of NP radius, NP composition, laser wavelength and incidence angle, and placement of the NP relative to the grating ridges. The spatially resolved THV temperature profiles enabled by the dye facilitated an estimation of the THV temperature gradient, and, by extension, the Al NP heating rate for each particular nanoparticle radius.

For each of the experiments, the resulting fluorescence images were converted into a spatial temperature map. Scattering images were used to estimate the dimension of each Al NP, using the correlation shown in **Figure 6-4(b)**. A representative transient THV temperature profile resulting from a single 120 nm diameter Al NP is shown in **Figure 6-8**. Radial temperature profiles were obtained by averaging the temperature map over the entire angular domain from 0–2π radians in ImageJ software. To smooth the raw data, binning was performed for each pixel with the average of its 3x3 pixel neighborhood. The temperature in the vicinity of the heated

single Al NP increased and reached steady-state with the peak temperature of 48.5 °C within 200 ms. While the region of greatest temperature was localized around the Al NP itself, the heat-affected region extended radially outward for tens of microns with time (**Figure 6-8**).

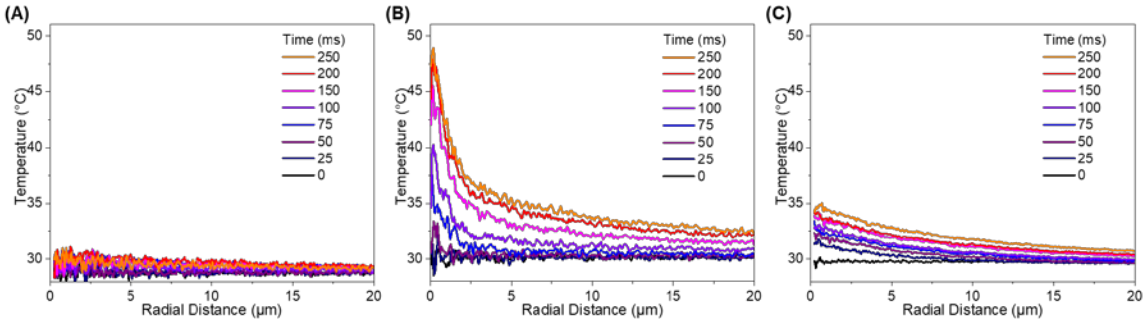

Figure 6-8. The time sequence of radial temperature profiles during laser irradiation. (a) The laser initially irradiated Al/THV/R6G film on a grating substrate with the absence of Al NP. Radial temperature profiles from the temperature maps of heated 120-nm Al NP supported on a (b) plasmonic grating and (c) flat silver substrates showing time-sequence before (at 0 ms) and during laser-induced heating.

The resulting temperature profiles for three different Al NP radii supported on a plasmonic grating and flat silver substrate are summarized in **Figure 6-9(a-b)**. For all experiments, the temperature profile generated on the grating substrate exceeded that observed for a similar Al NP supported on a flat silver substrate for identical laser heating parameters. The temperature profile observed for both substrates increased with Al NP radius; furthermore, the temperature difference between the grating and flat silver substrates increased with radius. As an example, the maximum THV temperature recorded using a plasmonic substrate increased from 42.7 °C to 59.8 °C as the Al NP radius increased from 45 to 75 nm. The maximum temperature observed using a flat silver substrate increased from 34.4 °C to 36.9 °C for the same Al NP radii.

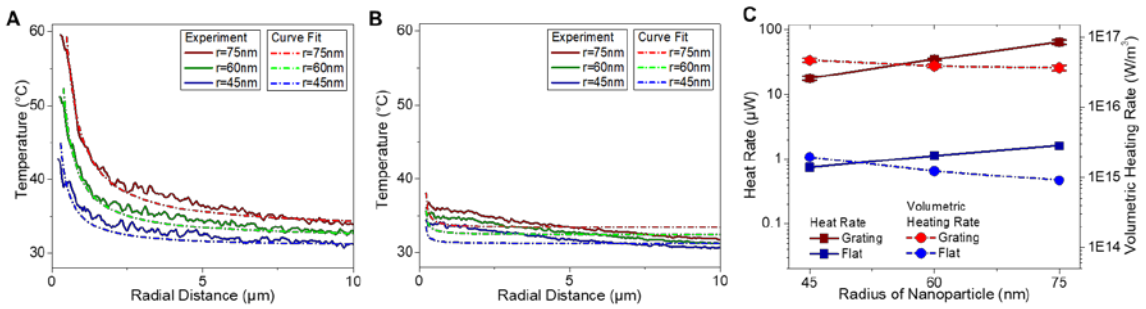

Figure 6-9. Steady-state radial temperature profiles were obtained experimentally for photothermally heated Al NP with the radius of 45 nm, 60 nm, and 75 nm on the (a) grating and (b) flat silver substrate. The (c) heat generation rate and volumetric energy generation rate can be derived from the experimental temperature profiles.

The heat generation rate of the central Al NP can be estimated from the radial temperature profile of the THV [49]. For a first-order approximation, the system was treated as a homogeneous THV slab with a point heating source. The resulting temperature profile is radially symmetric such that the steady-state temperature profile may be readily obtained from the heat diffusion equation. Denoted as "curve fit data" in **Figure 6-9(a-b)**, the temperature profile of the THV matrix was fit to an assumed solution of $\boldsymbol{T(r) = -C_1/r + C_2}$, where $\boldsymbol{C_1}$ and $\boldsymbol{C_2}$ are the curve fit constants, and $\boldsymbol{r}$ is the radial distance from the center nanoparticle. Note that the fit was performed preferentially to the first micron of the radial distribution, as the thickness of the film, convection from the top of the THV film and losses to the grating substrate will invalidate the spherical approximation. Nevertheless, the approximation holds relatively well for radial distances that far exceed the thickness of the film. Origin software was utilized to enable the curve fits of the experimental data. The radial temperature derivatives, namely, the heat transfer rate and the volumetric heating rate shown in **Figure 6-9(c)**, can readily be obtained from the approximation of experimental temperature profiles. Data points and standard deviation error bars were

based on four experimental measurements for nanoparticle heating experiments on the silver grating (**Figure 6-10**).

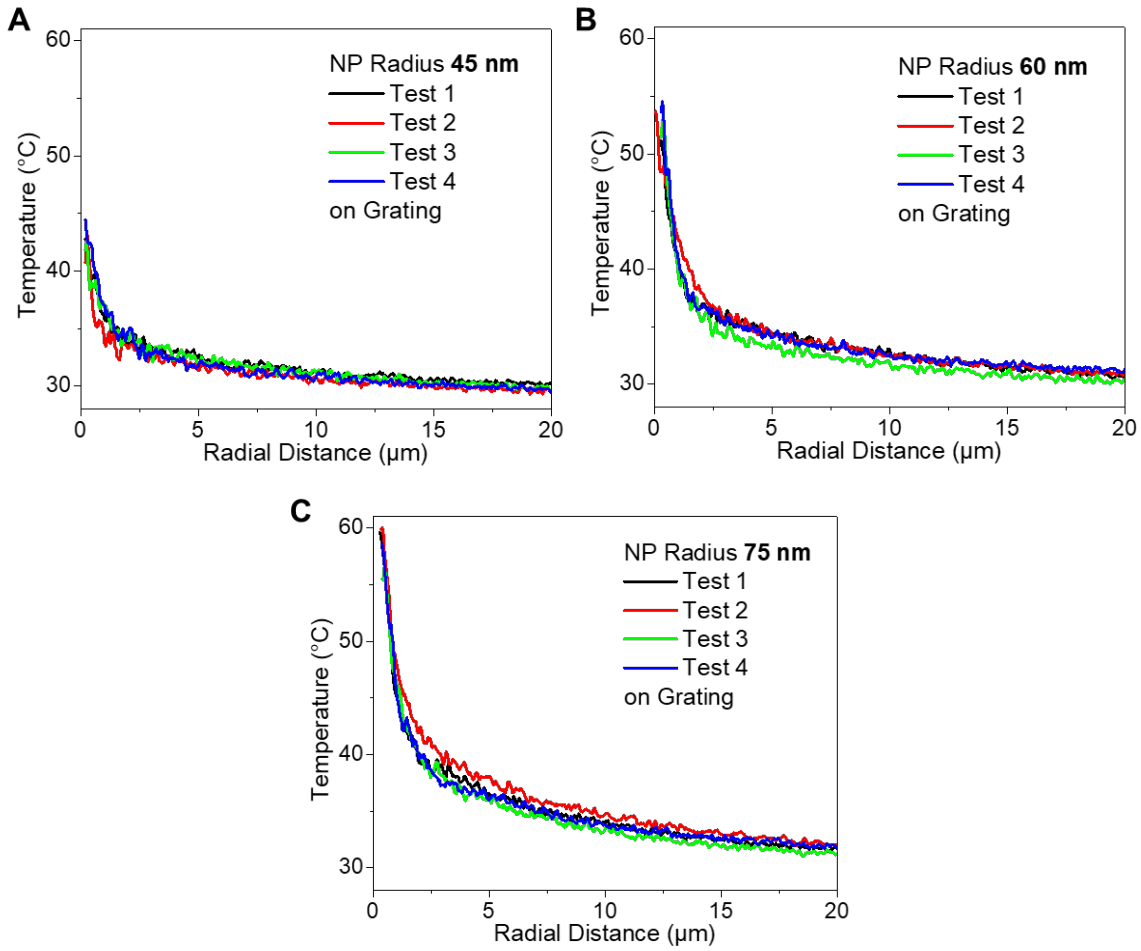

Figure 6-10. Steady-state radial temperature profiles were obtained experimentally. Four independent heating experiments were conducted for each nanoparticle radius: (a) 45 nm, (b) 60 nm, and (c) 75 nm.

The total Al NP heating rate may then be found from the temperature gradient of THV surrounding the NP. The NP heating rate is found using the relationship

$$q = -k(4\pi r_o^2)\frac{\partial T(r_o)}{\partial r} \qquad (3)$$

where q is the heating rate of the Al NP, k is the thermal conductivity of THV, and r_o represents the interface between the THV and the heated Al NP. [18,24,50] From

the total heating rate, the volumetric heating rate of the Al NP can be obtained by dividing the total heating rate by the volume of the Al NP. For photothermal heating on a grating substrate, the volumetric heating rate of Al NP with radii of 45, 60, and 75 nm is 4.66×10^{16}, 3.85×10^{16}, and 3.64×10^{16} W/m^3, respectively. For Al NPs heated on the flat silver substrate, the volumetric heating rate was 1.95×10^{15}, 1.24×10^{15}, and 0.91×10^{15} W/m^3, respectively. Based on these results, the heating rate of NPs due to field enhancement from the grating was between 24 – 40x greater than that observed for a flat silver substrate.

Table 6-1. Experimental result for nanoparticle embedded in flat silver and silver grating

Parameters	**Flat Silver**			**Silver Grating**		
Nanoparticle Radius (nm)	**45**	**60**	**75**	**45**	**60**	**75**
Experimental Heat Rate (μW)	0.746	1.124	1.612	17.790	34.837	64.257
Experimental Volumetric Heating Rate (W/m^3)	1.95×10^{15}	1.24×10^{15}	0.91×10^{15}	4.66×10^{16}	3.85×10^{16}	3.64×10^{16}

6.12 Conclusions

Fluorescence-based R6G dyes were used as partially aggregated, *in situ* temperature sensors to evaluate the photothermal heating of single Al NPs of 45 nm-75 nm diameters. A plasmonic grating platform was used to enhance the fluorescence intensity, optical resolution, and heating intensity. The dye concentration was designed to achieve a reversible and 'lights-on' temperature-dependent behavior, likely a result of heating-induced transition of R6G dimerized aggregate into monomeric form and separation of monomers from remaining dimers beyond the energy transfer distance. The R6G sensors were employed as thermal probes to determine the temperature response of photothermally heated Al NPs which were

distributed within the same THV media. The fluorescence intensity profiles were converted into spatial temperature maps comprising a spatial resolution of 36 nm and a temporal resolution of 25 ms. The thermal response of Al NPs is expected to be closely related to the radius of the NPs themselves, so the Al NP radius observed by polarization-based optical scattering was calibrated to SEM images to provide a ground truth. The experimental temperature profiles were used to estimate the photothermal energy generation rate of the Al NP. The sensitive, linear fluorescent response of the R6G dye, coupled with the fluorescence intensity enhancement provided by a plasmonic grating substrate, enabled a quantitative temperature sensing modality at a spatial resolution of less than 50 nm per pixel, even for the modest temperature differences presented in this work. This work represents a robust platform for high-resolution imaging and temperature sensing for sub-micron scale investigation.

CHAPTER 7 : FUTURE WORK

7.1 Upcoming Project 1

Investigation of Exfoliated 2D Molybdenum Trioxide and Aluminum Nanoparticle Reactions using In-Situ Laser Heating by Raman and Electron Microscopy Characterization

The project's intellectual merit is providing a greater understanding of the reaction mechanism between exfoliated 2D nanosheet of molybdenum trioxide (MoO_3) and aluminum nanoparticles. The method is to synergize the existing SEM and TEM techniques to capture events during the reaction in real-time using our newly developed in-situ electrical heating stage. The former technique provides the ability to perform energy dispersive X-ray (EDX) spectra mapping to observe the elemental distribution and the change in its composition. In contrast, the latter provides high-resolution imaging to study the morphological transformation due to the reaction. Ex-situ Raman spectroscopy performed outside the EMC further enhances the qualitative analysis of the material before and after the reaction. Combining these advanced characterization techniques will provide more significant results in determining the reaction mechanism at atomic resolution.

The project's broader impacts are benefits to our material science and combustion society by providing the mechanism of reaction mechanism between diffused Al and surface reactions with MoO_3. Our preliminary results indicate a preferred crystal orientation for reaction, and we seek confirmation of our theory using EBSD, in-situ reactions, and high-resolution TEM imaging. Results may also indicate a new methodology for creating high-quality single-layer alumina sheets.

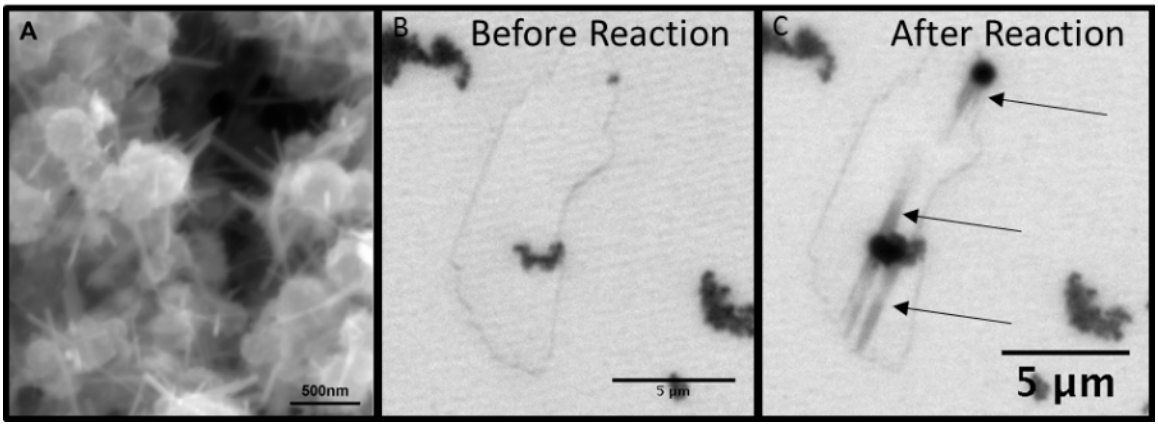

Figure 7-1. (a) SEM image of reacted Al NP and MoO_3 nanosheets showing alumina extensions formed on aluminum oxide shells. Optical images before (b) and after (c) laser heating of Al NPs and reaction with MoO_3 nanosheet substrate. Arrows indicate regions of alumina after the reaction.

Electron microscopy is an essential material characterization technique. With the development of our SEM in-situ electrical heating stage, real-time high-resolution dynamic analysis becomes feasible at nanoscale resolution. In the heating stage, the electrical and electrothermal analysis uses an advanced sample holder to provide ultra-high accuracy and stability of heating controlled by a computer. Localized in-situ heating and characterization methods will be developed to study the fundamental properties of the energetic materials, such as heat transfer, sintering, spallation, and nanoscale morphological change.

Our preliminary study using an in-house Raman spectroscopy has determined that the vibrational modes of MoO_3 are dependent upon incident laser polarization and that the vibrational mode occurring from the Mo-O-Mo deformation at 159 cm^{-1} is the most responsive to fluctuations in temperature. The relation between the temperature and 159 cm^{-1} Raman shifts is calibrated, allowing the Raman peak to act as a localized temperature sensor. Using the Raman laser, Al nanoparticles are locally heated to high temperatures in order to achieve reaction in the nanometer and micrometer

length scales. The shift of the location of the MoO_3 Raman peaks, the change in the full-width-half-maximum, and the variation of intensity of different vibrational modes can together be used as a sensing signal for dynamic thermal mapping. The characterization can allow us to determine the localized temperature by measuring the Raman or PL spectra of MoO_3 before, during, and after combustion. Further, Raman spectroscopy confirms that reaction zones exhibit signatures of aluminum oxide after the reaction, indicating that diffused aluminum has become incorporated into the MoO_3 lattice in the solid-state. Comparison of the Raman spectra taken at different reaction times can be used in the determination of the reaction mechanism, the percentage of reaction, and the corresponding heating temperature and time.

The proposed project aims to utilize EBSD, in-situ SEM reaction, and post-reaction TEM analysis to identify a reaction mechanism between Al nanoparticles and 2D MoO_3 nanosheet. EBSD will be performed on the MoO_3 sheets situated on a silicon substrate to determine the MoO_3 crystal orientation before reaction. It is hypothesized that diffused Al reacts on the exfoliated surface of MoO_3 nanosheets and generates sufficient exothermic energy to displace Mo from the original crystal lattice, resulting in the direct conversion of MoO_3 to Al_2O_3. High-resolution imaging and elemental mapping can be powerful to determine whether 2D MoO_3 sheets were converted to alumina sheets and if the diffusion process occurred at preferential crystal planes. Notice that reaction regions appear to be highly aligned in **Figure 7-1(c)**, indicating a possible preferred crystal orientation for a reaction. Raman spectroscopy will be used as a complementary procedure to react to Al and MoO_3 using the Raman laser. The primary expected outcome is a clarification of the mechanisms responsible for the morphological variation previously observed during post-reaction characterization.

Sample preparation and experiment. Inspired by in-situ Raman spectroscopy techniques and the unusual particle morphology produced during the reaction of Al NPs and MoO_3 sheets, [137] we are currently pursuing in-situ electron microscope reactions. The observation was conducted in an FEI Quanta 600 FEG environmental SEM (ESEM) at the University of Missouri. The system utilized Protochips Fusion MEMS-based "E-chips" to heat the reactants to their reaction temperatures. The Al NP and MoO_3 sheets were prepared using the directed self-assembly techniques described previously. [137] Briefly, 80 nm diameter Al NPs were dispersed with MoO_3 sheets at an equivalence ratio of 1.4. Ethanol was used as the dispersion solvent for optimized compatibility with microscopy techniques. Two microliters of the dispersion were placed onto the thin film heater of the E-Chip and allowed to dry in the open air. A schematic of the test platform is observed in **Figure 7-2**.

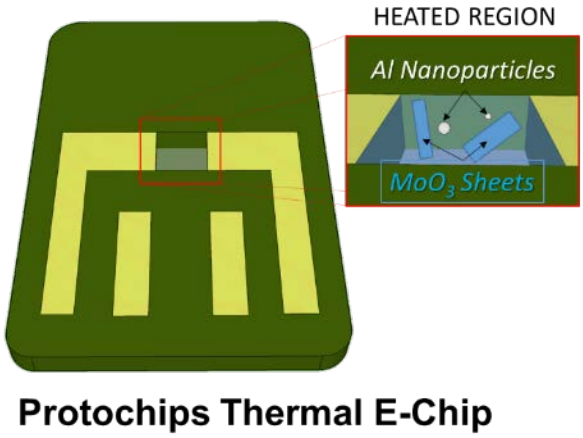

Figure 7-2. Schematic of Protochips Thermal E-Chip with Al NPs and MoO_3 flakes.

Once mounted in the appropriate Protochips holder, the nanoenergetic sample was loaded into the appropriate electron microscope. The Protochips holder establishes electrical contact to the heater element electrical leads to control heating and determine sample temperature. The temperature profile for an experiment was

input into an external control computer running the Protochips Clarity software. The software monitors the temperature of the sample while allowing the user to input a thermal heating profile. For TEM experiments, a heating rate of 50 °C/min was selected. This heating rate is similar to the 20 °C/min heating profile used in DSC-TGA experiments that produced the particle morphology produced in **Figure 7-3**. As previously determined and discussed, the linear extensions protruding from the Al NP alumina shells consist of alumina rather than MoO_3. In situ experiments intend to determine the reaction mechanisms responsible for creating these unique particle morphologies.

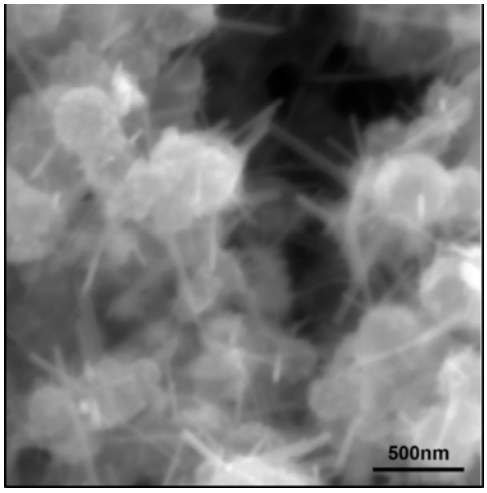

Figure 7-3. Particle morphology produced by 80 nm Al NP reaction with MoO_3 sheets.

Preliminary result and discussion. Our 2D materials prepared using the directed self-assembly technique ensures intimate proximity between the constituents. When the Al is close to the onset reaction temperature, it is hypothesized that diffused Al reacts on the exfoliated surface of MoO_3 nanosheets and generates sufficient exothermic energy to displace Mo from the original crystal lattice in the direct conversion of MoO_3 to Al_2O_3.

The series of conducted experiments aim to observe our hypothesized mechanism using an integrated Protochips thermal e-chip where a dispersed amount of Al NPs and MoO_3 flakes is deposited. The SEM heating experiment conducted in a high vacuum environment changes the physical properties of Al NPs and MoO_3. As an unintended consequence of conducting tests at low pressure, the MoO_3 flakes melted and decomposed at relatively low temperatures before the Al NP melting. This mismatch of the reaction phase changed the experimental outcomes from the expected result. Experimenting in a low vacuum environment was conducted to encounter the temperature deviation for the phase change. The MoO_3 flakes were melted before Al diffusion from the Al NP alumina shells, which suppresses the exothermic reactions of interest. Another nanoenergetic thermite studied was Al/GO/Bi_2O_3, which is known to undergo a condensed phase initiation mechanism during the reaction. The reaction of Al/Bi_2O_3 occurs at a lower temperature than the point where the release of oxygen from the Bi_2O_3 constituent. We plan to conduct a further in-situ heating experiment using 100 Torr nitrogen in future works.

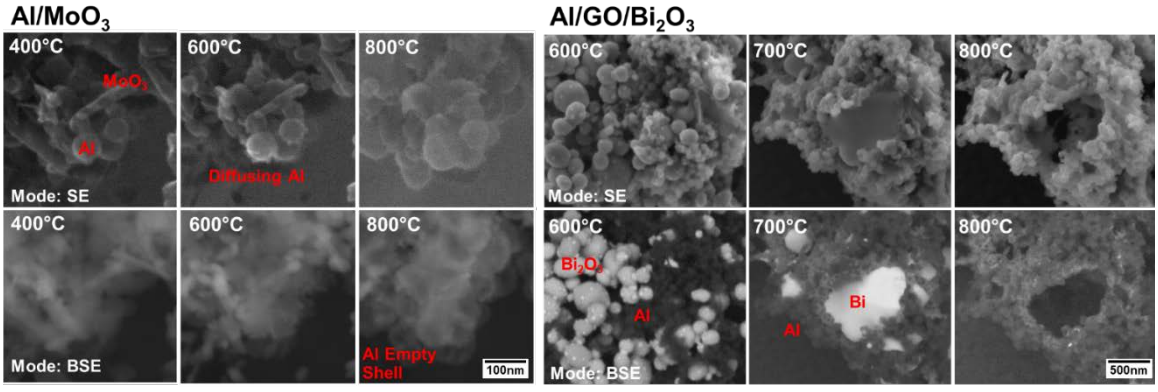

Figure 7-4. Temperature-resolved sequence of images during the in-situ heating of Al/MoO_3 and Al/GO/Bi_2O_3.

Similar in situ reaction experiments have been conducted within an SEM using the same experimental setup. Namely, thermal E-chips were placed on a Protochips SEM stage to facilitate thermal control and thermal sense. Similar results to those observed in TEM-based experiments were observed. Namely, MoO_3 flakes melted and decomposed well before the Al NP melted. Our most recent experiments were conducted in an imaging environment of 100 Pa of nitrogen. While the melting of MoO_3 was suppressed to higher temperatures (500-600 °C), the MoO_3 flakes were melted before Al diffusion from the Al NP alumina shells. A temperature-resolved sequence of images may be found in **Figure 7-5**. Note that the reported temperatures may be less than the temperature of the particles in this sequence because the particles in the image were located on a thick assembly of nanoparticles atop the thin film E-chip heater.

Nevertheless, the decomposition of MoO_3 is evident with increased temperature, with solid crystalline structures completely disappearing at a temperature of 800 °C. Also, at 800 ^oC, the spherical Al NPs appear to be empty shells. Further, the outer diameter of the Al NPs has increased substantially, indicating that Al has escaped the shells and oxidized on the Al NP surface. Additional experiments at higher pressures are planned for the near future.

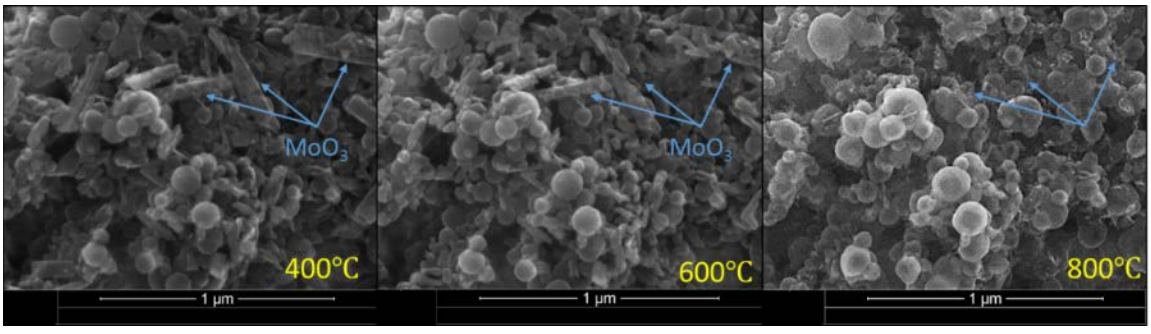

Figure 7-5. In situ SEM reaction of Al NPs and MoO_3 flakes from 400 - 800 ^oC.

While the desired in situ observation of Al NP and MoO_3 flakes has not been observed at this time, we have demonstrated that pressure is an essential parameter for nanothermite reactions. This discovery could lead to mitigation strategies to increase the safety of nanothermite storage. For the case of Al NPs and MoO3, the reduced melting temperature of MoO3 flakes at low pressure suppresses the exothermic reactions of interest. Additional in-situ experiments will utilize 100 Torr nitrogen during heating. Using this strategy, we believe that we can observe the transformation of the Al NP and MoO_3 flakes into the morphology observed in **Figure 7-3**.

PUBLICATION AND PRESENTATIONS

Journal Publication

1. **N. Zakiyyan**, A. Wang, R. Thiruvengadathan, C. Staley, J. Mathai, K. Gangopadhyay, M.R. Maschmann, S. Gangopadhyay," Combustion of Aluminum Nanoparticles and Exfoliated 2D Molybdenum Trioxide Composites," Combustion and Flame, 2018, 187, 1-10.
2. **N. Zakiyyan**, C. Darr, B. Chen, C. Mathai, K. Gangopadhyay, J. McFarland, S. Gangopadhyay, M. Maschmann, "Surface Plasmon Enhanced Fluorescence Temperature Mapping of Aluminum Nanoparticle Heated by Laser," Sensors, 2021, 21(5), 1585.
3. **N. Zakiyyan**, C. Mathai, K. Gangopadhyay, J. McFarland, S. Gangopadhyay, M. Maschmann, "Spallation of Isolated Aluminum Nanoparticles by Rapid Photothermal Heating," (under review)
4. **N. Zakiyyan**, C. Mathai, K. Gangopadhyay, J. McFarland, S. Gangopadhyay, M. Maschmann, "Effect of Nanoparticles Core-Shell Ratio to Nanofragment Dispersion Mechanism in Laser-Induced Plasmonic Enhanced Ignition" (in preparation)
5. **N. Zakiyyan**, C. Mathai, K. Gangopadhyay, J. McFarland, S. Gangopadhyay, M. Maschmann, "In situ Combustion Study of Aluminum Nanoparticles in Fluoropolymer Films by Photothermal Heating" *(in preparation)*

Conference Proceeding

1. S. Gangopadhyay, M. Maschmann, **N. Zakiyyan**, A. Wang, K. Gangopadhyay, "2D MoO3 Processing by Top Down and Bottom Up Techniques and Enhanced Combustion of 2D MoO3/Al Energetic Composites, European MRS meeting Strasbourg, France, May. 2017"
2. **N. Zakiyyan**, B. Chen, M. Riehn, A. Wood, S. Bok, R. Thiruvengadathan, C. Mathai, S. Barizuddin, K. Gangopadhyay, M.R. Maschmann, S.

Gangopadhyay, “Laser Ignition on Aluminum-Polymer Nanoenergetic Systems Using Plasmonic Gratings,” MRS, Nov. 2017, Boston, Ma.

3. S. Gangopadhyay, B. Chen, **N. Zakiyyan**, C. Wolenski, A. Wood, S. Barizuddin, C. Mathai, S. Bok, R. Thiruvengadathan, M. Maschmann, and K. Gangopadhyay, “In Situ Characterization of Nanoenergetics,” MRS, Nov. 2017, Boston, Ma.
4. A. Wang, **N. Zakiyyan**, S. Bok, R. Thiruvengadathan, K. Gangopadhyay, M.R. Maschmann, S. Gangopadhyay, “Synthesis and Characterization of a 3D-Macroscale RGO/Al/Bi2O3 Nanoenergetic Organogel,” MRS, Nov. 2017, Boston, Ma.

REFERENCES

[1] J. Akhavan, *The Chemistry of Explosives* (The Royal Society of Chemistry, 2011).

[2] E. R. Adlard, Chromatographia **49**, 347 (1999).

[3] S. Thangadurai, K. P. S. Kartha, D. R. Sharma, and S. K. Shukla, Sci. Technol. Energ. Mater. **65**, 215 (2004).

[4] D. Sundaram, V. Yang, and R. A. Yetter, *Metal-Based Nanoenergetic Materials: Synthesis, Properties, and Applications*, Progress in Energy and Combustion Science.

[5] E. L. Dreizin, Prog. Energy Combust. Sci. **35**, 141 (2009).

[6] K. Sullivan, G. Young, and M. R. Zachariah, Combust. Flame **156**, 302 (2009).

[7] V. E. Sanders, B. W. Asay, T. J. Foley, B. C. Tappan, A. N. Pacheco, and S. F. Son, J. Propuls. Power **23**, 707 (2007).

[8] S. F. Son, B. Asay, J. R. Busse, B. S. Jorgensen, B. Bockmon, and M. Pantoya, Proc. Int. Pyrotech. Semin. **28th**, 833 (2001).

[9] S. H. Fischer and M. C. Grubelich, (1998).

[10] Y. Jiang, S. Deng, S. Hong, J. Zhao, S. Huang, C. C. Wu, J. L. Gottfried, K. I. Nomura, Y. Li, S. Tiwari, R. K. Kalia, P. Vashishta, A. Nakano, and X. Zheng, ACS Nano **12**, 11366 (2018).

[11] S. J. Apperson, A. V. Bezmelnitsyn, R. Thiruvengadathan, K. Gangopadhyay, S. Gangopadhyay, W. A. Balas, P. E. Anderson, and S. M. Nicolich, J. Propuls. Power **25**, 1086 (2009).

[12] J. J. Granier and M. L. Pantoya, Combust. Flame **138**, 373 (2004).

[13] D. Hanlon, C. Backes, T. Higgins, J. M. Hughes, O. Neill, P. J. King, N. Mcevoy, G. S. Duesberg, B. Mendoza-, H. Pettersson, V. Nicolosi, and J. N. Coleman, 1 (2014).

[14] A. J. Molina-Mendoza, J. L. Lado, J. Island, M. A. Niño, L. Aballe, M. Foerster, F. Y. Bruno, A. López-Moreno, L. Vaquero-Garzon, H. S. J. van der Zant, G. Rubio-Bollinger, N. Agraït, E. Perez, J. Fernandez-Rossier, and A. Castellanos-Gomez, 1 (2015).

[15] E. M. Hunt, S. Malcolm, M. L. Pantoya, and F. Davis, Int. J. Impact Eng. **36**, 842 (2009).

[16] R. W. Conner and D. D. Dlott, J. Phys. Chem. C **116**, 2751 (2012).

[17] C. D. Yarrington, B. Lothamer, S. F. Son, W. Lafayette, T. J. Foley, and L. Alamos, 2009 (2009).

[18] T. Isik, X. Xu, S. F. Son, I. E. Gunduz, and V. Ortalan, Propellants, Explos. Pyrotech. **44**, 1608 (2019).

[19] a. Y. Dolgoborodov, M. N. Makhov, I. V. Kolbanev, a. N. Streletskii, and V. E. Fortov, J. Exp. Theor. Phys. Lett. **81**, 311 (2005).

[20] M. A. Rubio, I. E. Gunduz, L. J. Groven, T. R. Sippel, C. W. Han, R. R. Unocic, V. Ortalan, and S. F. Son, Combust. Flame **176**, 162 (2017).

[21] T. R. Sippel, S. F. Son, and L. J. Groven, Combust. Flame **161**, 311 (2014).

[22] S. L. Row and L. J. Groven, Adv. Eng. Mater. **20**, 1 (2018).

[23] H. Wang, J. Shen, D. J. Kline, N. Eckman, N. R. Agrawal, T. Wu, P. Wang, and M. R. Zachariah, Adv. Mater. **31**, 1 (2019).

[24] B. Chen, H. Zheng, M. Riehn, S. Bok, K. Gangopadhyay, J. McFarland, S. Gangopadhyay, and M. R. Maschmann, Nanotechnology **29**, (2018).

[25] M. L. Pantoya and J. J. Granier, Propellants, Explos. Pyrotech. **30**, 53 (2005).

[26] M. R. Weismiller, J. Y. Malchi, J. G. Lee, R. A. Yetter, and T. J. Foley, Proc. Combust. Inst. **33**, 1989 (2011).

[27] R. Thiruvengadathan, S. W. Chung, S. Basuray, B. Balasubramanian, C. S. Staley, K. Gangopadhyay, and S. Gangopadhyay, Langmuir **30**, 6556 (2014).

[28] A. Bezmelnitsyn, R. Thiruvengadathan, S. Barizuddin, D. Tappmeyer, S. Apperson, K. Gangopadhyay, S. Gangopadhyay, P. Redner, M. Donadio, D. Kapoor, and S. Nicolich, Propellants, Explos. Pyrotech. **35**, 384 (2010).

[29] R. Shende, S. Subramanian, S. Hasan, S. Apperson, R. Thiruvengadathan, K. Gangopadhyay, S. Gangopadhyay, P. Redner, D. Kapoor, S. Nicolich, and W. Balas, Propellants, Explos. Pyrotech. **33**, 122 (2008).

[30] J. N. Coleman, M. Lotya, A. O'Neill, S. D. Bergin, P. J. King, U. Khan, K. Young, A. Gaucher, S. De, R. J. Smith, I. V Shvets, S. K. Arora, G. Stanton, H. Y. Kim, K. Lee, G. T. Kim, G. S. Duesberg, T. Hallam, J. J. Boland, J. J. Wang, J. F. Donegan, J. C. Grunlan, G. Moriarty, A. Shmeliov, R. J. Nicholls, J. M. Perkins, E. M. Grieveson, K. Theuwissen, D. W. McComb, P. D. Nellist, and V. Nicolosi, Science (80-.). **331**, 568 (2011).

[31] V. Nicolosi, M. Chhowalla, M. G. Kanatzidis, M. S. Strano, and J. N. Coleman, Science (80-.). **340**, 1226419 (2013).

[32] S. Ratha and C. S. Rout, ACS Appl. Mater. Interfaces **5**, 11427 (2013).

[33] F. Xia, H. Wang, and Y. Jia, Nat. Commun. **5**, 4458 (2014).

[34] M. Bivour, J. Temmler, H. Steinkemper, and M. Hermle, Sol. Energy Mater. Sol. Cells **142**, 34 (2015).

[35] H. Wang, D. Kong, P. Johanes, J. J. Cha, G. Zheng, K. Yan, and N. Liu, Nano Lett. **13**, 3426 (2013).

[36] K. S. Novoselov, A. K. Geim, S. V. Morozov, D. Jiang, Y. Zhang, S. V. Dubonos, I. V. Grigorieva, and A. A. Firsov, Science (80-.). **306**, 666 (2004).

[37] J. Qiao, X. Kong, Z.-X. Hu, F. Yang, and W. Ji, Nat. Commun. **5**, 4475 (2014).

[38] S. Kim, A. Konar, W.-S. Hwang, J. H. Lee, J. Lee, J. Yang, C. Jung, H. Kim, J.-B. Yoo, J.-Y. Choi, Y. W. Jin, S. Y. Lee, D. Jena, W. Choi, and K. Kim, Nat. Commun. **3**, 1011 (2012).

[39] A. Rai, K. Park, L. Zhou, and M. R. Zachariah, Combust. Theory Model. **10**, 843 (2006).

[40] V. E. Sanders, B. W. Asay, T. J. Foley, B. C. Tappan, A. N. Pacheco, and S. F. Son, J. Propuls. Power **23**, 707 (2007).

[41] B. Jayasena and S. Subbiah, Nanoscale Res. Lett. **6**, 95 (2011).

[42] S. M. Umbrajkar, S. Seshadri, M. Schoenitz, V. K. Hoffmann, and E. L. Dreizin, J. Propuls. Power **24**, 192 (2008).

[43] K. W. Watson, M. L. Pantoya, and V. I. Levitas, Combust. Flame **155**, 619 (2008).

[44] R. J. Jacob, G. Jian, P. M. Guerieri, and M. R. Zachariah, Combust. Flame **162**, 258 (2015).

[45] V. I. Levitas, B. W. Asay, S. F. Son, and M. Pantoya, Appl. Phys. Lett. **89**, 3 (2006).

[46] V. I. Levitas, B. W. Asay, S. F. Son, and M. Pantoya, J. Appl. Phys. **101**, (2007).

[47] V. I. Levitas, M. L. Pantoya, and B. Dikici, Appl. Phys. Lett. **92**, 1 (2008).

[48] R. Thiruvengadathan, A. Bezmelnitsyn, S. Apperson, C. Staley, P. Redner, W. Balas, S. Nicolich, D. Kapoor, K. Gangopadhyay, and S. Gangopadhyay, Combust. Flame **158**, 964 (2011).

[49] V. I. Levitas, M. L. Pantoya, and S. Dean, Combust. Flame **161**, 1668 (2014).

[50] B. Chen, H. Zheng, M. Riehn, S. Bok, K. Gangopadhyay, M. R. Maschmann, and S. Gangopadhyay, ACS Appl. Mater. Interfaces **10**, 427 (2018).

[51] V. I. Levitas and Y. S. Hwang, J. Appl. Phys. **119**, (2016).

[52] M. L. Pantoya and J. J. Granier, J. Therm. Anal. Calorim. **85**, 37 (2006).

[53] G. C. Egan, K. T. Sullivan, T. Lagrange, B. W. Reed, and M. R. Zachariah, J. Appl. Phys. **115**, (2014).

[54] Y. Ohkura, P. M. Rao, and X. Zheng, Combust. Flame **158**, 2544 (2011).

[55] Y. Ohkura, P. M. Rao, and X. Zheng, Combust. Flame **158**, 2544 (2011).

[56] K. W. Watson, M. L. Pantoya, and V. I. Levitas, Combust. Flame **155**, 619 (2008).

[57] T. Iqbal, M. Ijaz, M. Javaid, M. Rafique, K. N. Riaz, M. B. Tahir, G. Nabi, M. Abrar, and S. Afsheen, Plasmonics **14**, 147 (2019).

[58] F. Menges, P. Mensch, H. Schmid, H. Riel, A. Stemmer, and B. Gotsmann, Nat. Commun. **7**, 1 (2016).

[59] J. a Schuller, E. S. Barnard, W. Cai, Y. C. Jun, J. S. White, and M. L. Brongersma, Nat. Mater. **9**, 193 (n.d.).

[60] A. J. Wood, Fabrication and Characterization of a Plasmonic Grating Platform for Enhanced Fluorescence Biosensor Applications, 2016.

[61] A. Otto, Zeitschrift Für Phys. **216**, 398 (1968).

[62] E. Kretschmann and H. Raether, Zeitschrift Fur Naturforsch. - Sect. A J. Phys. Sci. **23**, 2135 (1968).

[63] R. W. Wood, Proc. Phys. Soc. London **18**, 269 (1901).

[64] M. J. Jory, G. W. Bradberry, P. S. Cann, and J. R. Sambles, Meas. Sci. Technol. **6**, 1193 (1995).

[65] J. Homola, I. Koudela, and S. S. Yee, Sensors Actuators, B Chem. **54**, 16 (1999).

[66] S. Maity, J. R. Bochinski, and L. I. Clarke, Adv. Funct. Mater. **22**, 5259 (2012).

[67] X. Li, W. C. H. Choy, L. Huo, F. Xie, W. E. I. Sha, B. Ding, X. Guo, Y. Li, J. Hou, J. You, and Y. Yang, Adv. Mater. **24**, 3046 (2012).

[68] A. J. Wood, B. Chen, S. Pathan, S. Bok, C. J. Mathai, K. Gangopadhyay, S. A. Grant, and S. Gangopadhyay, RSC Adv. **5**, 78534 (2015).

[69] D. Halbertal, J. Cuppens, M. Ben Shalom, L. Embon, N. Shadmi, Y. Anahory, H. R. Naren, J. Sarkar, A. Uri, Y. Ronen, Y. Myasoedov, L. S. Levitov, E. Joselevich, A. K. Geim, and E. Zeldov, Nature **539**, 407 (2016).

[70] C. Mi, J. Zhou, F. Wang, G. Lin, and D. Jin, Chem. Mater. **31**, 9480 (2019).

[71] C. D. S. Brites, P. P. Lima, N. J. O. Silva, A. Millán, V. S. Amaral, F. Palacio, and L. D. Carlos, Nanoscale **4**, 4799 (2012).

[72] D. Ross, M. Gaitan, and L. E. Locascio, Anal. Chem. **73**, 4117 (2001).

[73] V. K. Natrajan and K. T. Christensen, Meas. Sci. Technol. **20**, (2009).

[74] I. Wegrzyn, A. Ainla, G. D. M. Jeffries, and A. Jesorka, Sensors (Switzerland) **13**, 4289 (2013).

[75] H. Huang, G. Firestone, D. Fontecha, R. E. Gorga, J. R. Bochinski, and L. I. Clarke, Nanoscale **12**, 904 (2020).

[76] W. Wei-Wen Hsiao, Y. Yung Hui, P.-C. Tsai, and H.-C. Chang, Acc. Chem. Res. **49**, 400 (2016).

[77] B. del Rosal, U. Rocha, E. C. Ximendes, E. Martín Rodríguez, D. Jaque, and J. G. Solé, Opt. Mater. (Amst). (2017).

[78] Z. Umatova, Y. Zhang, R. Rajkumar, P. S. Dobson, and J. M. R. Weaver, Rev. Sci. Instrum. **90**, (2019).

[79] A. Laraoui, H. Aycock-Rizzo, Y. Gao, X. Lu, E. Riedo, and C. A. Meriles, Nat. Commun. **6**, (2015).

[80] A. Balčytis, M. Ryu, S. Juodkazis, and J. Morikawa, Sci. Rep. **8**, 8 (2018).

[81] B. B. Lahiri, S. Bagavathiappan, T. Jayakumar, and J. Philip, Infrared Phys. Technol. **55**, 221 (2012).

[82] R. Usamentiaga, P. Venegas, J. Guerediaga, L. Vega, J. Molleda, and F. G. Bulnes, Sensors (Switzerland) **14**, 12305 (2014).

[83] F. Yuan, L. Ding, Y. Li, X. Li, L. Fan, S. Zhou, D. Fang, and S. Yang, Nanoscale **7**, 11727 (2015).

[84] L. M. Maestro, E. M. Rodríguez, F. S. Rodríguez, M. C. I. De La Cruz, A. Juarranz, R. Naccache, F. Vetrone, D. Jaque, J. A. Capobianco, and J. G. Solé, Nano Lett. **10**, 5109 (2010).

[85] Q. Ding, X. Zhang, L. Li, X. Lou, J. Xu, P. Zhou, and M. Yan, Opt. Express **25**, 19065 (2017).

[86] S. Li, K. Zhang, J. M. Yang, L. Lin, and H. Yang, Nano Lett. **7**, 3102 (2007).

[87] J. Wu, T. Y. Kwok, X. Li, W. Cao, Y. Wang, J. Huang, Y. Hong, D. Zhang, and W. Wen, Sci. Rep. **3**, 1 (2013).

[88] J. L. Wu, B. S. Cao, L. Rino, Y. Y. He, Z. Q. Feng, and B. Dong, RSC Adv. **7**, 48494 (2017).

[89] F. Ye, C. Wu, Y. Jin, Y. H. Chan, X. Zhang, and D. T. Chiu, J. Am. Chem. Soc. **133**, 8146 (2011).

[90] C. Cao, X. Liu, Q. Qiao, M. Zhao, W. Yin, D. Mao, H. Zhang, and Z. Xu, Chem. Commun. **50**, 15811 (2014).

[91] K. Okabe, N. Inada, C. Gota, Y. Harada, T. Funatsu, and S. Uchiyama, Nat. Commun. **3**, (2012).

[92] C. D. S. Brites, S. Balabhadra, and L. D. Carlos, Adv. Opt. Mater. **7**, 1 (2019).

[93] B. Liu, C. Li, P. Yang, Z. Hou, and J. Lin, Adv. Mater. **29**, (2017).

[94] T. Myint, R. Gunawidjaja, and H. Eilers, J. Phys. Chem. C **116**, 21629 (2012).

[95] B. R. Anderson, R. Gunawidjaja, and H. Eilers, J. Phys. Chem. C (2017).

[96] A. Riedinger, P. Guardia, A. Curcio, M. A. Garcia, R. Cingolani, L. Manna, and T. Pellegrino, Nano Lett. **13**, 2399 (2013).

[97] J. Feng, K. Tian, D. Hu, S. Wang, S. Li, Y. Zeng, Y. Li, and G. Yang, Angew. Chemie **123**, 8222 (2011).

[98] J. Feng, L. Xiong, S. Wang, S. Li, Y. Li, and G. Yang, Adv. Funct. Mater. **23**, 340 (2013).

[99] J. J. Shah, S. G. Sundaresan, J. Geist, D. R. Reyes, J. C. Booth, M. V. Rao, and M. Gaitan, J. Micromechanics Microengineering **17**, 2224 (2007).

[100] C. T. Culbertson, S. C. Jacobson, and J. Michael Ramsey, Talanta **56**, 365 (2002).

[101] B. Chen, H. Zheng, J. Yoon, S. Bok, C. Mathai, K. Gangopadhyay, S. Gangopadhyay, and M. R. Maschmann, Proc. IEEE Sensors 6 (2017).

[102] N. Kuzkova, O. Popenko, and A. Yakunov, Int. J. Biomed. Imaging **2014**, (2014).

[103] T. Kan, H. Aoki, N. Binh-Khiem, K. Matsumoto, and I. Shimoyama, Sensors (Switzerland) **13**, 4138 (2013).

[104] Y. Wu, J. Liu, J. Ma, Y. Liu, Y. Wang, and D. Wu, ACS Appl. Mater. Interfaces **8**, 14396 (2016).

[105] B. Chen, A. Wood, A. Pathak, J. Mathai, S. Bok, H. Zheng, S. Hamm, S. Basuray, S. Grant, K. Gangopadhyay, P. V. Cornish, and S. Gangopadhyay, Nanoscale **8**, 12189 (2016).

[106] A. Wood, S. Barizuddin, C. M. Darr, C. J. Mathai, A. Ball, K. Minch, A. Somoskovi, B. Hamasur, J. T. Connelly, B. Weigl, A. Andama, A. Cattamanchi, K. Gangopadhyay, S. Bok, and S. Gangopadhyay, PLoS One **14**, 1 (2019).

[107] S. Basuray, A. Pathak, S. Bok, B. Chen, S. C. Hamm, C. J. Mathai, S. Guha, K. Gangopadhyay, and S. Gangopadhyay, Nanotechnology **28**, 025302 (2017).

[108] A. Wood, C. J. Mathai, K. Gangopadhyay, S. Grant, and S. Gangopadhyay, ACS Omega **2**, 2041 (2017).

[109] B. Chen, A. Wood, C. M. Darr, S. Bok, K. Gangopadhyay, J. A. McFarland, M. R. Maschmann, and S. Gangopadhyay, Proc. - 2018 IEEE Int. Conf. Bioinforma. Biomed. BIBM 2018 2446 (2019).

[110] C. Wolenski, A. Wood, C. J. Mathai, X. He, J. McFarland, K. Gangopadhyay, S. Gangopadhyay, and M. R. Maschmann, Nanotechnology **30**, (2019).

[111] A. Wang, S. Bok, R. Thiruvengadathan, K. Gangopadhyay, J. A. McFarland, M. R. Maschmann, and S. Gangopadhyay, Combust. Flame **196**, 400 (2018).

[112] Y. Chen, G. C. Egan, J. Wan, S. Zhu, R. J. Jacob, W. Zhou, J. Dai, Y. Wang, V. A. Danner, Y. Yao, K. Fu, Y. Wang, W. Bao, T. Li, M. R. Zachariah, and L. Hu, Nat. Commun. **7**, 12332 (2016).

[113] G. Young, H. Wang, and M. R. Zachariah, Propellants, Explos. Pyrotech. **40**, 413 (2015).

[114] A. Bezmelnitsyn, R. Thiruvengadathan, S. Barizuddin, D. Tappmeyer, S. Apperson, K. Gangopadhyay, S. Gangopadhyay, P. Redner, M. Donadio, D. Kapoor, and S. Nicolich, Propellants, Explos. Pyrotech. **35**, 384 (2010).

[115] R. Thiruvengadathan, C. Staley, J. M. Geeson, S. Chung, K. E. Raymond, K.

Gangopadhyay, and S. Gangopadhyay, Propellants, Explos. Pyrotech. **40**, 729 (2015).

[116] K. Park, D. Lee, A. Rai, D. Mukherjee, and M. R. Zachariah, J. Phys. Chem. B **109**, 7290 (2005).

[117] G. C. Egan, T. Lagrange, and M. R. Zachariah, J. Phys. Chem. C **119**, 2792 (2015).

[118] D. S. Sundaram, P. Puri, and V. Yang, Combust. Flame **169**, 94 (2016).

[119] B. J. Henz, T. Hawa, and M. R. Zachariah, J. Appl. Phys. **107**, (2010).

[120] P. Puri and V. Yang, J. Nanoparticle Res. **12**, 2989 (2010).

[121] M. A. Trunov, M. Schoenitz, and E. L. Dreizin, Combust. Theory Model. **10**, 603 (2006).

[122] M. A. Trunov, M. Schoenitz, and E. L. Dreizin, Propellants, Explos. Pyrotech. **30**, 36 (2005).

[123] A. B. Vorozhtsov, M. Lerner, N. Rodkevich, H. Nie, A. Abraham, M. Schoenitz, and E. L. Dreizin, Thermochim. Acta **636**, 48 (2016).

[124] V. I. Levitas, Combust. Flame **156**, 543 (2009).

[125] B. Chen, A. Pathak, K. Gangopadhyay, P. V. Cornish, and S. Gangopadhyay, Nanobiomedicine **2**, 8 (2015).

[126] K. Bhatnagar, A. Pathak, D. Menke, P. V. Cornish, K. Gangopadhyay, V. Korampally, and S. Gangopadhyay, Nanotechnology **23**, (2012).

[127] C. M. Darr, V. Korampally, B. Chen, K. Gangopadhyay, and S. Gangopadhyay, Sensors Actuators, B Chem. **202**, 1088 (2014).

[128] P. K. Nayak, C. Hsu, S. Wang, J. C. Sung, and J. Huang, Thin Solid Films 0 (2012).

[129] E. Sassaroli, K. C. P. Li, and B. E. O'Neill, Phys. Med. Biol. **54**, 5541 (2009).

[130] H. Yu, P. Zhang, S. Lu, S. Yang, F. Peng, W. S. Chang, and K. Liu, J. Phys. Chem. Lett. **11**, 5836 (2020).

[131] L. Delfour and T. E. Itina, J. Phys. Chem. C **119**, 13893 (2015).

[132] T. Fennel, K. H. Meiwes-Broer, J. Tiggesbäumker, P. G. Reinhard, P. M. Dinh, and E. Suraud, Rev. Mod. Phys. **82**, 1793 (2010).

[133] B. Rufino, F. Boulc'h, M. V. Coulet, G. Lacroix, and R. Denoyel, Acta Mater. **55**, 2815 (2007).

[134] R. Thiruvengadathan, G. M. Belarde, A. Bezmelnitsyn, M. Shub, W. Balas-Hummers, K. Gangopadhyay, and S. Gangopadhyay, Propellants, Explos. Pyrotech. **37**, 359 (2012).

[135] S. Valliappan, J. Swiatkiewicz, and J. A. Puszynski, Powder Technol. **156**, 164 (2005).

[136] M. R. Weismiller, J. Y. Malchi, J. G. Lee, R. A. Yetter, and T. J. Foley, Proc. Combust. Inst. **33**, 1989 (2011).

[137] N. Zakiyyan, A. Wang, R. Thiruvengadathan, C. Staley, J. Mathai, K. Gangopadhyay, M. R. Maschmann, and S. Gangopadhyay, Combust. Flame **187**, 1 (2018).

[138] N. Zakiyyan, C. M. Darr, B. Chen, C. Mathai, K. Gangopadhyay, J. McFarland, S. Gangopadhyay, and M. R. Maschmann, Sensors **21**, 1 (2021).

[139] G. Li, L. Niu, W. Hao, Y. Liu, and C. Zhang, Combust. Flame **214**, 238 (2020).

[140] K. T. Sullivan, N. W. Piekiel, C. Wu, S. Chowdhury, S. T. Kelly, T. C. Hufnagel, K. Fezzaa, and M. R. Zachariah, Combust. Flame **159**, 2 (2012).

[141] V. I. Levitas, M. L. Pantoya, and B. Dikici, Appl. Phys. Lett. **92**, 3 (2008).

[142] Y. Chen, G. C. Egan, J. Wan, S. Zhu, R. J. Jacob, W. Zhou, J. Dai, Y. Wang, V. A. Danner, Y. Yao, K. Fu, Y. Wang, W. Bao, T. Li, M. R. Zachariah, and L. Hu, Nat. Commun. **7**, 1 (2016).

[143] Z. Hu, F. Chen, J. Xu, Q. Nian, D. Lin, C. Chen, X. Zhu, Y. Chen, and M. Zhang, J. Alloys Compd. **746**, 269 (2018).

[144] D. J. Kline, Z. Alibay, M. C. Rehwoldt, A. Idrogo-Lam, S. G. Hamilton, P. Biswas, F. Xu, and M. R. Zachariah, Combust. Flame (2020).

[145] Y. Yang, P. Ghildiyal, and M. R. Zachariah, Langmuir **35**, 3413 (2019).

[146] Y. Yang, Y. Yao, D. J. Kline, T. Li, P. Ghildiyal, H. Wang, L. Hu, and M. R. Zachariah, ACS Appl. Nano Mater. 1 (2020).

[147] J. Y. Malchi, T. J. Foley, and R. A. Yetter, ACS Appl. Mater. Interfaces **1**, 2420 (2009).

[148] J. Sun, M. L. Pantoya, and S. L. Simon, Thermochim. Acta **444**, 117 (2006).

[149] A. Castellanos-Gomez, M. Barkelid, A. M. Goossens, V. E. Calado, H. S. J. Van Der Zant, and G. A. Steele, Nano Lett. **12**, 3187 (2012).

[150] W. Gao, Graphene Oxide Reduct. Recipes, Spectrosc. Appl. 61 (2015).

[151] S. Balendhran, S. Walia, H. Nili, J. Z. Ou, S. Zhuiykov, R. B. Kaner, S. Sriram, M. Bhaskaran, and K. Kalantar-Zadeh, Adv. Funct. Mater. **23**, 3952 (2013).

[152] M. M. Y. A. Alsaif, A. F. Chrimes, T. Daeneke, S. Balendhran, D. O. Bellisario, Y. Son, M. R. Field, W. Zhang, H. Nili, E. P. Nguyen, K. Latham, J. Van Embden, M. S. Strano, J. Z. Ou, and K. Kalantar-Zadeh, Adv. Funct. Mater. **26**, 91 (2016).

[153] J. N. Israelachvili, Acad. Press (2010).

[154] R. Thiruvengadathan, V. Korampally, A. Ghosh, N. Chanda, K. Gangopadhyay, and S. Gangopadhyay, Reports Prog. Phys. **76**, (2013).

[155] E. J. Mily, A. Oni, J. M. Lebeau, Y. Liu, H. J. Brown-Shaklee, J. F. Ihlefeld, and J. P. Maria, Thin Solid Films **562**, 405 (2014).

[156] and M. R. Z. N. W. Piekiel, K. T. Sullivan, S. Chowdhury, Security **298**, (2008).

[157] H. Z. Wu, S. Bandaru, D. Wang, J. Liu, W. M. Lau, Z. Wang, and L. L. Li, Phys. Chem. Chem. Phys. **18**, 7359 (2016).

[158] N. W. Piekiel, L. Zhou, K. T. Sullivan, S. Chowdhury, G. C. Egan, and M. R. Zachariah, Combust. Sci. Technol. **186**, 1209 (2014).

[159] J. Sun and S. L. Simon, Thermochim. Acta **463**, 32 (2007).

[160] K. Moore and M. L. Pantoya, Propellants, Explos. Pyrotech. **31**, 182 (2006).

[161] C. S. Staley, K. E. Raymond, R. Thiruvengadathan, J. J. Herbst, S. M. Swaszek, R. J. Taylor, K. Gangopadhyay, and S. Gangopadhyay, Propellants, Explos. Pyrotech. **39**, 374 (2014).

[162] M. L. Pantoya and S. W. Dean, Thermochim. Acta **493**, 109 (2009).

[163] P. M. Brisley, G. Lu, Y. Yan, and S. Cornwell, IEEE Trans. Instrum. Meas. **54**, 1417 (2005).

[164] K. I. Svensson, A. J. Mackrory, M. J. Richards, and D. R. Tree, (2005).

[165] A. D. Curtis, A. A. Banishev, W. L. Shaw, and D. D. Dlott, Rev. Sci. Instrum. **85**, 1 (2014).

[166] J. Wang, W. P. Bassett, and D. D. Dlott, J. Appl. Phys. **121**, (2017).

[167] R. Padhye, J. McCollum, C. Korzeniewski, and M. L. Pantoya, J. Phys. Chem. C **119**, 26547 (2015).

[168] V. I. Levitas, B. W. Asay, S. F. Son, and M. Pantoya, Appl. Phys. Lett. **89**, (2006).

[169] H. Wang, G. Jian, J. B. Delisio, and M. R. Zachariah, 52nd Aerosp. Sci. Meet. 1 (2014).

[170] H. Furutani, H. Fukumura, H. Masuhara, S. Kambara, T. Kitaguchi, H. Tsukada, and T. Ozawa, J. Phys. Chem. B **102**, 3395 (1998).

[171] F. D. Ruz-Nuglo and L. J. Groven, Adv. Eng. Mater. **20**, 1 (2018).

[172] N. Kostoglou, I. Emre Gunduz, T. Isik, V. Ortalan, G. Constantinides, A. G. Kontos, T. Steriotis, V. Ryzhkov, E. Bousser, A. Matthews, C. Doumanidis, C. Mitterer, and C. Rebholz, Mater. Des. **144**, 222 (2018).

[173] H. Wang, D. J. Kline, and M. R. Zachariah, Nat. Commun. **10**, (2019).

[174] M. N. Slipchenko, C. E. Moody, J. D. Miller, S. Roy, J. R. Gord, and T. R. Meyer, J. Nanotechnol. Eng. Med. **3**, 031007 (2013).

[175] J. Gottfried, E. Bukowski, J. L. Gottfried, and E. J. Bukowski, Appl. Opt. **56**, (2016).

[176] C. Wolenski, A. Wood, C. J. Mathai, X. He, J. McFarland, K. Gangopadhyay, S. Gangopadhyay, and M. R. Maschmann, Nanotechnology **30**, 1 (2019).

[177] P. Innocenzi, H. Kozuka, and T. Yoko, J. Non. Cryst. Solids **201**, 26 (1996).

[178] A. Wood, B. Chen, J. Mathai, S. Bok, S. Grant, K. Gangopadhyay, P. V. Cornish, and S. Gangopadhyay, Micros. Today **25**, 42 (2017).

[179] K. Bhatnagar, A. Pathak, D. Menke, P. V. Cornish, K. Gangopadhyay, V. Korampally, and S. Gangopadhyay, Nanotechnology **23**, (2012).

[180] C. A. Schneider, W. S. Rasband, and K. W. Eliceiri, Nat. Methods **9**, 671 (2012).

[181] F. M. Zehentbauer, C. Moretto, R. Stephen, T. Thevar, J. R. Gilchrist, D. Pokrajac, K. L. Richard, and J. Kiefer, Spectrochim. Acta - Part A Mol. Biomol. Spectrosc. **121**, 147 (2014).

[182] D. Avnir, D. Levy, and R. Reisfeld, J. Phys. Chem. **88**, 5956 (1984).

[183] F. López Arbeloa, P. Ruiz Ojeda, and I. López Arbeloa, J. Chem. Soc. Faraday Trans. 2 Mol. Chem. Phys. **84**, 1903 (1988).

[184] G. Hungerford, K. Suhling, and J. A. Ferreira, J. Photochem. Photobiol. A Chem. **129**, 71 (1999).

[185] V. M. Martínez, F. L. Arbeloa, J. B. Prieto, and I. L. Arbeloa, J. Phys. Chem. B **109**, 7443 (2005).

[186] A. Soleilhac, M. Girod, P. Dugourd, B. Burdin, J. Parvole, P. Y. Dugas, F. Bayard, E. Lacoîte, E. Bourgeat-Lami, and R. Antoine, Langmuir **32**, 4052 (2016).

[187] H. Takakura, Y. Zhang, R. S. Erdmann, A. D. Thompson, Y. Lin, B. McNellis, F. Rivera-Molina, S. N. Uno, M. Kamiya, Y. Urano, J. E. Rothman, J. Bewersdorf, A. Schepartz, and D. Toomre, Nat. Biotechnol. **35**, 773 (2017).

[188] P. J. MacDonald, S. Gayda, R. A. Haack, Q. Ruan, R. J. Himmelsbach, and S. Y. Tetin, Anal. Chem. **90**, 9165 (2018).

[189] M. Wang, B. Bangalore Rajeeva, L. Scarabelli, E. P. Perillo, A. K. Dunn, L. M. Liz-Marzán,

and Y. Zheng, J. Phys. Chem. C **120**, 14820 (2016).

[190] J. R. Lakowicz, J. Malicka, I. Gryczynski, and Z. Gryczynski, Biochem. Biophys. Res. Commun. **307**, 435 (2003).

[191] C. F. Bohren and D. R. Huffman, *Absorption and Scattering of Light by Small Particles* (Wiley, 2008).

[192] S. Wang, Y. Yang, H. Yu, and D. D. Dlott, Propellants, Explos. Pyrotech. **30**, 148 (2005).

[193] K. J. Smith, Y. Cheng, E. S. Arinze, N. E. Kim, A. E. Bragg, and S. M. Thon, (2018).

[194] Y. Peng, Y. Wang, Y. Yang, and D. D. Dlott, J. Nanopart. Res. **12**, 777 (2010).

[195] O. Lecarme, Q. Sun, K. Ueno, and H. Misawa, ACS Photonics **1**, 538 (2014).

[196] S. K. Jha, Z. Ahmed, M. Agio, Y. Ekinci, and J. F. Löffler, J. Am. Chem. Soc. **134**, 1966−1969 (2012).

[197] P. R. West, S. Ishii, G. V Naik, N. K. Emani, V. M. Shalaev, and A. Boltasseva, Laser Photonics Rev. **13**, 1 (2010).

VITA

Naadaa Ghulaam Zakiyyan

Naadaa was born in Situbondo, Indonesia, in April 1994. After completing his high school at Sampoerna Academy Malang, he pursued his bachelor's degree in electrical engineering at the University of Missouri. While he maintained good academic standings, Naadaa was also active in various campus organizations. He served as a former board member of the Mizzou International Student Council and the vice president of the Indonesian Student Association at the University of Missouri. He was also an active member of the Mizzou Hydrogen Car Team, which received several awards from the Shell Eco-marathon Americas in the Urban Concept category. In his first year, his infographics, comparing today's energy situation to that expected in 2050, won the Shell Student Energy Challenge, in which the team received the $5,000 first prize. In his third year, he was selected to serve as the Mizzou Hydrogen Car Team's Electrical Department Lead to continue the designs of urban concept hydrogen-fueled and battery electric vehicles. Additionally, throughout his undergraduate study, Naadaa had the opportunity to join summer internship programs in several Indonesian companies, such as Phillip Morris International, PT Sumberdaya Sewatama, and Credit Suisse Bank. In his senior year, Naadaa had the opportunity to pursue his interest in research while working as an undergraduate research assistant under the supervision of Dr. Shubhra Gangopadhyay's research group. In 2016, Naadaa received his bachelor's degree in Electrical Engineering with Cum Laude and honors, in addition to obtaining minor degrees in Mathematics and Energy Engineering. After his bachelor's graduation, he pursued a Doctor of Philosophy in Biological Engineering at the University of Missouri from June 2016 through July 2022 under the co-supervision of Dr. Shubhra Gangopadhyay and Dr. Matthew Maschmann. His Ph.D. research included designing, simulating, and analyzing an in-situ nanoscale characterization system to capture laser-induced combustion.